2015

Regression rate determination of a gas generator hybrid rocket motor with GOX

Michael D. Mascaro

REGRESSION RATE DETERMINATION OF A GAS GENERATOR HYBRID ROCKET MOTOR WITH GOX

by

MICHAEL D. MASCARO

A THESIS

Submitted in partial fulfillment of the requirements
for the degree of Master of Science in Engineering
in
The Department of Mechanical and Aerospace Engineering
to
The School of Graduate Studies
of
The University of Alabama in Huntsville

HUNTSVILLE, ALABAMA

2015

In presenting this thesis in partial fulfillment of the requirements for a master's degree from The University of Alabama in Huntsville, I agree that the Library of this University shall make it freely available for inspection. I further agree that permission for extensive copying for scholarly purposes may be granted by my advisor or, in his/her absence, by the Chair of the Department or the Dean of the School of Graduate Studies. It is also understood that due recognition shall be given to me and to The University of Alabama in Huntsville in any scholarly use which may be made of any material in this thesis.

Michael D. Mascaro — 4/6/2015 (date)

THESIS APPROVAL FORM

Submitted by Michael D. Mascaro in partial fulfillment of the requirements for the degree of Master of Science in Engineering in Aerospace Systems Engineering and accepted on behalf of the Faculty of the School of Graduate Studies by the thesis committee.

We, the undersigned members of the Graduate Faculty of The University of Alabama in Huntsville, certify that we have advised and/or supervised the candidate of the work described in this thesis. We further certify that we have reviewed the thesis manuscript and approve it in partial fulfillment of the requirements for the degree of Master of Science in Engineering in Aerospace Systems Engineering.

Robert A Frederick Jr. 4/6/15
Dr. Robert A. Frederick, Jr. (Date) Committee Chair

David Lineberry 4/6/2015
Dr. David Lineberry (Date)

4/6/15
Dr. Gabe Xu (Date)

4/7/15
Dr. Keith Hollingsworth (Date) Department Chair

Jennifer K England 4/7/15
for *Dr. Shankar Mahalingam* (Date) College Dean

4/13/15
Dr. David Berkowitz (Date) Graduate Dean

ABSTRACT

School of Graduate Studies
The University of Alabama in Huntsville

Degree Masters of Science in Engineering College/Dept. Engineering/Mechanical and Aerospace Engineering

Name of Candidate Michael D. Mascaro

Title Regression Rate Determination of a Gas Generator Hybrid Rocket Motor with GOX

Hybrid rocket motors suffer from low regression rates when compared to traditional solid rocket motors. This work investigates the regression rate of a mixed oxidizer hybrid motor using a fuel-rich solid grain with and without gaseous oxygen as an oxidizer. The approach consisted of static testing of 15 motors to determine average pressures and regression rates. Ballistic analysis used an optimization sequence to determine a regression rate model using a linear combination of solid and hybrid models. Average regression rates were observed from 0.083 to 0.213 in/s, and predicted at a range from 0.102 to 0.222 in/s with good agreement between the test and ballistic analysis results. The pressure exponents calculated were 0.531 from test data and 0.585 from the ballistic analysis. The calculated oxidizer flux exponent was 2.85 for the tests investigated. Combustion instabilities were observed during hybrid testing.

Abstract Approval: Committee Chair 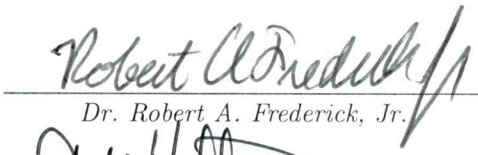

Dr. Robert A. Frederick, Jr.

Department Chair 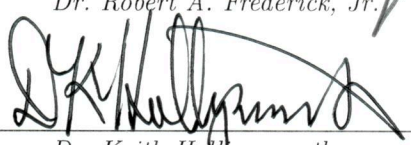

Dr. Keith Hollingsworth

Graduate Dean 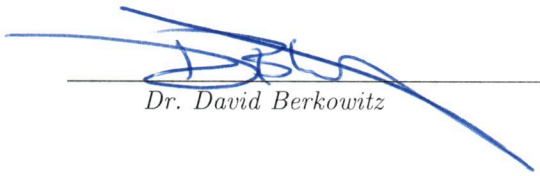

Dr. David Berkowitz

ACKNOWLEDGMENTS

Work performed in this research was done as a part of the NASA STTR Proposal 11-1 T2.01-9811 between Exquadrum, Inc., and the University of Alabama in Huntsville Propulsion Research Center. The propellant grains used during testing were manufactured by Exquadrum, Inc. as part of the NASA STTR proposal. I would specifically like to thank Dr. Marlow Moser of Exquadrum, Inc., for his assistance in pre- and post- test analysis during the testing program.

I would also like to extend sincere thanks to my committee chair and adviser, Dr. Robert A. Frederick, Jr., for his endless support and guidance throughout this project as well as his support throughout my time at the University of Alabama in Huntsville. In addition, I would like to thank Dr. David Lineberry for his support in the development and review of the numerical model, as well as the endless hours spent developing the uncertainty analysis techniques. Thanks also to Dr. Gabe Xu for supporting me during my first stint in research and the trials and tribulations that followed.

Lastly, I would like to extend my thanks to the other members of the Propulsion Research Center who supported me during this work. Thanks to Amy Parlett, Daniel Jones, Brian Roy, and Tony Hall for their assistance in conducting tests. I would like to additionally thank Tony Hall and Brian Roy for their assistance in designing and manufacturing the test set up, and a sincere thanks to Brian Roy for manufacturing nozzle after nozzle on short notice.

TABLE OF CONTENTS

LIST OF FIGURES

LIST OF TABLES

LIST OF SYMBOLS

SYMBOL	DEFINITION
Δt	time step
δt_i	individual uncertainty in measurement
$\eta_{c^\star}$	characteristic velocity efficiency
ρ_p	density of propellant
γ	specific heat ratio
a	temperature coefficient
A_p	grain port area
A_t	nozzle throat area
A_v	venturi throat area
b	hybrid coefficient
$c^\star$	characteristic velocity
D	grain port diameter
D_{ref}	reference grain port diameter
G/S	ratio of gaseous oxidizer to solid fuel burned
G_{ox}	oxidizer mass flux
L	length of grain

L_{pre}, L_{post}	'pre' or 'post'-test length of grain
m	length exponent
$\dot{m}_{ox}$	oxidizer mass flow rate
m_{pre}, m_{post}	'pre' or 'post'-test grain mass
n	pressure exponent
O/F	oxidizer to fuel ratio
P	chamber pressure
P_{ref}	reference chamber pressure
P_v	venturi pressure
q	oxidizer flux exponent
R_g	gas constant
$\dot{r}_{bore}$	regression rate of grain bore
$\dot{r}_{ends}$	regression rate of grain end
r_p	initial radius of grain port
T_{av}	average chamber temperature
t_b	burn time
$T_{burn,i}$	temperature of the combustion gases at step 'i'
T_v	temperature of gas at venturi
U_B	random uncertainty of variable 'B'

V_i	inner volume of motor at step 'i'
$w_{i,pre,head}, w_{i,post,aft}$	web thickness at position 'i', 'pre-test' or 'post-test', 'head' or 'aft' end of grain
web_{pre}, web_{post}	'pre' or 'post'-test grain web thickness

LIST OF ACRONYMS

ACRONYM	DEFINITION
AN	Ammonium Nitrate
AP	Ammonium Perchlorate
AMROC	American Rocket Company
DAQ	Data Aquisition
DRE	Data Reduction Equation
GSR	Gas to Solid Ratio
GOX	Gaseous Oxygen
HTPB	Hydroxyl-Terminated Polybutadiene
HRM	Hybrid Rocket Motor
JRC	Johnson Research Center
LOX	Liquid Oxygen
LRE	Liquid Rocket Engine
MOH	Mixed Oxidizer Hybrid
PLC	Programmable Logic Controller
PRC	Propulsion Research Center
SRM	Solid Rocket Motor

To my mother and father, who have always supported me no matter how far my dreams may take me. To my sister, the best friend I have ever had, and will ever have. To my dog, who forgave every late night and lonely day.

CHAPTER 1

INTRODUCTION

Traditionally, rocket propulsion has utilized one of two motor concepts; liquid rocket engines inject a gaseous or liquid fuel and oxidizer into a chamber for combustion, and solid rocket engines provide the fuel and oxidizer in a composite solid material for combustion. As a method of combining the advantages of both types of traditional rocket propulsion, hybrid rocket engines have been developed to provide fuel or oxidizer in a solid state, with the other reactants in a liquid or gaseous form. This chapter will provide an overview of rocket propulsion technology as it pertains to traditional liquid, solid, and hybrid propulsion as well as the mixed hybrid rocket concept. Additionally, the motivation, scope, and objectives of the work completed is provided within this chapter.

1.1 Overview of Rocket Propulsion Technology

Solid rockets use a premixed combination of fuel and oxidizer cast into a solid shape to provide the combustion reactants for the rocket engine. This allows for high volumetric loading and a simple, cost effective design, but the combination of fuel and oxidizer causes solid rockets to be stored as explosive materials, with the requirements

and regulations that come from such a classification. Liquid rocket engines offer increased performance over solid rocket engines, start/stop and throttling capabilities and the safety of separate fuel and oxidizer, but incorporate additional complexity from the systems required to control the fuel and oxidizer supplies. Hybrid rocket engines were developed to provide the safety and performance of a liquid rocket engine with the simplicity and low cost of a solid rocket [5] [1].

1.1.1 Solid Rocket Propulsion

Solid Rocket Motors (SRMs) are a well-established form of rocket propulsion consisting of fuel and oxidizer mixed together as a single solid grain. This fuel grain contains all the required fuel and oxidizer for combustion. The grain is located directly inside the combustion chamber, and consists of the majority of the motor volume and mass. An igniter is used to initiate combustion of the solid grain, which burns normal to the solid grain surface until the fuel has been exhausted. Since the solid grain consists of both fuel and oxidizer, the combustion occurs on the surface of the grain and the gaseous combustion products are forced through the nozzle to provide the required transfer of momentum for propulsion [1]. A simplified diagram of a SRM is given in Figure 1.1.

Since the combustion products are created directly from the burning surface of the propellant grain, the performance of a SRM directly relates to the rate at which the solid grain burns to form the gaseous products. This is referred to as the burning rate, the rate at which the solid fuel grain regresses normal to the burning surface. An increase to the burning rate creates an increase in the mass flow rate of

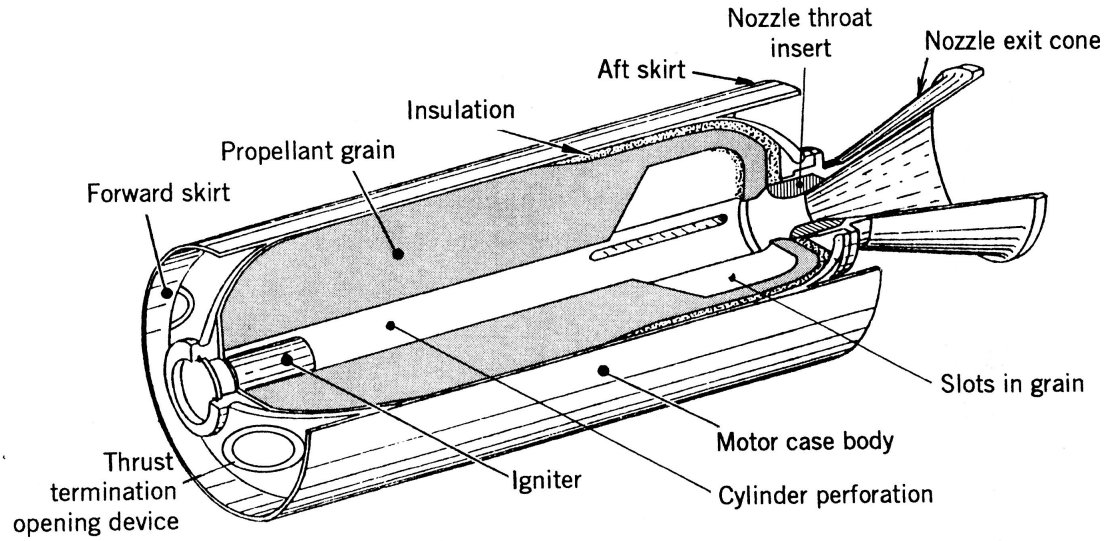

Figure 1.1: Simplified diagram of a solid rocket motor (SRM) [1].

combustion products produced. If the burn surface area of the propellant is constant, a faster burning rate will produce more combustion products, higher pressures in the chamber, and correspondingly a greater momentum transfer through the nozzle [1].

A commonly used model to describe the burning rate of a solid rocket propellant is known as St. Robert's law, and is shown in Equation (1.1). In this equation, the burning rate is described by three parameters; the temperature sensitivity, a, the pressure exponent, n, and the chamber pressure, P. Both a and n are experimentally determined constants for specific propellant composition, and therefore for a given propellant the burning rate is a function of only the chamber pressure. Since the chamber pressure is dependent on the amount of the solid grain combusted at any given time, the pressure is predetermined by the shape and geometry of the grain. This means that the regression rate and therefore the pressure are both primarily dependent on grain geometry and cannot easily be adjusted during motor operation [1].

$$\dot{r} = aP^n \tag{1.1}$$

The fuel grain of a SRM is typically either cartridge-loaded or cast directly into the motor casing, and due to the lack of feed systems SRMs tend to be simpler and cheaper to produce than liquid rocket engines (LRE). In addition, the dense solid fuel grain of a SRM provides high volumetric loading, and the simple design reduces complexity when compared to a liquid rocket motor. However, most solid rocket motors cannot be used more than once, cannot be stopped once ignited, and cannot be easily throttled [1] [5].

1.1.2 Liquid Rocket Propulsion

Liquid Rocket Engines (LREs) are the other well-established form of rocket propulsion commonly used throughout industry, government, and other applications. Unlike solid rocket motors, liquid rocket engines separate the fuel and oxidizer in pressurized tanks until combustion. Feed systems make use of turbopumps or pressurization to introduce propellants into the combustion chamber through an injector. An igniter provides the energy to burn the propellants within the combustion chamber, and the combustion gases are expelled through the nozzle to transfer momentum to the rocket. A simplified diagram of a LRE is given in Figure 1.2.

In a LRE, performance is often controlled by adjusting the mixture ratio, or the ratio of oxidizer mass flow rate to fuel mass flow rate into the chamber. The combustion properties change as the mixture ratio changes, which changes the overall

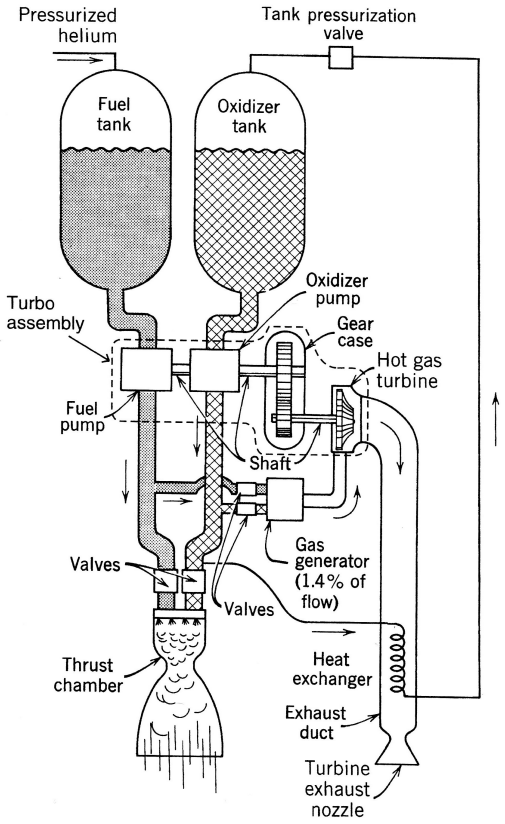

Figure 1.2: Simplified diagram of a liquid rocket motor (LRE) [1].

performance of the engine. By controlling the rate of fuel and oxidizer injected into the combustion chamber, the motor can be throttled, stopped, and restarted as necessary to suit the desired mission profile and performance. By separating the fuel and oxidizer, LREs offer improved safety over SRMs, and LRE propellants can be tailored to provide better performance than the propellant combinations used in SRMs. Liquid rocket engines typically suffer from poor volumetric loading due to the lower density of propellants relative to SRMs, and the added number of components in a LRE adds to the overall system complexity [1].

However, unlike a solid rocket motor, liquid rocket engines can control the mass flow rates of propellants through the system with the use of feed line pressures, valves, and pumps. This enables external control over the propellant flow rates, and therefore LREs offer increased flexibility in mission control and design over that of SRMs [1].

1.1.3 Hybrid Rocket Propulsion

In an effort to harness the advantages of both liquid and solid propulsion, classical hybrid rockets consist of a solid fuel grain and a liquid oxidizer. The solid fuel grain is contained within the combustion chamber, while the oxidizer is stored within a pressure vessel. The liquid oxidizer is transferred into the combustion chamber through an injector, and an igniter provides the required energy to initiate combustion. A diagram of a classical hybrid rocket motor (HRM) is given in Figure 1.3.

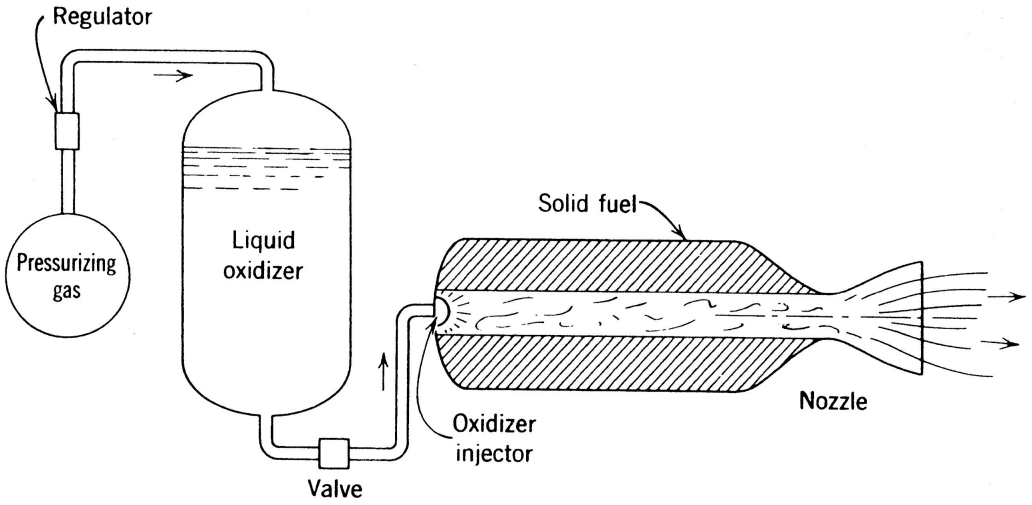

Figure 1.3: Simplified diagram of a classical hybrid rocket motor (HRM) [1].

Since a classical HRM contains only fuel within the solid grain, the combustion process is typically described as a diffusion flame. The solid propellant absorbs energy and vaporizes into a gaseous fuel, which mixes with the oxidizer injected into the chamber and combusts. The mass flux of oxidizer within the combustion chamber is controlled by the injector and oxidizer supply systems, but the corresponding mass flux of fuel is less controllable within a HRM. Similar to the burning rate of a SRM grain, an important property of a HRM is the regression rate of the fuel, or the rate at which the fuel vaporizes normal to the exposed surface. However with most HRM, the surface area of the exposed grain changes as the fuel regresses, which causes changes in the mass flow of fuel into the combustion chamber. This can shift the mixture ratio and change the characteristic velocity of the motor, and therefore change the performance of the motor [1].

Hybrid and liquid rockets typically occupy the same volume, but hybrids have large values of length over diameter (L/D). This means that hybrid rockets tend to be long and narrow, which forces the rocket to have unnecessary structure. Solids and liquids typically can have a smaller value of L/D, and liquid rocket engines are easily tailored to size and geometry constraints. For a hybrid rocket to be competitive in overall geometry and size, the L/D should be less than 12, a value commonly achieved by liquid and solid rockets currently in use [5].

Hybrid rockets also suffer in mass fraction, defined as the mass of the propellant burned divided by the total mass. Solid rockets, due to the fuel and oxidizer being premixed and contained all within one chamber, have very little additional structure requirements; this helps keep the mass fraction sufficiently high. Liquid rocket en-

gines, although they have additional structure requirements due to propellant storage tanks, have the advantage of only needing these structures to withstand relatively low pressures; the majority of the high pressures experienced in a liquid engine happen in the comparatively small combustion chamber. A hybrid rocket, since the oxidizer is kept separate from the fuel in a similar manner to liquid engines, requires additional components such as pumps and storage tanks. However since the hybrid fuel is stored within the combustion chamber, the chamber must be both large enough to contain the fuel and strong enough to withstand the combustion pressures [5].

One of the primary problems with a HRM is that fuel regression rates tend to be approximately one third the value of regression rates observed in SRMs. As a result the surface area in a HRM must be very large to provide the required fuel mass flow rates for most applications. To provide these large surface areas, hybrids make use of complicated fuel grain structures, which can leave behind large amounts of unburned fuel [1]. These remnants of grain are referred to as "residuals," and contribute the weight of the motor after combustion [1]. Often, these residuals are a result of excess fuel grain used to provide structural integrity to the fuel grain. Typically increasing the complexity of the grain geometry or the number of ports increases the residuals inside the motor. To be competitive, the hybrid mass fraction should be between 0.84-0.92 [5]. A common method to reduce the mass of residuals is to simply increase the strength of the fuel grain to reduce the amount of fuel required for grain structural integrity. Another method consists of using structural analysis during the design of the grain to plan for fuel expulsion. This concept designs the grain so that a controlled amount of fuel will be expelled through the nozzle at the

end of the burn due to the conditions inside the motor and the structural integrity of the fuel [6].

A simple equation used to describe the regression rate of the solid fuel grain in a hybrid rocket follows the same form as St. Robert's law for SRMs. This equation, given in Equation (1.2), shows that the regression rate can be determined from a coefficient, b, an exponent, q, and the oxidizer mass flux, G_{ox}. Unlike a SRM, this equation only describes the regression rate, and therefore mass flow, of the fuel grain. The oxidizer mass flow rate is independent, but since the regression rate depends on the mass flux of the oxidizer, the mass flow rate of fuel is linked to that of the oxidizer. As such, the mass flow rate of the fuel will vary non-linearly with changes to the mass flow rate of the oxidizer and varying the total mass flow rate accordingly [1].

$$\dot{r} = bG_{ox}^{q} \tag{1.2}$$

Hybrid rocket motor development has focused on several areas in order to become a viable replacement for solid or liquid propulsion methods. Liquid oxygen (LOX) or gaseous oxygen (GOX) is commonly used as a high performance oxidizer for hybrid motors, often in conjunction with hydroxyl-terminated polybutadiene(HTPB) as a solid fuel grain. LOX-HTPB hybrids have been tested in motors producing thrust up to 250,000 lbf [7] [8]. These motors require a large number of ports in the fuel grain to ensure there is sufficient surface area to achieve the proper mass flow rate of fuel. As a result, hybrids using a large number of ports also require a csomplex injector design to handle the requirements of the port design [9].

The main advantages to hybrid rockets are simple; they provide throttling capabilities, the ability to stop the burn before grain burnout, and increased safety over solid rockets. They also provide easier storage than liquid rockets due to the fuel being a solid grain [1]. The separate fuel and oxidizer of a HRM provides for increased safety in transport and storage, as the fuel grain is simply classified as a flammable material rather than an explosive material [10] [1]. Hybrids do have easier production techniques than solids (reducing costs) as requirements for mixing and safety are not as strict as a solid propellant. Voids or cracks in the solid propellant of a hybrid rocket do not present as large of a detriment as in a solid rocket [5].

1.1.4 Mixed Oxidizer Hybrids

A subset of hybrid rocket motors have been developed to increase the regression rate of the fuel grain in a HRM. Increasing this regression rate increases the mass flow rate of fuel into the motor, and reduces the surface area requirements for a given mass flow rate. A reduced surface area requirement for a given value of motor performance allows for a more efficiently loaded fuel grain, increasing the volumetric loading of the rocket [1].

To achieve these higher regression rates, a Mixed Oxidizer Hybrid (MOH) uses varying amounts of solid oxidizer within the solid fuel grain. The amount of oxidizer mixed with the fuel grain varies depending on the propellant formulations, with amounts typically ranging to 30% by weight [3]. For comparison, SRM can contain oxidizer at amounts closer to 75% by weight [10] [11]. These lower amounts of solid oxidizer are intended to increase the regression rate without classifying the

material as an explosive solid. The majority of MOH concepts are designed with fuel grains unable to sustain combustion without additional oxidizer in order to maintain the safety advantages of a HRM over a SRM [1] [10] [12].

Previous research into the mixed oxidizer concept has suggested a regression rate model that assumes the regression rate is effected by a multiplication of the pressure and oxidizer flux, as shown in Equation (1.3) [10] [3]. In this model, the chamber pressure causes an increase in the regression rate similar to that of a SRM, but without additional oxidizer in the form of the oxidizer flux, the regression is zero. The variables a, n, and q are experimentally determined constants specific to the propellants investigated.

$$\dot{r} = aP^n G_{ox}^q \tag{1.3}$$

1.2 Motivation

In order to increase the regression rate of a the solid fuel grain in a hybrid rocket, the mixed oxidizer hybrid concept introduces small amounts of solid oxidizer into the fuel grain. As the weight percentage of oxidizer within the solid grain increases, the motor combustion characteristics change. Previous research on MOH concepts focus on fuel formulations designed to extinguish without oxidizer flow. The internal ballistics models used for these applications behave in a corresponding fashion [12] [10] [3]. For a higher weight percentage of solid oxidizer, however, a MOH fuel grain can be capable of sustaining combustion even without the additional oxidizer characteristic of a hybrid concept. For such a situation, a different internal ballistics

model must be used. This work was intended to experimentally verify a proposed regression rate model and corresponding internal ballistics model for a MOH concept containing enough oxidizer that combustion can be sustained without the addition of an oxidizer flux through the motor.

1.3 Objectives and Scope

A new formulation for a MOH solid grain has been proposed by Exquadrum, Inc. that is intended for use for hybrid propulsion in upper-stage boosters [13]. This formulation, referred to as Exquadrazine 6514, is based on the mixed oxidizer hybrid concept, but uses a highly oxidized solid grain that does not self-extinguish. Previous testing conducted at Exquadrum, Inc., showed the solid grain is capable of burning as a solid rocket motor. The University of Alabama in Huntsville Propulsion Research Center has been contracted to conduct testing of Exquadrazine 6514 in a hybrid configuration and to characterize the regression rate of the grain. The objective of this work is to determine a regression rate model that can predict the chamber pressure of such a mixed-oxidizer hybrid rocket motor.

The regression rate equation for Exquadrazine 6514 is calculated using a best fit optimization code. The internal ballistics model is designed to simulate the MOH concept for a center port gas generator grain with oxidizer flowing through the port. The proposed regression rate model for the regression of the bore is a function of both chamber pressure, P, and oxidizer flux G_{ox}, as shown in Equation (1.4). The model also assumes that the regression on each end of the grain behaves as a pure solid. As

such, the model proposes that the regression of each grain end follows St.Robert's law and is a function of only the chamber pressure, as given in Equation (1.5)

$$\dot{r}_{bore} = aP^n + bG_{ox}^q \tag{1.4}$$

$$\dot{r}_{ends} = aP^n \tag{1.5}$$

An initial literature review analyzed previous attempts at improving the regression rate of hybrid rockets, focusing on the mixed oxidizer hybrid concept, regression rate models, and experimental techniques for determining regression rates. A proposed form of the regression rate equation and corresponding numerical internal ballistics model was developed. A test matrix was designed to determine the required coefficients for the regression rate equation experimentally. Data collected through experimental test was collected and analyzed along with corresponding thermochemical analysis to provide the inputs for the numerical model.

CHAPTER 2

LITERATURE REVIEW

This chapter reviews sources from the literature on hybrid rocket motors, laboratory testing, and other relevant topics to the objective of this research. Topics researched include hybrid technologies, regression rate improvements, prior regression rate modeling, and burn rate determination techniques. Previous research on mixed oxidizer hybrid and gas generator concepts show a focus on motors that extinguish without oxidizer flux.

2.1 Increasing Hybrid Regression Rate

2.1.1 Melt Layer Concepts

One of the primary objectives of hybrid rocket research and development is identifying methods of increasing the regression rate of the solid fuel grain. One popular method in recent research is the use of "liquefying" fuels. These fuels create a melt layer of viscous material when heated, which vaporizes and mixes with the oxidizer to provide combustion. A common liquefying fuel in research applications is paraffin wax [14], which is observed to have regression rates up to three times that of classical hybrid propellants. Paraffin wax hybrid rocket motors have been operated

in static tests up to sounding rocket scale motors, with stable combustion and an efficiency of at least 91 percent [14]. Wax fuels do suffer from poor grain strength and lack of resistance to temperature and weather extremes, which has hindered their use in non-research applications [5].

Solid cryogenic hybrids are another form of liquefying fuels being investigated to increase regression rates [15]. Karabeyoglu and Altman showed that solid cryogenic hybrids have regression rates 2-5 times the level predicted by conventional regression rate models. Hybrid propellants that form a liquefying layer show an increase in regression rate as the melt layer viscosity and surface tension decrease [15].

2.1.2 Flow Enhancement Concepts

Vortex injectors use aft-end injection to form high velocity flow of oxidizer over the surface of the grain [2]. Chiaverini et. al. found that a HTPB/GOX hybrid using vortex injector technology displayed regression rates up to seven times that of classical HTBP and GOX hybrids. It was theorized this was a result of high convective heat flux at the surface of the fuel due to the high velocity gases within the chamber [2]. Figure 2.1 shows the schematic of the vortex injector hybrid investigated by Chiaverini et. al [2].

2.1.3 Mixed Oxidizer Hybrid Concept

Another technique to increase the regression rate of hybrid rockets is to add a small amount of oxidizer into the solid fuel grain, creating a Mixed Oxidizer Hybrid when lightly oxidized ($< 30\%$ AP) [3]. This concept is also referred to as a gas

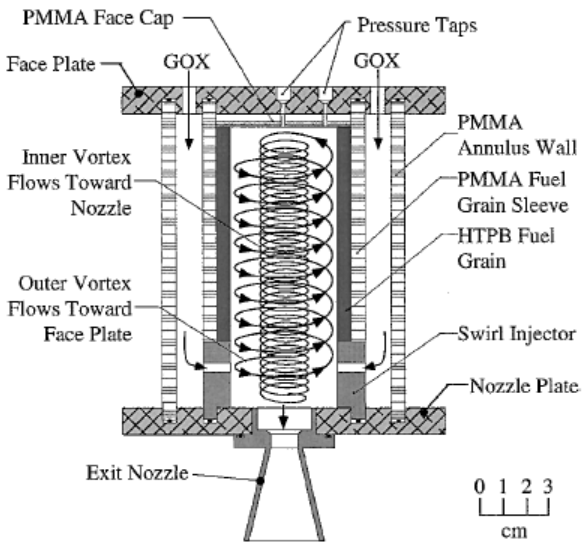

Figure 2.1: Vortex injector hybrid design [2].

generator hybrid motor, referring to the fuel-rich nature of the solid grain. Research has been completed on MOH grains involving Ammonium Nitrate (AN), Ammonium Perchlorate (AP), and other oxidizers [16] [17].

Whitehead and Knox investigated MOH grains using HTPB, varying levels of AP as an oxidizer, and Ferric Oxide as a catalyst. The highest regression rates observed were four and a half times that of a fuel made from only HTPB, through the use of 27.5% AP and 2.5% catalyst by weight. It is important to note that these values were the maximum tested for both oxidizer and catalyst [10] [12]. Further use of AP and catalyst was not pursued as it was suspected that the grain would be beyond the extinguishment limits of the grain [3]. As can be seen in Figure 2.2, the regression rate increases with an increase of oxidizer.

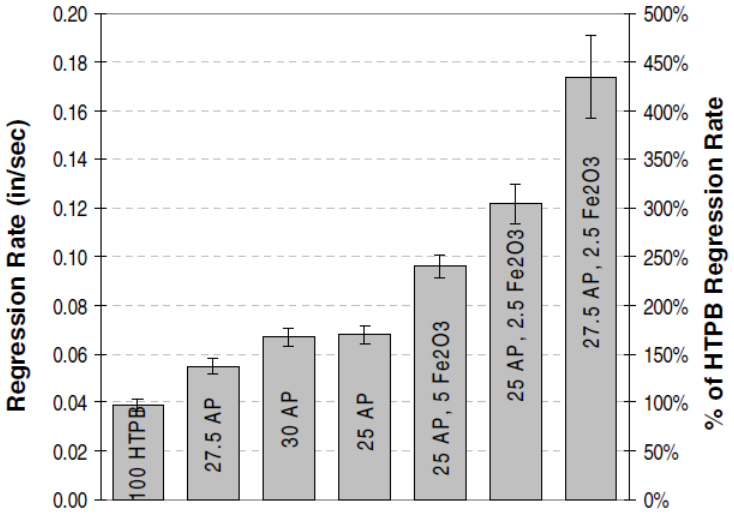

Figure 2.2: Regression rate of mixed oxidizer hybrid with HTPB and varying AP levels [3].

2.1.4 Propellant Extinguishment Concepts

The extinguishment of the propellant is a common limiting concern in the development of MOH solid grains. The use of pure HTPB as a binder with 40-70% AP as an oxidizer has been shown to produce a sooty exhaust with a low pressure deflagration limit which results in poor extinguishment characteristics [17]. This behavior is expected, however, as most solid rocket motors have approximately 70% oxidizer by weight; therefore as the weight percentage of oxidizer in a MOH increases, the propellant should behave closer to that of a SRM [10] [1].

Cohen and Strand researched the relationship between the pressure exponent of the solid grain and the stability and extinguishment properties of the MOH concept. Higher pressure exponents, impossible to use in a solid due as the chamber pressure would increase uncontrollably, are feasible in a MOH concept when the ratio

of fluid oxidizer to solid propellant burned (F/S ratio) increases. As the pressure exponent increases, the extinguishment characteristics of the grain improves, even at low F/S ratios. Correspondingly, lower pressure exponent propellants require higher F/S ratios to maintain the desired extinguishment characteristics [18].

Markopolous and Abel observed varying extinguishment characteristics during testing of a MOH using hydrogen peroxide with a AP loaded solid grain. It was found that heat absorbed by phenolics and case materials were contributing to after-burning when oxidizer flow was cut off. In addition, it was observed that higher characteristic length motors displayed larger ignition overspikes. Larger ignition transients and delays were also observed in higher characteristic length motors [19].

2.2 Regression Rate Modeling

Altman et. al. tested 9 different forms of the regression rate equation and performed statistical analysis with data from AMROC test motors and MOH motors for various scales. This research studied simplified empirical versions, versions with pressure dependency, and versions with length dependency to see how well they predicted the regression rate, and how well they scaled from small to large scale motor results. Simplified regression forms showed the least amount of error in extrapolating from small scale to large scale motor data [20].

The simplest regression rate models are based directly off St. Robert's Law, used to calculate the regression rate of solid rocket motors. Equation (2.1) shows St. Robert's Law, which uses two experimentally determined constants to predict the burning rate; in this equation, a is the temperature coefficient, and n is the pressure

exponent, and P is the chamber pressure [1]. The equivalent regression rate law for hybrid rockets is given in Equation (2.2), which shows the regression rate as a function of oxidizer mass flux, or G_{ox} [1].

$$\dot{r} = aP^n \tag{2.1}$$

$$\dot{r} = bG_{ox}^q \tag{2.2}$$

Other regression rate models used for hybrids replace the oxidizer mass flux term, G_{ox} with the total mass flux, G, as shown in Equations (2.3) and (2.4) [20].

$$\dot{r} = bG^q \tag{2.3}$$

$$\dot{r} = bG^{0.8} \tag{2.4}$$

Models that include a length dependency are given in Equations (2.5), (2.6), and (2.7). In these equations, L is the length of the grain [20]. Some models, like Equation (2.8), include a port diameter term, D, and a density of the propellant, ρ.

$$\dot{r} = bL^m G^q \tag{2.5}$$

$$\dot{r} = bL^{-0.2} G^{0.8} \tag{2.6}$$

$$\dot{r} = bL^m G_{ox}^q \tag{2.7}$$

$$\dot{r} = bL^m G_{ox}^q \left(1 + \frac{(2b)(4q)\rho_p L^{(1+m)}}{DG_{ox}^{(1-q)}}\right) \tag{2.8}$$

The last category of regression rate models include a pressure dependence in the regression rate. It is believed these models are the most applicable to the MOH concept [10] [12] [1] [20]. These models include Equations (2.9), (2.10), (2.11), and (2.12).

$$\dot{r} = bG_{ox}^q P^n \tag{2.9}$$

$$\dot{r} = bG_{ox}^q P^n D^l \tag{2.10}$$

$$\dot{r} = bG_{ox}^q L^m \left(1 - e^{-P/P_{ref}}\right) \tag{2.11}$$

$$\dot{r} = bG_{ox}^q L^m \left(1 - e^{-D/D_{ref}}\right)\left(1 - e^{-P/P_{ref}}\right) \tag{2.12}$$

Altman et. al. found that when predicting the regression rate of motors within the same scale, equations with a length and total flux dependence (Equations (2.5) and (2.6)) produce the least error in predicted and measured values. For classical hybrids, simpler equations such as Equations (2.2), (2.3), and (2.4) have slightly higher

errors in predicting within the same scale, but the error in scaling to a larger scale is reduced compared to more complex equations. In MOH, equations with a pressure dependence such as Equation (2.11) and (2.12) were the most accurate for determining the regression rate of motors within the same scale as well as extrapolating to larger scale motors [20]. The proposed regression rate model was kept simple in order to reduce the error in scaling, and includes a pressure term due to the MOH concept.

2.3 Regression Rate Determination

There are several different methods used to determine the regression rate of both solid and hybrid rocket motors. Common methods include using X-Ray imaging to view the physical regression of the grain over time, placing a window into the combustion chamber and recording the regression of the grain with a camera, ultrasonic testing, and more [21]. Other methods use an analysis of the grain characteristics and pressure trace to determine a burn time for either a propellant grain thickness (web thickness) over time or a mass balance over time [21]. The standard web thickness over time determination can be found from Equation (2.13), where w_b is the web burned and t_b is the burn time [21]. Equation (2.14) shows the determination of regression rate from a mass balance over time method.

$$\dot{r}_{TOT} = \frac{w_b}{t_b} \tag{2.13}$$

$$\dot{r}_{MB} = \frac{w_{avg} \int_B^E P_c dt}{t_b \int_A^G P_c dt} \tag{2.14}$$

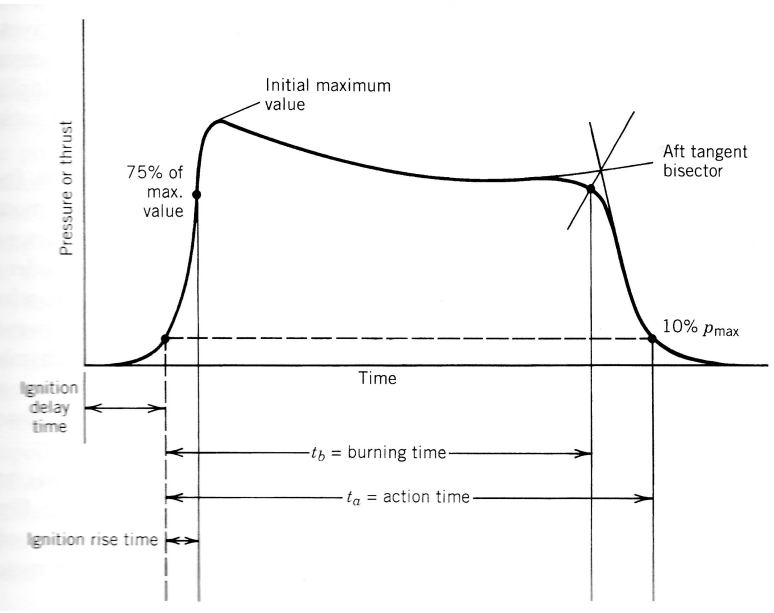

Figure 2.3: Aft-Tangent Bisector method for determining burning time [1].

In determining the burn start time, the most common method used is to assume ignition at a given percentage of the maximum pressure, typically 10% of the maximum [21]. The method for determining the end of the burn, however, is much more varied. Methods include the Tangent-Bisector method, as seen in Figure 2.3, the time at a given percentage of the maximum pressure, the time where the second derivative of pressure (d^2P/dt^2) is zero, or the maximum negative derivative of pressure (dP/dt) after tail-off [21].

2.3.1 Solid Regression Rate Determination

Watson observed that in solid rocket burning rate determination, factors such as propellant curing, casting techniques, and can introduce variation in burn rate. For motors with imperfect bore geometries, an offset between two concentric cylinders can

be used to approximate the burn surface area, which is near linear for offsets up to 5% [22]. When determining the burning rate from a batch of motors, the variations in calculated burning rate can be reduced through the use of larger motors [22].

Determining the burning rate using the average pressure is accurate only if the pressure history is neutral. If the pressure trace is non-neutral, the pressure corresponding to the average burning rate may not be the average pressure. To overcome this, Watson recommends using computerized analysis to calculate a burning rate over time using actual recorded pressure data from motor test firings [22].

Liley also proposed using a single test firing to compare with pressure data generated by an internal ballistics code for solid rocket burning rate determination. The ballistics code takes inputs on the grain geometry, burning rate law, and propellant composition to generate a theoretical pressure trace over time. The code then runs an optimization scheme to determine the burning rate law that provides the least error between the pressure trace generated by the ballistic code and the pressure trace recorded from the actual test firing of the motor. This process used an absolute area percent difference to determine the accuracy of the burning rate law tested [23].

2.3.2 Hybrid Regression Rate Determination

Chiaverini et. al. used x-ray radiography to determine instantaneous regression rates of the solid throughout the grain in classical hybrid with HTPB and GOX. This research showed that regression rate decreases along the axis to a minimum regression rate, and then increases past this point. This research also showed that thermal radiation had a non-negligible effect on the regression rate. The effect of ther-

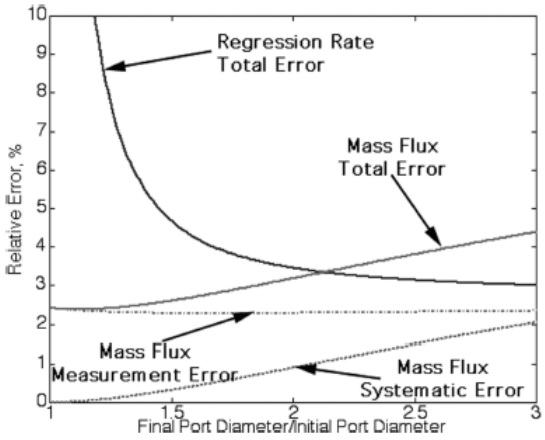

Figure 2.4: Error in regression rate and mass flux as a function of diameter ratio [4].

mal radiation on the regression rate increased at lower mass fluxes and high chamber pressures [24].

In a MOH, Lund et. al. observed significant variation in strand burning rate results for an AP loaded grain, which was attributed to variations in the AP particle size [25]. The uncertainty of the regression rate of lab scale motors can be reduced by increasing of the motor size and the burning time [26]. Karabeyoglu, et. al. showed that for hybrid motors, increasing the web thickness can reduce the error in the regression rate determination. However, increasing the web thickness too much increases the error in the oxidizer flux measurements, as shown in Figure 2.4 [4]. The largest issue in regression rate determination for hybrids, however, is the lack of scaling techniques to adjust lab-scale results to full-scale equivalent regression rates [27] [1].

2.4 Summary of Regression Rate Models

Table 2.1 shows a summary of the hybrid regression rate models discussed. A qualitative overview on scaling characteristics from Altman et. al. is presented for applicable models [20]. The column 'SRM' denotes a model capable of describing the regression rate of a hybrid motor operating without oxidizer, e.g. a MOH burning as a solid rocket. The literature review found no regression rate models intended for use with either a solid rocket motor or a hybrid rocket motor.

This research covers the analysis of a proposed regression rate model that was developed for a propellant grain used as both a SRM and a HRM. The regression rate determination techniques use traditional grain thickness over burn time methods from test data, while the regression rate model is determined from a method similar to that of the optimization and ballistics analysis used by Liley for SRMs.

Table 2.1: Summary of hybrid regression rate models.

Model	Flux Term	Pressure	Length	Diameter /Area	SRM	Notes
(2.1)	N/A	X			X	Used on SRMs
(2.2)	Oxidizer					Commonly used
(2.3)	Total					Scales well to inerts
(2.4)	Total					Scales well to inerts and metal additives
(2.5)	Total		X			Scales well to inerts
(2.6)	Total		X			Scales well to inerts
(2.7)	Oxidizer		X			Poor scaling
(2.8)	Oxidizer		X	X		Consistent scaling for inerts/metal additives
(2.9)	Oxidizer	X				Scaling unknown
(2.10)	Oxidizer	X		X		Poor scaling
(2.11)	Oxidizer	X	X			Poor scaling
(2.12)	Oxidizer	X	X	X		Scales well for metal additives

CHAPTER 3

EXPERIMENTAL METHODS

3.1 Overview

This section describes the facility, hardware, instrumentation, and test matrix used during experimental testing. Testing of the Exquadrazine 6514 grains was conducted at the Johnson Research Center at the University of Alabama in Huntsville. Proven equipment was used for the facility hardware, motor, and instrumentation. The test matrix, given in Table 3.1, details the target pressure, oxygen mass flow rate, used for the tests conducted. Pressure ranges were targeted for approximately 300 psi for the low pressure, 500 psi for the medium pressure, and 800 psi for the high pressure due to equipment limitations. Oxygen flow rates were targeted at 0.1 lbm/s for the low flow rate and 0.6 lbm/s for the high flow rate.

The testing began with three tests without additional oxidizer in order to determine the pressure dependency of the regression rate. The nozzle throat diameter was varied for these tests to vary the average chamber pressure for each test. Following the determination of the pressure dependency, the hybrid portion of the testing introduced the additional test variable of oxygen mass flow rate. For the hybrid tests, both the oxidizer mass flow rate and average chamber pressure were varied to pro-

Table 3.1: Test Matrix

Configuration Number	Target Average Pressure	Target Oxygen Flow Rate
Solid-1	Low	N/A
Solid-2	Medium	N/A
Solid-3	High	N/A
Hybrid-1	Low	Low
Hybrid-2	High	Low
Hybrid-3	Low	High

duce three different test configurations. These three configurations were designed to produce a significant variation in oxidizer mass flow rate to help determine the hybrid portion of the proposed model, Equation (1.4) and Equation (1.5).

To determine the regression rate model, the critical measurements during testing were the grain dimensions and weight before and after the test, the chamber pressure, and the oxidizer mass flow rate. The grain dimensions give the web thickness burned, and the chamber pressure allows for the calculation of burn time to calculate the average regression rate. The oxidizer mass flow rate was calculated from pressure and temperature measurements, and allow for an assessment of how the additional oxidizer affects the regression rate.

3.2 Facility Description

The Johnson Research Center (JRC) at the University of Alabama in Huntsville served as the location for experimental testing. The rocket test cell at this facility is capable of testing SRM, LRE, and HRM systems producing up to 500 pounds of

thrust. The test cell contains a thrust stand within a firing basin, surrounded with concrete-filled cinder-block walls. The pneumatic feed system controls and tubing are located behind the thrust stand, isolated by a concrete wall. Only a single firing valve is located directly behind the thrust stand itself. Separate walls isolate the firing basin from the fuel and oxidizer supplies, located on different sides of the test cell for safety. Valves are operated pneumatically through the use of a Programmable Logic Controller (PLC) which communicates to a remote control room within the JRC for test control. Pressure, temperature, and other sensor measurements are connected to a National Instruments Data Acquisition (DAQ) unit located in an adjacent facility to the test cell. This DAQ unit communicates with a computer in control room for recording and analyzing data signals throughout the test.

Additional safety during testing is ensured through various features of the facility. Locked gates are closed during testing to prevent access to the surrounding area of the rocket test cell, while semaphore lights both on the exterior of the test cell and within the JRC provide an easily identifiable indication of testing in progress. Cameras located both within and around the exterior of the test areas provide the control room with a live view before, during, and after test operations.

3.3 Hardware Description

The gaseous oxygen (GOX) feed system used during testing is a well-established system at the JRC rocket test cell. Testing required modification of only the feed line into the injector and selection of a proper sonic nozzle size for flow control. The igniter system used consisted of the hydrogen-oxygen torch igniter at the JRC rocket

test cell, which has been used previously to ignite SRM, LRE, and HRM systems. The motor hardware was re-purposed from previous HRM testing at the JRC by Whitehead [10] and Knox [12].

3.3.1 Feed System

The GOX feed system, shown in Figure 3.1, at the rocket test cell begins at the oxygen manifold, which is equipped to hold up to six K-bottles of gaseous oxygen. The GOX pressure is controlled through a nitrogen dome loader to regulate the upstream pressure. A tube-insert venturi is placed immediately before the GOX fire valve to regulate the flow of GOX through the feed system. The venturi diameter and GOX pressure upstream of the venturi were modified to change the GOX flow rate as test configurations required. Nitrogen for the GOX dome loader is provided through the nitrogen manifold, which can hold up to three K-bottles of nitrogen gas. This nitrogen is also used as an inert (non-reactive) gas for all line and motor purges for the GOX feed system and igniter feed lines. The pneumatic valves used to control the flow of all gases through the feed system are controlled through pressurized air provided from a compressor.

3.3.2 Igniter

The ignition of the motor grain during testing utilized a hydrogen-oxygen torch igniter system. A single hydrogen K-bottle provides the fuel for the igniter, and the fuel pressure is regulated by a dome loader pressurized by nitrogen. A nitrogen purge is placed on the fuel ignition feed line leading into the igniter. The GOX for

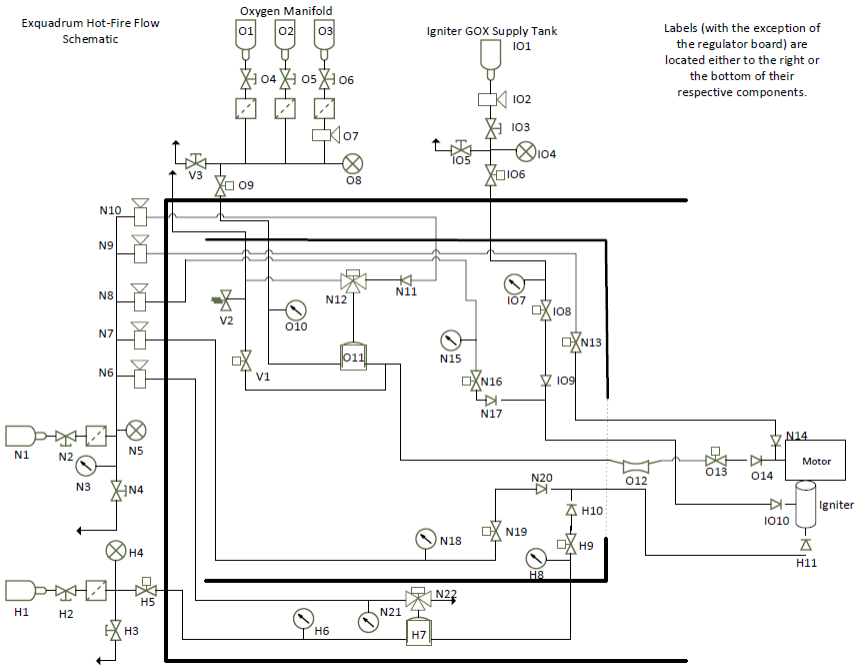

Figure 3.1: JRC Test Cell Feed System Schematic.

the igniter is supplied by an independent oxygen K-bottle using a pressure regulator, and also has an independent nitrogen purge. The igniter torch used was run at a 4:1 ratio of hydrogen to oxygen. This fuel rich condition reduces the amount of unburned oxygen released into the motor, and previous testing has shown this ratio is sufficient to provide the required ignition energy for past SRM, HRM, and other test articles.

A spark plug located on the igniter body provides the ignition energy to combust the hydrogen and oxygen mix within the igniter. The resulting combustion gases are expelled through a 1/4" stainless steel fitting that can be connected to the test article. Figure 3.2 shows a frame taken from video of an igniter test during the experimental test period. The motor has been disassembled to view the combustion gases produced by the igniter and ensure proper operation of the igniter prior to testing.

Figure 3.2: Igniter Test with Motor Hardware Removed.

The torch igniter is visible mounted vertically above the head-end hardware of the motor case.

3.3.3 Motor Design and Mounting

The motor hardware used during testing has been proven in multiple HRM and MOH test firings previously conducted at the JRC by Whitehead [10] and Knox [12]. The head end, aft end, and motor chamber components were made from stainless steel. The head end component consists of an injector port and two 1/4" ports for the igniter combustion gases and for a pressure measurement. The aft end component holds a oxygen-free copper nozzle machined to specification depending on the pressure requirements of each test. The motor chamber consists of a 2.5 inch diameter stainless steel tube, with a length of 12.0 inches. Inside the motor case are two phenolic pieces, one at the injector and one placed on the inner face of the nozzle. These

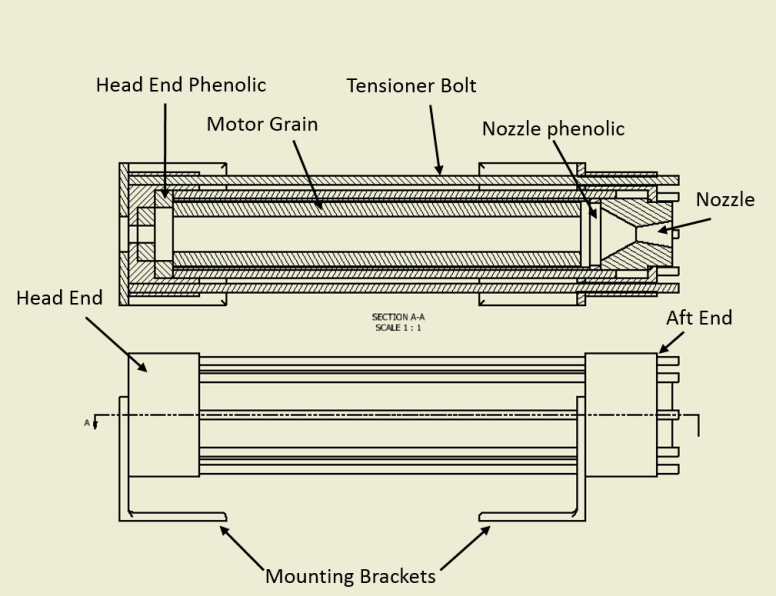

Figure 3.3: Cross sectional drawing of motor assembly.

phenolic pieces are intended to provide the motor components protection from the hot combustion gases during testing. The components are sealed through the use of O-rings and Krytox grease to prevent leaks. Figure 3.3 shows a cross-sectional drawing of the motor assembly.

The motor components are held in tension by eight threaded rods which fit into threaded holes on the head end component. The aft end component is tightened down onto the motor chamber and head end through the use of eight steel nuts. The motor is securely attached to the thrust stand through a head end bracket, which bolts to the head end component of the motor hardware. The aft end bracket rests inside the aft end component. This design increases the overall safety of the hardware by ensuring that in the event of overpressurization, the aft end assembly will separate from the motor chamber, causing rapid depressurization. Figure 3.4 shows the motor

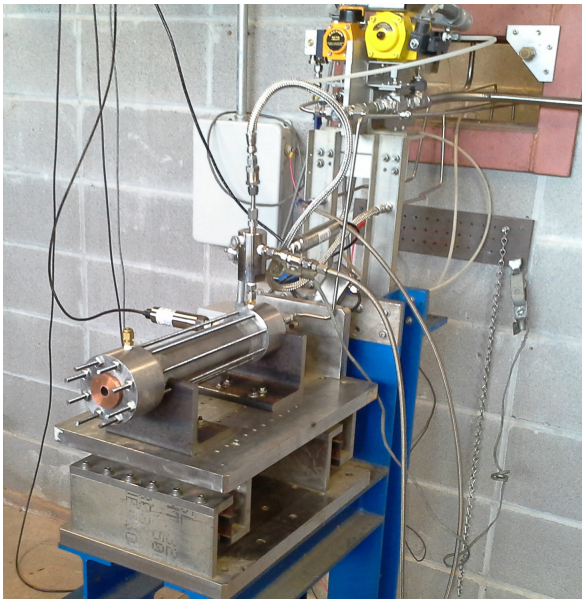

Figure 3.4: Motor Hardware on the Thrust Stand.

hardware assembled on the thrust stand prior to a test without oxidizer. The feed line into the injector is a 1/4" stainless steel tube intended to inject a nitrogen purge into the chamber. Tests as a hybrid using GOX utilized a 1/2" feed line.

3.4 Measurement Description

All pneumatic valves in the feed system for both the GOX supply and the igniter, as well as the igniter spark source, were controlled through the use of an OMRON PLC. This PLC allowed for fully automated sequencing and timing of all valves during the test operation. The PLC valve sequencing and timing values were edited as necessary. Pressure measurements were made at the head end of the motor chamber using a Honeywell transducer rated from 0-3000 psi. A Sensotec 500 lb load cell measured the thrust recorded on the thrust stand.

Oxygen mass flow measurements were made through the use of a venturi, pressure transducer, and thermocouple. GOX flow is choked at the nozzle throat, and therefore the mass flow through the venturi can be determined from an upstream pressure and temperature measurement. A Sensotec transducer provided the pressure measurements, and a K-type thermocouple was used for the temperature measurements.

Data collection occurred through the control room computer running Labview 8.0 software. The data was measured at 1000 Hz, and all measured pressures, temperatures, and thrust values were archived in data files for post-test analysis. For measurement of grain mass pre- and post-test, a Ohaus Scout Pro SP6000 digital scale was used. Grain dimensions were measured using Mitutoyo CD-6" CS calipers.

Video was collected for each of the tests from a variety of cameras. A Panasonic HC-V100M high definition camera was used to record the primary footage for each test, as well as to provide a live video feed of the test area during test operations. High speed footage was recorded at 1000 frames per second for each test using a Red Lake high speed camera. As an additional footage source, a GoPro Hero 3+ Black Edition camera was used to provide a unique video angle for certain tests, when available.

3.5 Test Procedures

Prior to the test day, any motor grains planned for testing were thermally conditioned for 24 hours by placing the grains in a temperature controlled environment. On the day of the planned test the test procedures began with set-up of all cameras and mount of the motor head-end hardware to the thrust stand and feed system. Af-

ter the test area was prepared for testing, the area was brought to a 'red' condition; this condition means that only test members are allowed in the test area. At this point the feed system pressurization began, first with the nitrogen purge. Following the purge pressurization and flow test, the igniter system was pressurized and checked for proper flow rates. Before the full motor was installed on the stand, an igniter test was conducted to ensure proper operation, as can be seen in Figure 3.2.

Once the igniter operation was been verified, the grain was weighed and measured, and then placed into the motor hardware and installed on the thrust stand. For a hybrid test, the oxygen feed system was pressurized and the flow rates were verified. Following this, all cameras were set to record, and the test operator started the firing sequence. The firing sequence consisted of four phases, an igniter firing phase, the main burn phase, the nitrogen purge phase, and an abort phase. In a hybrid test, the oxidizer flow began halfway through the igniter phase and continued through the main burn phase. The abort phase only activated in the event of the abort button being pushed by the test operator.

After the grain burned, the test team waited ten minutes for the area to clear. Pictures were taken of the motor hardware post test and then the motor was disassembled so the grain could be measured. Once the required measurements were taken, the grain was placed in a waste propellant container for storage. After the testing was completed, the cameras, motor hardware, and equipment were disassembled and put away, and the test area was taken off the 'red' condition.

3.6 Test Matrix Development

In order to determine the four empirical constants in the proposed regression rate equation described in Chapter 2, a series of test cases was developed to provide various pressure and oxidizer flow rate configurations. The nozzle throat diameter, mass flow rate of gaseous oxygen, and duration of oxygen flow were varied. All tests were conducted using an ambient grain temperature of approximately 70°F. The test matrix was given in Table 3.1.

The proposed regression rate model gives regression rate as a function of both pressure and oxidizer flux. This model has four experimentally determined constants, and as such four different combinations of pressure and oxidizer flux must be tested. However, the test matrix was planned to test the motors without oxidizer flux first, so that two of the experimental constants could be determined through these tests. As such, two variations of pressure were needed for the tests without oxidizer flux, and two variations of pressure and oxidizer flux were needed for the tests with GOX. The test matrix was developed with more than the minimum required configurations to ensure that chamber pressures do not exceed maximum allowable values due to the lack of prior knowledge of the motor performance with GOX. The target value for the high flow rate tests was determined to be 0.6 lbm/s, as this was predicted to produce near-stoichiometric conditions during motor operation.

CHAPTER 4

DATA REDUCTION METHODS

This chapter describes the two-part data reduction process used to determine the regression rate equation. The first part uses the raw data measured from the tests and converts it into various parameters detailing the performance and characteristics of the motor tested. These values are then used as inputs for the second part of the data reduction, a ballistic analysis code. The ballistic analysis is used to generate a predicted pressure time history, which is compared with the recorded pressure time history from the test data. An optimization sequence is used to iterate through possible coefficient combinations for the regression rate model and a minimum error is used to determine the optimum set of coefficients. Cequel^{TM} thermochemical analysis software was used as part of the ballistic analysis for the calculation of reaction-specific properties such as the temperature and specific heat ratio of the combustion products. Please note that the formulation Exquadrazine 6514 is proprietary information of Exquadrum, Inc., and as such no information will be disclosed about the formulation of the propellant. Uncertainty analysis was performed on both the input variables calculated in the post-test analysis and the regression rate equation output by the optimization sequence.

4.1 Post-Test Data Reduction

Pressure, temperature, and thrust measurements were recorded through Labview software during testing, and were output into a post-test data file. These numbers were analyzed to determine several parameters that were later used as inputs to the ballistic analysis. The values calculated from the post-test analysis were; the estimated grain density, the characteristic velocity efficiency, the time from ignition to 80% of max pressure, the average oxidizer mass flow rate, and the web thickness burned during testing. Additional analysis included calculation of maximum pressures, maximum thrust, and average specific impulse; these values were not used in the second part of the analysis and served as an additional check of the data gathered. The non-reduced and reduced data has been documented in Appendix C

The density of the grain is estimated through measurements made of the web thickness and mass for both pre- and post-test. Web measurements were made at four locations around the circumference of the grain on both the head and aft end, and these measurements were averaged to create average web thicknesses for both pre- and post-test grain conditions. A diagram of the grain dimensions can be found in Appendix D. The equation for the pre-test web thickness is given in Equation (4.1), and the post-test web thickness was calculated in the same manner. The superscripts 'pre' and 'post' refer to pre- or post-test measurements, while 'head' and 'nozzle' refer to the location of the grain where the measurements were made.

$$web_{pre} = \frac{\frac{\sum_{i=1}^{4} w_{i,pre,head}}{4} + \frac{\sum_{j=1}^{4} w_{j,pre,head}}{4}}{2} \tag{4.1}$$

The grain density calculations involved calculating the pre- and post-test volume of the propellant and dividing the change in mass of the propellant by the change in volume. For tests that burned all of the propellant grain, the post-test volume was zero. The calculation is given in Equation (4.2). The grain pre- and post- test length are represented by L_{pre} and L_{post} respectively, while m_{pre} and m_{post} are the pre- and post-test masses of the grain. Please note that r_p refers to the radius of the port through the grain, equal to 0.5 ± 0.005 inches.

$$\rho_p = \frac{m_{pre} - m_{post}}{\pi \left((r_p + w_{pre})^2 - r_p^2\right) L_{pre} - \pi \left((r_p + w_{pre})^2 - (r_p + w_{pre} - w_{post})^2\right) L_{post}} \tag{4.2}$$

Ignition was determined as the time at which the chamber pressure reached 10% of the maximum recorded value. The end of burn was determined by calculating the minimum change in pressure over time (dP/dt). The change in pressure over time is determined using a moving linear fit of thirty points, as shown in Equation (4.3). Please note that the subscript i in the equation for dP/dt represents the point at which the dP/dt is centered. The corresponding equation for burn time is given in Equation (4.4), where $t|_{min\frac{dP}{dt}}$ is the time corresponding to the minimum dP/dt, and $t|_{P_{c,10\%}}$ is the time at which the chamber pressure has reached 10% of its maximum value.

$$\frac{dP}{dt}|_i = \frac{\sum_{j=i-15}^{i+15}(t_j - \bar{t})(P_j - \bar{P})}{\sum_{k=i-15}^{i+15}(t_k - \bar{t})^2} \tag{4.3}$$

$$t_b = t|_{min\frac{dP}{dt}} - t|_{P_{c,10\%}} \tag{4.4}$$

Since the grains tested were designed with a progressive grain that caused a non-neutral pressure trace, the pressure that corresponds to the average burning rate is not the average pressure during the burn [21]. Instead, a rate-averaged pressure was used to provide the pressure corresponding to the average burning rate, as shown in Equation (4.5) [21]. In this equation, P_i is the instantaneous pressure at time, i, n is the pressure exponent from the regression rate model, N is the number of pressure measurements, and t_b is the burn time. This process was used only for the tests without GOX flow.

$$P_{avg} = \left(\frac{\sum_{i=1}^{N} P_i^n dt}{t_b} \right)^{\frac{1}{n}} \tag{4.5}$$

Two regression rates were calculated from each test; an average regression rate was found as well as a maximum regression rate. The average regression rate was calculated from the change in average web thickness given by Equation (4.1). Since measurements of the grain were made at four locations pre- and post test, a maximum regression rate was also calculated from the maximum change in web thickness at a single recorded location, pre- and post-test. The calculations for the average regression rate and maximum average regression rate are given in Equation (4.6) and Equation (4.7). Please note in Equation (4.7), $w_{pre,i}$ and $w_{post,i}$ were evaluated at the index of maximum change in web thickness.

$$\bar{\dot{r}}_{avg} = \frac{w_{pre} - w_{post}}{t_b} \tag{4.6}$$

$$\bar{\dot{r}}_{max} = \frac{w_{pre,i} - w_{post,i}}{t_b} \tag{4.7}$$

Equation (4.8) calculates the average mass flow rate based off of pressure and temperature measurements made upstream of the venturi. Please note, $\bar{P}_v$ is the average pressure upstream of the venturi during the burn time, $\bar{T}_v$ is the average temperature of the flow upstream of the venturi over the same duration, γ is the ratio of specific heats of gaseous oxygen, R is the gas constant of gaseous oxygen, and A_v is the area of the venturi throat.

$$\bar{\dot{m}}_{ox} = \frac{\bar{P}_v A_v \gamma \sqrt{\left(\frac{2}{\gamma+1}\right)^{\left(\frac{\gamma+1}{\gamma-1}\right)}}}{\sqrt{\gamma R \bar{T}_v}} \tag{4.8}$$

The average GOX flux, $\bar{G}_{ox}$ was calculated using the average web thickness burned and the average mass flow rate of GOX. Equation (4.9) shows this calculation.

$$\bar{G}_{ox} = \frac{\bar{\dot{m}}_{ox}}{\pi \left(r_p + \frac{(web_{pre} - web_{post})}{2}\right)^2} \tag{4.9}$$

The characteristic velocity efficiency was calculated using a calculated characteristic velocity based off the recorded chamber pressure, and a theoretical characteristic velocity based off of the average chamber pressure and average ratio of gaseous oxygen to solid fuel burned. These values were used to interpolate a predicted chamber pressure from a two dimensional table of characteristic velocities calculated using Cequel thermochemical analysis software. This use of thermochemical analysis is discussed in greater detail in the next section. The average ratio of gaseous oxygen to

gaseous fuel (or gas to solid ratio) is calculated through the ratio of mass flow rate of oxygen to mass flow rate of fuel, as shown in Equation (4.10).

$$\left(\frac{G}{S}\right)_{avg} = \frac{\bar{\dot{m}}_{ox} t_b}{m_{pre} - m_{post}} \tag{4.10}$$

The characteristic velocity efficiency can then be calculated as the ratio of the average characteristic velocity measured from the test data and the theoretical characteristic velocity. For tests using a configuration without GOX flow, 3295 ft/sec was considered the theoretical characteristic velocity. For tests using the hybrid configuration, the theoretical characteristic velocity is linearly interpolated from four values considered from a combination of low and high gas to solid ratios and low to high chamber pressures. These values are found through rounding the calculated gas to solid ratio to the nearest tenth of a decimal place, and the average chamber pressure is rounded to the nearest hundredth. The equations for the average characteristic velocity, theoretical characteristic velocity, and characteristic velocity efficiency are presented in Equations (4.11), (4.12), and (4.14) respectively.

$$c^\star = \frac{\bar{P}_c A_t}{\left(\frac{m_{pre} - m_{post}}{t_b}\right) + \bar{\dot{m}}_{ox}} \tag{4.11}$$

$$c^{\star}_{theo,R,P} = \left[c^{\star}_{L,L} + \left(\frac{R - R_L}{R_H - R_L}\right)\left(c^{\star}_{H,L} - c^{\star}_{L,L}\right)\right] + \left(\frac{P - P_L}{P_H - P_L}\right) * \tag{4.12}$$

$$\left\{\left[c^{\star}_{L,H} + \left(\frac{R - R_L}{R_H - R_L}\right)\left(c^{\star}_{H,H} - c^{\star}_{L,H}\right)\right] - \left[c^{\star}_{L,L} + \left(\frac{R - R_L}{R_H - R_L}\right)\left(c^{\star}_{H,L} - c^{\star}_{L,L}\right)\right]\right\} \tag{4.13}$$

$$\eta_{c^{\star}} = \frac{c^{\star}}{c^{\star}_{theo,R,P}} \tag{4.14}$$

In Equation (4.11), A_t is the area of the nozzle throat, and $\bar{P}_c$ is the average chamber pressure. For Equation (4.12), $c^{\star}_{theo,R,P}$ refers to the theoretical characteristic velocity at the test conditions of the gas to solid ratio, R, and average chamber pressure, P. The ideal characteristic velocity at the lower ratio and lower pressure is $c^{\star}_{L,L}$, at low ratio and high pressure is $c^{\star}_{L,H}$, high ratio and low pressure is $c^{\star}_{H,L}$, and high ratio and high pressure is $c^{\star}_{H,H}$. The low and high ratios and low and high pressures are represented by R_L, R_H, P_L, and P_H respectively.

The average specific impulse, I_{sp} for each test was calculated from the thrust measurements, F_i, and the mass of the propellant and oxidizer burned, m_p, as shown in Equation (4.15)

$$I_{sp} = \frac{\sum_{i=1}^{N} F_i dt}{m_p g_0} \tag{4.15}$$

4.2 Numerical Model

The optimization code was designed to work with both solid and hybrid test data and results. For the solid tests, a 3D CAD model was used to calculate the burning surface area of the grains at various web thicknesses. This was necessary as several of the motor grains were cast with bores that were crooked, causing uneven surface areas as the grain burned near completion. These values, along with other inputs, were then passed into a numerical model for each iteration in the optimization code.

The numerical model served as the primary method for determining the accuracy of a proposed regression rate equation based off the test data. This numerical model received input from the test data, generated a theoretical pressure trace, and compared this theoretical pressure trace to the recorded pressure trace using an average percent error method. The ballistic analysis code returns several values; it returns a single "average percent error" that corresponds to the accuracy of the fit between the predicted and measured pressure values, an average predicted regression rate, and a maximum average predicted regression rate. Figure 4.1 shows the process of using the numerical model to determine the regression rate model.

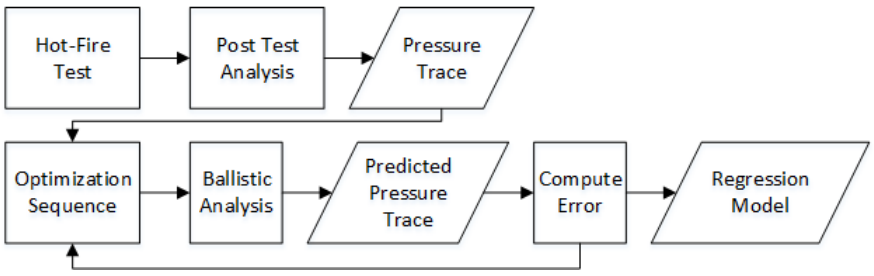

Figure 4.1: Flowchart of calculating regression rate model from test data.

4.2.1 Internal Ballistics

The internal ballistics code received 21 different inputs from the optimization sequence in order to determine the theoretical pressure trace, as listed below.

- Grain quality ('Good' or 'Poor')
- Web thickness to minimum web
- Burn surface area of bore to minimum web
- Burn surface area of ends to minimum web
- Web thickness past minimum web
- Burn surface area of bore past minimum web
- Burn surface area of ends past minimum web
- Throat diameter
- Characteristic velocity efficiency
- Propellant density
- Burn time
- GOX mass flow rate
- Maximum web thickness
- Burning after GOX cutoff (Boolean value)

- Average web thickness
- Temperature coefficient, a
- Pressure exponent, n
- Hybrid coefficient, b
- Hybrid exponent, q
- Measured time values
- Measured pressure values

In the case of a crooked grain, an set of web thicknesses and the corresponding burn surface areas are input for two conditions; one set is for web thicknesses up to the minimum measured web thickness (the condition before the grain first burns to the wall), and the other set for after the web thickness has progressed past the minimum measured web thickness. In the case of the hybrid tests, which did not use crooked grains, these input arrays were empty. A separate text input was used to inform the ballistics code whether it should expect a crooked grain and the corresponding inputs, or a straight grain.

The inputs into the ballistic code also contained the four coefficients for the proposed regression rate model, a_0, b, n, and q. These coefficients were iterated in the optimization code to determine the best fit between the model and the test data, as discussed in a later section. This best fit was the result of a comparison with the predicted values and the measured values given in the listed inputs.

The main portion of the ballistics code used a looping sequence that operated under a fixed time-step concept. An initial pressure was calculated off the igniter mass flow rates, which was fixed for every test. This initial flow rate then was used to

calculate an initial regression rate for the bore and for the ends of the grain. The time step and web thickness are the first two adjustments at the start of each iteration, adding a constant value (0.0001 seconds) to the calculated time, and adjusting the web thickness through the use of Equation (4.16) and Equation (4.17) for the bore and ends of the grain. Once the web thickness has been updated, Equation (4.18) updates the area of the port. Please note that the subscript "i" refers to the current iteration.

$$w_{bore,i} = w_{bore,i-1} + \dot{r}_{bore,i-1}\Delta t \tag{4.16}$$

$$w_{ends,i} = w_{ends,i-1} + \dot{r}_{ends,i-1}\Delta t \tag{4.17}$$

$$A_{p,i} = \pi(r_{inner} + w_{bore,i})^2 \tag{4.18}$$

The area of the burn, A_b, was calculated in one of two ways depending on the type of grain; for a crooked grain the burn surface area was interpolated based on the current web thickness and the data input from the CAD model, for a straight grain the burn surface area was calculated using Equation (4.19) and Equation (4.20). These burn surface areas were calculated separately for both the bore and the ends of the grain. Figure 4.2 shows an example of the changes to the grain geometry and burn surface area for a given iteration.

$$A_{b,bore,i} = 2\pi(r_{inner} + w_{bore,i}) * (L - 2w_{ends,i}) \tag{4.19}$$

$$A_{b,ends,i} = 2\left(\pi(r_{outer})^2 - \pi(r_{inner} + w_{bore,i})^2\right) \tag{4.20}$$

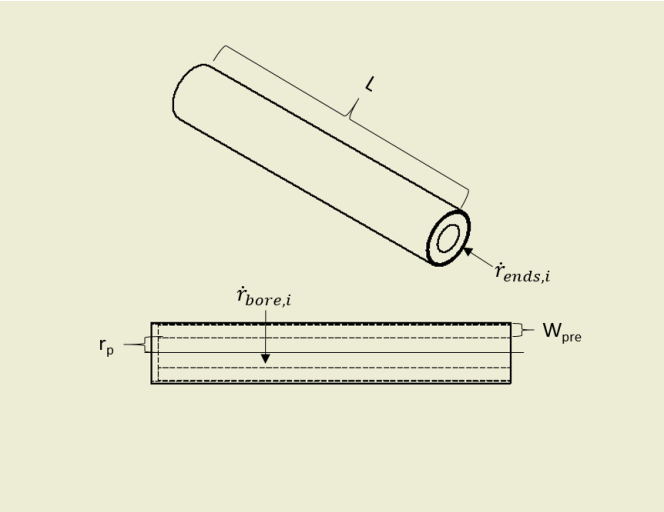

Figure 4.2: Changes in grain dimension during a single iteration of the ballistics analysis code.

The pressure was based on a mass balance in the combustion chamber that considered the mass of gas inside the motor chamber (Equation (4.21)), the mass of propellant burned during the time step (Equation (4.22)), and the mass leaving through the nozzle (Equation (4.23)). This mass combined with the mass of gaseous oxygen entering the chamber during the time step was converted into a pressure through the use of Equation (4.24).

$$m_{existing,i} = \frac{P_i V_i}{R_g T_{burn,i}} \tag{4.21}$$

$$m_{burned,i} = \dot{r}_{bore,i} A_{b,bore,i} \rho_{prop} \Delta t + \dot{r}_{ends,i} A_{b,ends,i} \rho_{prop} \Delta t \tag{4.22}$$

$$m_{leaving,i} = \frac{P_i A_t \Delta t}{c_i^\star} \tag{4.23}$$

$$P_i = \frac{\left(m_{existing,i} + m_{burned,i} + \bar{\dot{m}}_{ox} \Delta t - m_{leaving,i}\right) R_g T_{burn,i}}{V_i} \tag{4.24}$$

Please note in the above equations that ρ_p is the density of the solid fuel grain, R_g is the specific gas constant of the combustion gases, γ_i is the specific heat ratio of the combustion gases, $c_i^\star$ is the characteristic velocity, and Δt is the time step.

The volume inside the motor updates using Equation (4.25), and the gas to solid ratio is updated using Equation (4.26). This ratio is used to determine the specific heat ratio, temperature of the combustion gases, and theoretical characteristic velocity. The calculation of these three parameters will be discussed in the next subsection.

$$V_i = \pi \left((r_{inner} + w_{bore,i})^2 \right) (L - 2w_{ends,i}) + 2\pi w_{ends,i} \left(r_{outer}^2 \right) \tag{4.25}$$

$$\left(\frac{G}{S} \right)_i = \frac{\bar{\dot{m}}_{ox}}{r_{bore,i} A_{b,bore,i} \rho_p + r_{ends,i} A_{b,ends,i} \rho_p} \tag{4.26}$$

Once the chamber pressure has been determined, the regression rate of the bore and the ends of the grain are calculated through Equation (4.27) and Equation (4.28). These iterations then continue until either the web has burned to the maximum thickness input, or burn time in the ballistics analysis has exceeded four times the recorded burn time. This time limit served to reduce the computing time required for tests recreating the crooked grain pressure trace. In straight grains, the maximum web thickness occurs at the maximum burn surface area, but in a crooked grain, the maximum web thickness occurs at very small values of burn surface area. As a result, the corresponding pressures and regression rates are very low for this portion of the analysis, meaning many iterations are required to calculate the burning of the remaining web. By limiting the total time of the ballistic analysis iterations, the overall computing time was reduced.

$$\dot{r}_{bore,i} = aP_i^n + b\left(\frac{\bar{\dot{m}}_{ox}}{A_{p,i}}\right)^q \tag{4.27}$$

$$\dot{r}_{ends,i} = aP_i^n \tag{4.28}$$

4.2.2 Thermochemical Analysis

Cequel^{TM} thermochemical analysis code was used in order to calculate combustion parameters such as the theoretical characteristic velocity, ratio of specific heats, the specific gas constant, and the combustion gas temperature. These values were calculated using the specific formulation of Exquadrazine 6514 to provide the

theoretical maximum values, and are shown in Figure 4.3. A table of values for each of these three parameters was calculated for ranges of 1 to 3000 psi for pressure, and from 0.0 to 5.0 for values of gas to solid ratio and is located in Appendix B.

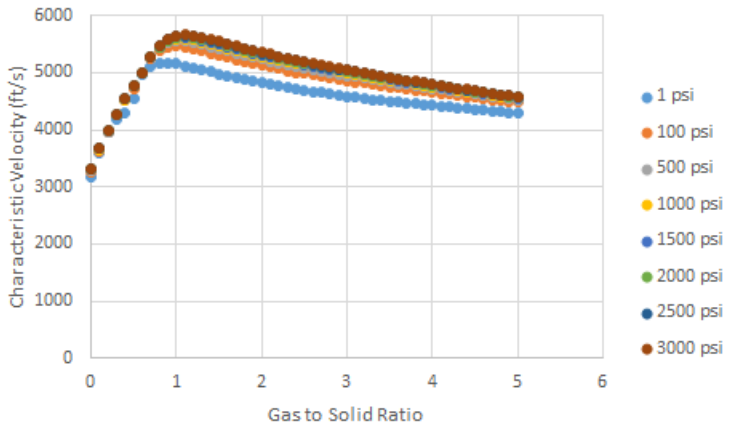

Figure 4.3: Theoretical characteristic velocity as a function of gas to solid ratio for varying chamber pressures.

To calculate a specific value from the tables for a given pressure and ratio, a linear interpolation scheme was developed. The bounds of the interpolation are decided by a rounding of the ratio to a single decimal place, and rounding the pressure to the nearest integer. The first interpolation is performed twice to interpolate the ratio for both the high and low pressure values, as shown in Equation (4.29).

$$X_{LP} = X_{LP,LR} + \left(\frac{R - R_L}{R_H - R_L}\right)(X_{LP,HR} - X_{LP,LR}) \tag{4.29}$$

In these interpolations, X is the variable being considered (characteristic velocity, specific heat ratio, or temperature), R is the current ratio, R_L is the lower

ratio bound, R_H is the high ratio bound, and the subscripts LP,HP, LR, and HR refer to the low and high pressure and ratio bounds. The ratio interpolation given in Equation (4.29) is repeated for the higher pressure bound, and then these two values are interpolated using Equation (4.30).

$$X = X_{LP} + \left(\frac{P - P_L}{P_H - P_L} \right) (X_{HP} - X_{LP}) \tag{4.30}$$

4.2.3 CAD Modeling

To model the burning surface area of a grain with a crooked bore, a three-dimensional model was created using Autodesk Inventor Computer Aided Design (CAD) software. These models were created for each grain in question from the measurements made of pre-test web thickness. The thickness of the grain was then varied by small increments to create a table of web thickness and corresponding surface area of the grain. These values are shown in Figure 4.4 and Figure 4.5. The tables of burn surface area for each crooked grain are given in Appendix F.

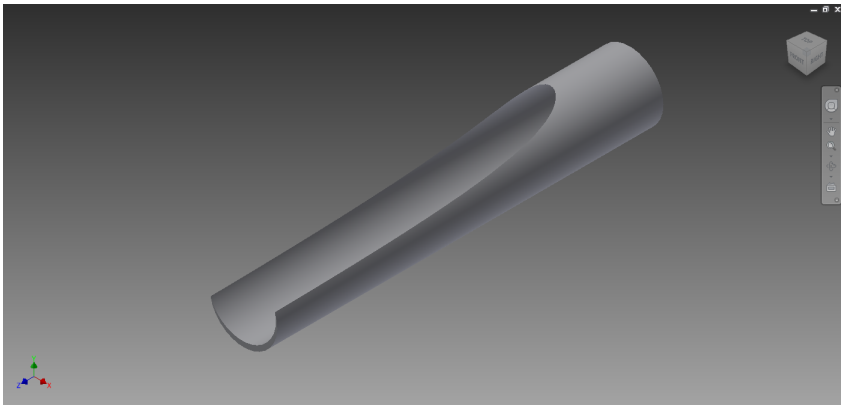

Figure 4.4: 3D CAD Model of Exquadrazine Grain 1, Partially Burned

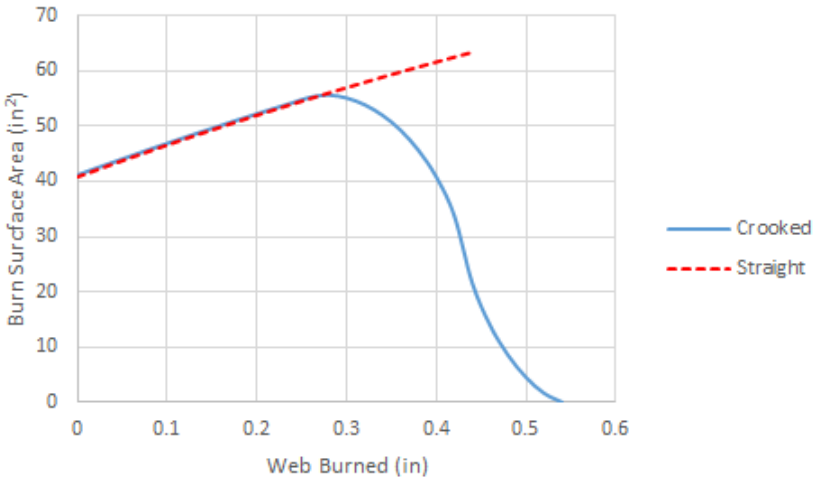

Figure 4.5: Comparison of burn surface area vs. web for a crooked bore and a straight bore grain, from test 4-1.

4.3 Regression Rate Determination

To determine the regression rate equation, the ballistics code previously described was used in combination with the data from the post-test analysis. An iteration scheme was devised to determine two of the four coefficients of the regression rate equation with each run of the optimization sequence. The code begins by assigning a value for the first coefficient, and then looping through a range of possible values for the second coefficient. For each pair of coefficients, the code iterates through each set of test data and uses the ballistic code to return a square error for each test. This square error is calculated using the predicted pressure from the ballistic analysis and the actual pressure from the test data using Equation (4.31).

$$error = \sum_{i=1}^{N} \left(P_{measured,i} - P_{predicted,i}\right)^2 \tag{4.31}$$

The predicted and measured pressure traces are aligned at the ignition time before calculating the square error. For each combination of regression rate coefficients, the error from each test is averaged into a single average error for each set of coefficients. The set of coefficients with the minimum average error provides the best fit, and is considered to be the correct coefficients.

Once the best fit equation has been calculated for the regression rate model, the pressure trace generated by the ballistics analysis was analyzed to determine the average pressure and average regression rate in the same fashion as the post-test analysis. The ignition time was defined in the same manner as the post-test analysis, at 10% of the maximum chamber pressure. For the tests conducted with a crooked bore, the minimum change in pressure over change in time was used to find the end of burn time. For straight bore tests, the burn time corresponded to the maximum pressure time. For solid tests, the average pressure was calculated for the length of the burn time using the rate average pressure equation given in Equation (4.5), while for hybrid tests the average pressure was a time average over the burn time. The maximum average regression rate was calculated using the maximum web thickness burned divided by the burn time, while the average regression rate was calculated using the average web thickness divided by the burn time.

4.4 Uncertainty Analysis

The uncertainty analysis also was performed in two parts. An initial analysis focused on the uncertainty of the inputs to the ballistic code- the uncertainty in the post-test analysis data. Additional calculated values from the post-test data were included in the post-test uncertainty analysis, even though not all of the calculated values were used as inputs to the ballistic analysis. The second part of the uncertainty analysis used the input uncertainty to determine the uncertainty in the predicted regression rate of the proposed regression rate model.

4.4.1 Post-Test Uncertainty Analysis

To find the uncertainty in a result calculated from N variables, $(x_1, x_2, ..., x_N)$, the equation used for each result must be reduced to a Data Reduction Equation (DRE), $r = f(x_1, x_2, ..., x_N)$ [28]. Each DRE is a function of the originally measured values; these values were pressure, mass, length (or thickness), temperature, time, and various constants (where the uncertainty of the constant is assumed to be zero) [28]. The formula used to find the standard uncertainty in a calculated result is given in Equation (4.32).

$$u_r = \sqrt{\sum_{i}^{N} \left(\frac{\delta r}{\delta x_i} \right)^2 u_{x_i}^2} \tag{4.32}$$

The uncertainty for a given result, u_r, is calculated from summation of the square of the partial derivatives of the parameter with each variable $\delta r/\delta x_i$, multiplied by the corresponding measurement uncertainty of each variable, δu_{x_i}. The expanded

uncertainty, U_r, was determined by Equation (4.33) in order to calculate the range in which the true value of r lies for a given confidence interval.

$$U_r = u_r t \tag{4.33}$$

The confidence interval for the uncertainty analysis performed during this work was selected as 95%, corresponding to a value of $t = 2$. This confidence interval was chosen for all expanded uncertainties. These uncertainty calculations were done using Mathematica, and a sample equation for the uncertainty in the mass flow rate of fuel is given in Equation (4.35). The DRE for the mass flow rate of fuel is given in Equation (4.34). The post-test uncertainty calculations are given in Appendix G.

$$\bar{\dot{m}}_f = \frac{m_{pre} - m_{post}}{\Delta t_b} \tag{4.34}$$

$$U_{\dot{m}_f} = \sqrt{\left(\frac{1}{\Delta t_b}\right)^2 U_{m_{post}}^2 + \left(\frac{1}{-\Delta t_b}\right)^2 U_{m_{pre}}^2 + \left(\frac{-(m_{pre} - m_{post})}{{\Delta t_b}^2}\right)^2 U_{\Delta t_b}^2} \tag{4.35}$$

4.4.2 Ballistic Code Uncertainty

The uncertainty in the post-test calculations then served as the input uncertainty for the ballistic code in order to determine the regression rate uncertainty. A Monte Carlo method was used to vary the input values across 5000 iterations for a given regression rate equation. For each iteration, input values were randomly se-

lected for each input from a normal distribution with mean equal to the calculated value and standard deviation equal to half of the expanded uncertainty.

For each iteration of the Monte Carlo analysis, a pressure versus time trace was generated for either the complete burning of the propellant (for solid tests) and the duration of the oxidizer flow (for hybrid tests). From these generated pressure versus time curves, the average regression rate, average pressure, and maximum regression rate for a given regression rate model were returned. This allowed the optimization sequence to capture the standard deviation of a statistical sample for the parameters returned by the ballistic analysis given a specific set of regression rate coefficients and test conditions. The standard uncertainty was taken as the standard deviation of the population, and the expanded uncertainty was calculated as mentioned in Equation (4.33) to capture a 95% confidence interval for the regression rate.

CHAPTER 5

RESULTS

This chapter covers the results of the testing conducted and the corresponding analysis performed. Fifteen static tests of the Exquadrazine 6514 grains were performed, four without additional oxidizer and eleven with GOX as an additional oxidizer. Throughout this chapter, tests without additional oxidizer are referred to as 'no oxidizer' or 'solid' tests, while tests using GOX as an additional are referred to as 'oxidizer' or 'hybrid' tests.

Pressure traces from the hot-fire tests are presented to illustrate phenomenon observed, and the calculated results from the solid tests are presented in the first section. The second section presents pressure traces and results from the hybrid testing, as well as phenomenon observed during testing. The final section presents the results of the regression rate determination and the corresponding uncertainty in the regression rate.

During this chapter, several tests will be referenced by certain characteristics such as hybrid or solid, configuration of the test parameters, or extinguishing and non-extinguishing. For clarity, Table 5.1 identifies each test by the test number and corresponding characteristics.

Table 5.1: Listing of tests conducted and identifying characteristics.

Test Number	Type	Configuration	Nozzle Diameter (in)	Venturi Diameter (in)	GOX Flow (lbm/s)	Extinguishing
4-1	Solid	N/A	0.2969	N/A	N/A	N/A
4-2	Solid	N/A	0.2610	N/A	N/A	N/A
4-3	Solid	N/A	0.2380	N/A	N/A	N/A
4-4	Hybrid	1	0.4375	0.08	0.092	Yes
4-5	Hybrid	1	0.4375	0.08	0.098	Yes
4-6	Hybrid	2	0.3750	0.08	0.100	No
4-7	Hybrid	2	0.3750	0.08	0.101	No
4-8	Hybrid	2	0.3750	0.08	0.101	No
4-9	Hybrid	2	0.3750	0.08	0.101	No
4-10	Hybrid	3	0.4375	0.12	0.302	Yes
4-11	Hybrid	3	0.4375	0.12	0.302	Yes
4-12	Hybrid	4	0.6000	0.186	0.601	Yes
4-13	Hybrid	4	0.6000	0.186	0.594	Yes
4-14	Solid	N/A	0.2610	N/A	N/A	N/A
4-15	Hybrid	2	0.3750	0.08	0.098	No

5.1 Solid Testing

Four solid tests were conducted during the test period; three were conducted to verify the initial viability of the ballistics code and the optimization sequence, while the fourth verified the initial results of the solid testing. These results were also verified against ultrasonic burning rate measurements conducted by Daniel A. Jones at the UAH PRC High Pressure Lab [29].

Three different copper nozzles were used to vary the chamber pressure conditions of the solid tests. For each of the tests, the grain burned to completion, though

varying amounts of fine ash remained inside the motor grain after testing, as can be seen in Figure 5.1. As expected with the solid configuration, each test produced a significant amount of smoke in the exhaust plume. This plume is visible in Figure 5.2.

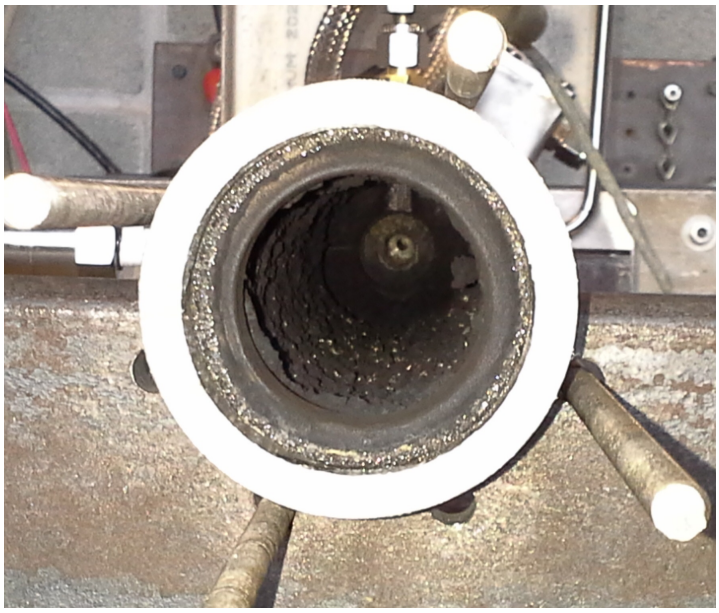

Figure 5.1: Ash deposits inside fuel grain after solid test.

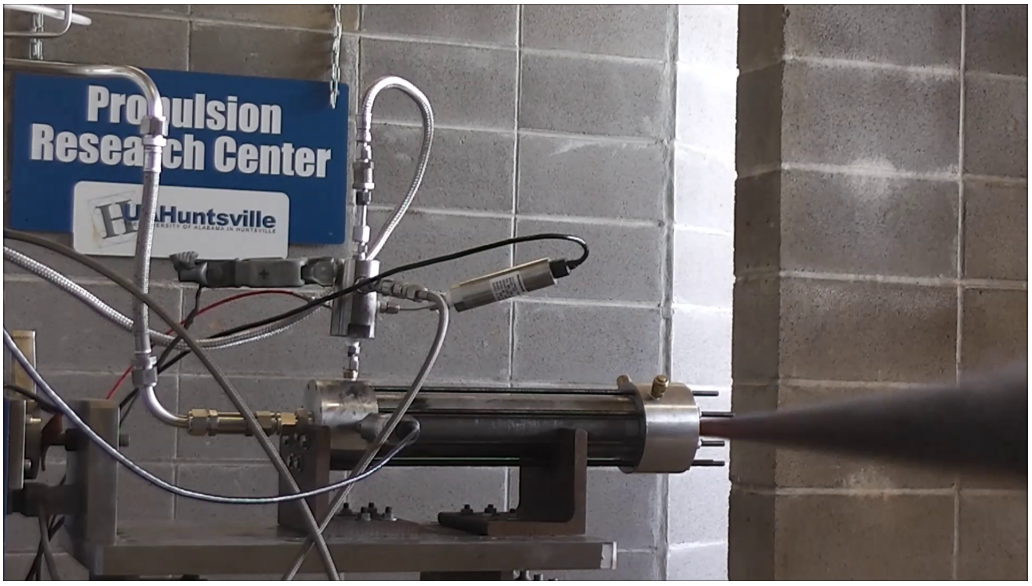

Figure 5.2: Exhaust plume from test 4-14.

Each test also observed an ignition transient and overspike in pressure as a result of ignition. The ignition delays observed in the first test and third test are nearly identical, while the ignition delays in the second and fourth test are longer but also similar. The ignition overspike is suspected to be a result of the hydrogen-oxygen torch igniter used during testing. It is believed that excess oxygen after igniter cut-off momentarily increases the characteristic velocity inside the motor, generating the pressure overspike. The measured pressure traces showing the overspike are included in Appendix C.

Every grain used in testing after the first and second solid tests were temperature conditioned to 70°F prior to testing. The fourth solid test was exposed to low ambient temperatures for approximately an hour prior to firing. Abel and Markopolous noted that preheating the motor resulted in a shorter ignition delay [19],

so it's possible the variations in ambient temperature led to the variation in ignition delay. A sample pressure trace showing the ignition transient, ignition time, burnout time, and dP/dt trace is provided for Test 4-3 in Figure 5.3.

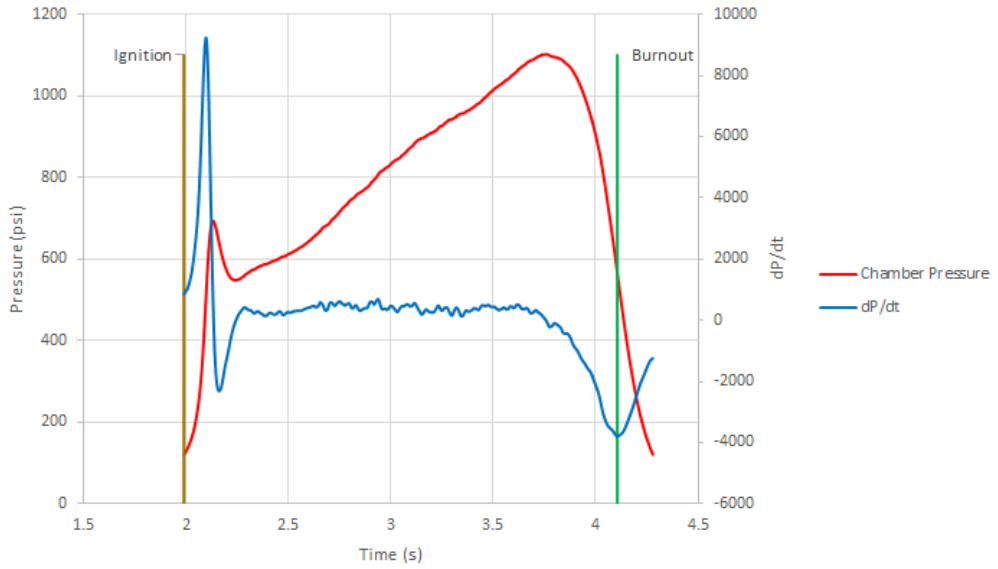

Figure 5.3: Pressure trace and event overlays for test 4-3, 0.2380" nozzle throat.

5.1.1 Static Test Results

The results of the solid tests are given in Table 5.2. For each test, the maximum chamber pressure did not occur at burnout, which is indicative of the bore not being centered. The grains selected for tests 4-1,4-2, and 4-3 were specifically chosen as grains that had a visibly crooked bore, so the maximum pressure was not expected to occur at burnout. These grains were selected in order to preserve the available straight-bore grains for the subsequent hybrid testing. As discussed in Chapter 4, the average pressure given for the solid tests is the rate averaged pressure.

The original targeted pressures for solid tests 4-1 and 4-2 were 500 and 1500 psi and the nozzle throat diameters were sized accordingly using a straight bore assumption. Post-test ballistics analysis recreated the observed pressure traces for test 4-1 and 4-2 using the 3D CAD modeling for the area of the burn as a function of web thickness, described in Chapter 4. The model confirmed that the crooked bores of both grains led to the lower than expected pressures. The grain used for test 4-3 was measured prior to nozzle sizing to determine the bore offset, and the nozzle was sized to achieve a maximum pressure of 1500 psi given this offset. During post-firing inspection, it was observed that combustion gases had leaked from around the outside of the nozzle, creating black sooty deposits on the outside of the copper nozzle. This can be observed in Figure 5.4.

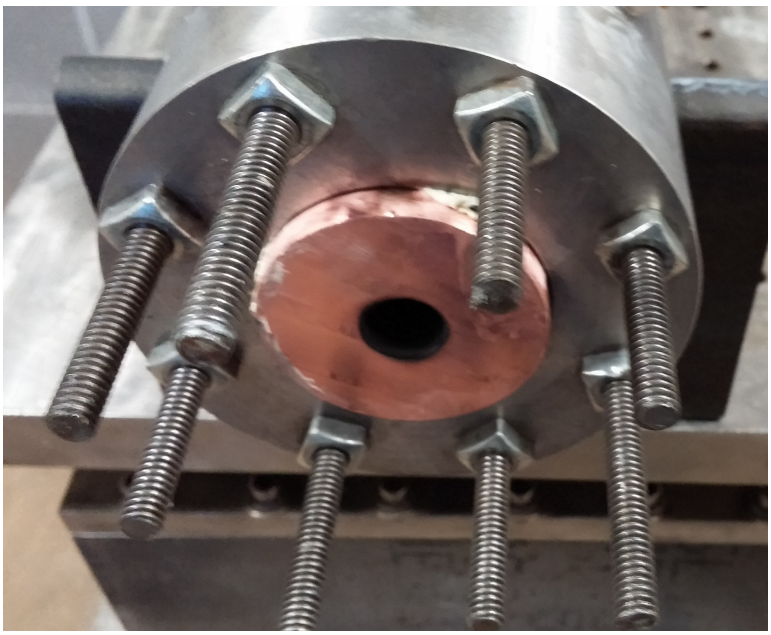

Figure 5.4: Sooty deposits on exterior of the nozzle after test 4-3.

After disassembling the motor components, it was discovered that the O-ring used to create a seal around the copper nozzle had failed. It was hypothesized that the O-ring had been pinched during the nozzle installation, causing it to break. Following this test, the copper nozzle was modified to reduce the likelihood of tearing the O-ring again. It is suspected that the lack of a proper seal around the nozzle caused the maximum chamber pressure to reach only 1100 psi instead of the expected 1500 psi.

Test 4-14 utilized a grain without a visibly crooked bore, although the maximum pressure did not occur at burn out, as can be seen in Figure 5.5. The most likely explanation for this is that the visual inspection and grain measurements did not account for a deformation in the bore, possibly at the middle of the bore rather than at the head or aft end of the grain.

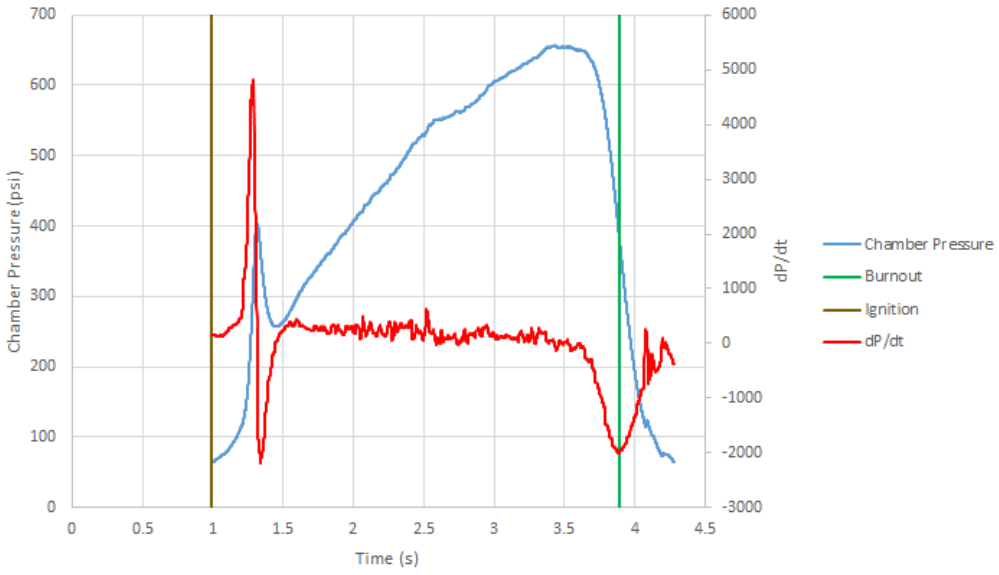

Figure 5.5: Pressure trace for test 4-14, 0.2610" nozzle throat.

Table 5.2: Summary of solid test data.

Test Number	4-1	4-2	4-3	4-14
Test Date	12/4/2014	12/15/2014	1/16/2015	2/10/2015
Nozzle Throat Diameter (in)	0.2969	0.2610	0.2380	0.2610
Burn Time (s)	3.436	3.061	2.115	3.275
Web Thickness Burned (in)	0.4210	0.4440	0.4500	0.4435
Average Burning Rate (in/s)	0.122	0.145	0.213	0.153
Maximum Burning Rate (in/s)	0.153	0.177	0.232	0.164
Mass of Fuel Burned (lbm)	0.988	0.994	1.008	0.996
Grain Density (lbm/in^3)	0.046	0.043	0.043	0.043
Average Chamber Pressure (psi)	273.0	405.2	780.3	439.4
Maximum Chamber Pressure (psi)	356.4	646.9	1102	656.5
Maximum Thrust (lbf)	28.83	50.31	84.32	57.87
Average Specific Impulse (s)	72.07	102.8	125.8	118.8
Characteristic Velocity Efficiency	65	68	73	68
Ignition Transient Duration (s)	0.266	0.465	0.247	0.461

5.1.2 Comparison with Results of Ultrasonic Testing

The Exquadrazine 6514 propellant is undergoing additional research at the UAH PRC. This testing, conducted by Daniel A. Jones of UAH, consists of ultrasonic combustion bomb testing of the propellant as a solid. This testing served to establish data on the burning rate of the propellant without additional oxidizer [29]. Additional testing may be completed to determine the temperature sensitivity of the grain.

The results of this ultrasonic testing are presented in Figure 5.6. Included on this figure are the four average regression rates and pressures measured from the solid tests. The motor test data extrapolates well within the data collected, although the average regression rates observed in the motor data are lower than the fit of regression

rate observed in the ultrasonic testing. The four UAH solid tests conducted for this research are identified as "UAH Solid Tests" on the graph; the remaining data on the graph are the various results calculated from the combustion bomb tests.

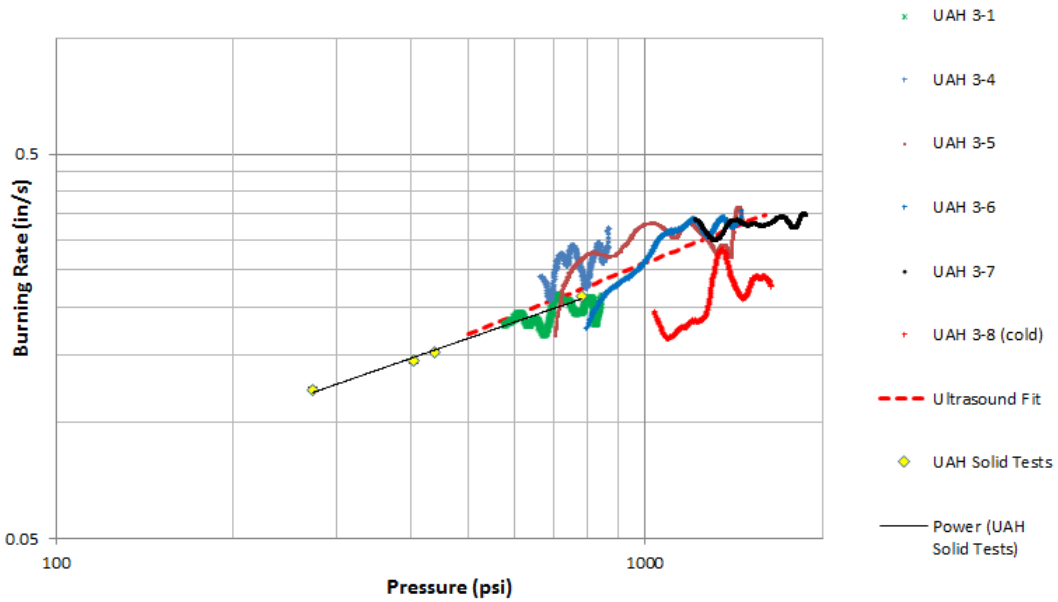

Figure 5.6: Summary of solid burning rate for all Exquadrazine 6514 testing at UAH.

An interesting point of note is the low temperature test data of the ultrasonic testing. This test was conducted at 40°F, 30 degrees lower than the ambient tests; the resulting regression rate for the cold temperature test is significantly lower than the ambient temperature tests. However, only a single low temperature test has been conducted to date, so this data is not conclusive.

5.2 Hybrid Testing

Eleven hybrid tests were conducted to determine the overall regression rate of the motor in a hybrid configuration. Tests were conducted at GOX mass flow rates of 0.1, 0.3, and 0.6 lbm/s, Each test condition was tested at least twice to demonstrate consistency in the data gathered, although on certain tests the GOX flow time was increased to increase the burn time. Figure 5.7 show the measured test configurations of average pressure and average oxidizer flux for each of the eleven tests, separated by the four targeted configurations. The corresponding average regression rates measured for each test are presented in Figure 5.8. Each hybrid test and it's corresponding configuration are also summarized in Table 5.3.

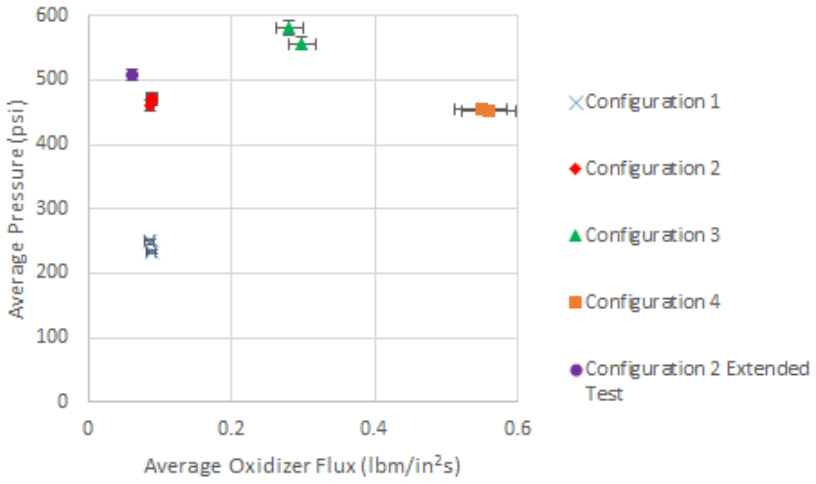

Figure 5.7: Recorded test configurations for hybrid testing.

Table 5.3: Summary of hybrid testing and configurations

Configuration	Nozzle Throat Diameter (in/s)	Targeted GOX Mass Flow Rate (lbm/s)	Test Number	Measured GOX Mass Flow Rate (lbm/s)
1	0.4375	0.100	4-4	0.092
			4-5	0.098
2	0.3750	0.100	4-6	0.100
			4-7	0.101
			4-8	0.101
			4-9	0.101
3	0.4375	0.300	4-10	0.302
			4-11	0.302
4	0.600	0.600	4-12	0.601
			4-13	0.594
2 Extended	0.3750	0.100	4-15	0.098

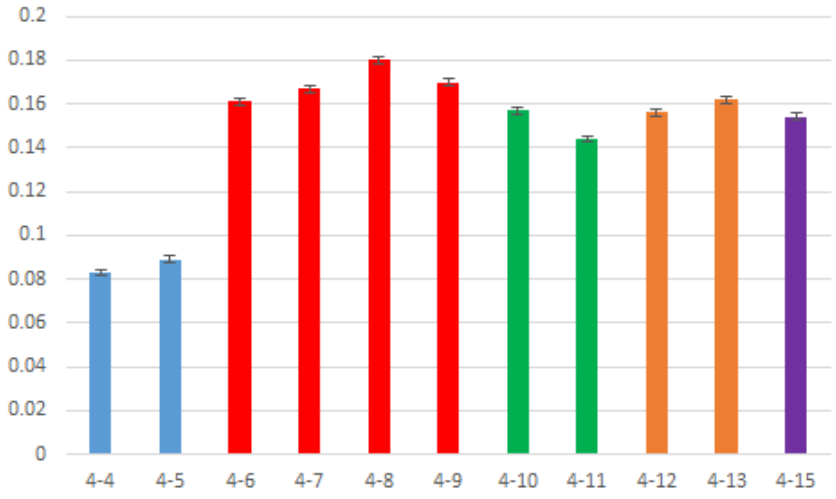

Figure 5.8: Recorded average regression rates for hybrid tests.

For each test condition except for the high flow (0.6 lbm/s) condition, a low frequency instability was observed. This instability produced significant pressure oscillations inside the motors, and was also observed both in video footage of the testing and audibly from outside the test area. The high flow hybrid tests did not show the same instability in the pressure data or video footage, and no instability was audible during testing. Figure 5.9 shows the pressure traces recorded from the third hybrid test condition, tests 4-10 and 4-11. These tests had a GOX flow rate of 0.3 lbm/s and a nozzle throat diameter of 0.4375 inches. Test 4-10 had a GOX flow duration of 1.0 seconds, while test 4-11 had a GOX flow duration of 1.3 seconds.

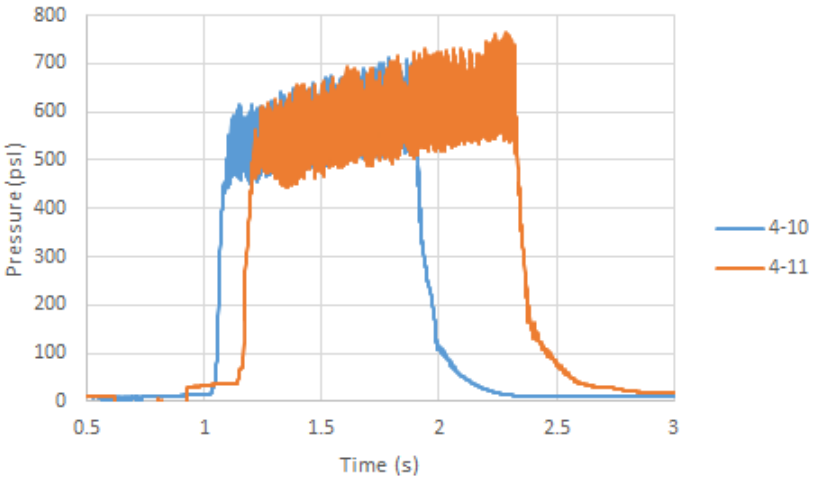

Figure 5.9: Pressure traces for hybrid tests 4-10 and 4-11, 0.4375" throat diameter, 0.3 lbm/s GOX flow rate.

At the higher flow rates, shown in Figure 5.10, the pressure trace did not show significant instability, and the pressure trace was approximately neutral throughout

the burn. These tests, test 4-12 and 4-13, had a GOX mass flow rate of 0.6 lbm/s with a 0.6 inch nozzle throat diameter.

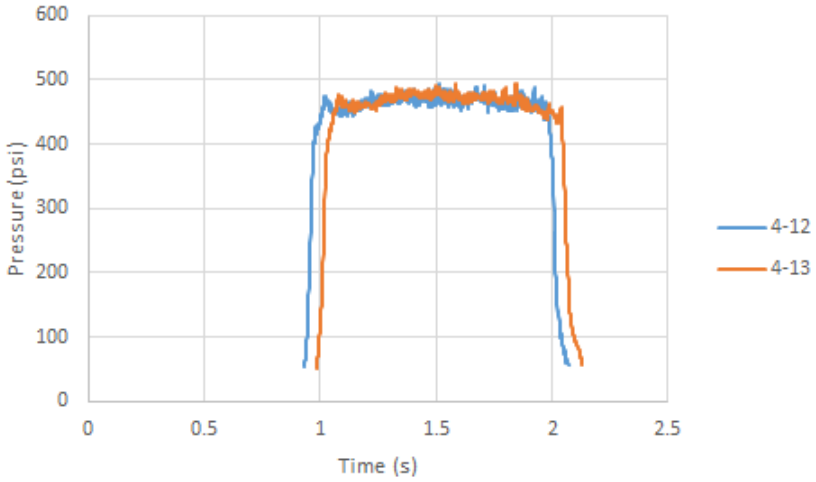

Figure 5.10: Pressure traces for hybrid tests 4-12 and 4-13, 0.6" throat diameter, 0.6 lbm/s GOX flow rate.

Tests conducted with the second configuration, 0.3750 inch nozzle diameter and 0.1 lbm/s, displayed burning of the grain beyond cutoff of the GOX flow. Four tests, test 4-6, 4-7, 4-8, and 4-9 were conducted with this configuration, and all four burned through the complete grain after GOX cutoff. The first two tests, 4-6 and 4-7 were conducted with no delay on the nitrogen purge used to flush the motor of combustibles post test; although the nitrogen purge operates behind a check valve, the motor chamber pressure dropped enough after GOX cutoff to allow the nitrogen purge to flow into the motor. This can be seen in Figure 5.11; the drop in pressure in the purge pressure traces indicate nitrogen flow. Prior to these tests, the motor chamber pressure had remained high enough to prevent the check valve from opening

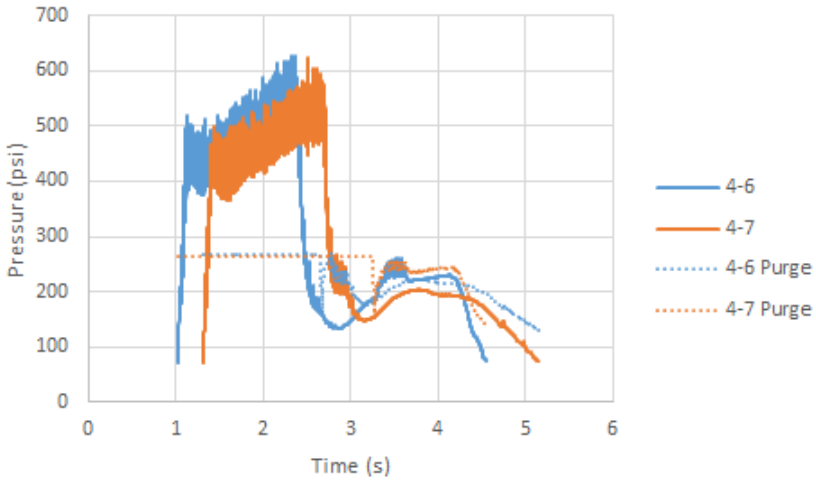

Figure 5.11: Pressure traces for hybrid tests 4-6 and 4-7, 0.375" throat diameter, 0.1 lbm/s GOX flow rate. Nitrogen purge pressures included to show nitrogen flow time.

until after burnout, and so as a safety factor it was standard procedure to open the purge after ignition to purge the motor in case of unexpected depressurization.

Tests 4-8 and 4-9 were conducted with a delay on the nitrogen purge so that the purge did not flow until after the grain had burned completely. The pressure traces of these two tests are presented in Figure 5.12. The nitrogen purge for both of these tests occurred at approximately 7 seconds after the start of data collection. In the pressure traces for 4-6, 4-7, 4-8, and 4-9, the continued burning of the grain is visible as the rise in pressure after the unstable combustion and pressure drop. It is suspected that the smaller throat diameter prevented the chamber pressure from dropping below the extinguishment limit for the propellant, and therefore the grain continued to burn.

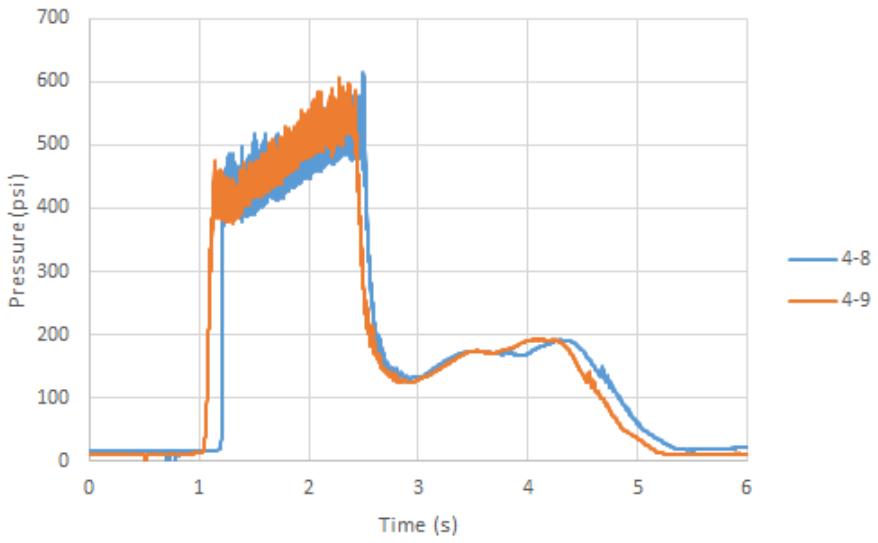

Figure 5.12: Pressure traces of hybrid tests 4-8 and 4-9, 0.375" throat diameter, 0.1 lbm/s. Grain did not extinguish on GOX cutoff.

5.2.1 Static Test Results and Discussion

The post-test analysis results of the eleven hybrid tests are presented in Table 5.4, Table 5.5, and Table 5.6. Overall, the hybrid tests show good consistency for tests conducted under the same configuration. Tests conducted at the same GOX mass flow rate and nozzle throat diameter but with different GOX flow times showed similar average burning rates and characteristic velocity efficiency, though as expected the average and maximum chamber pressures are higher, since the increase in burn time shifts the average values higher. This increase in pressure is caused by further burning of the progressive grain. This behavior can be witnessed between tests 4-4 and 4-5 as well as between tests 4-10 and 4-11.

Table 5.4: Summary of hybrid test data, tests 4-4, 4-5, 4-6, and 4-7.

Test Number	4-4	4-5	4-6	4-7
Test Date	1/27/2015	1/30/2015	2/3/2015	2/3/2015
Nozzle Throat Diameter (in)	0.4375	0.4375	0.3750	0.3750
GOX Flow Rate (lbm/s)	0.092	0.098	0.100	0.101
GOX Flux (lbm/in^2s)	0.088	0.085	0.085	0.084
Burn Time (s)	1.85	2.381	1.404	1.410
Web Thickness Burned (in)	0.157	0.212	0.217	0.201
Average Regression Rate (in/s)	0.083	0.089	0.161	0.167
Maximum Regression Rate (in/s)	0.093	0.102	N/A	N/A
Mass of Fuel Burned (lbm)	0.364	0.518	0.688	0.651
Grain Density (lbm/in^3)	0.050	0.052	0.042	0.043
Average Chamber Pressure (psi)	233.4	249.2	460.4	471.6
Maximum Mean Pressure (psi)	293.4	312.3	584.2	589.7
Maximum Chamber Pressure (psi)	326.5	347.9	623.8	628.6
Maximum Thrust (lbf)	90.81	90.75	108.7	N/A
Average Specific Impulse (s)	219.0	207.6	158.1	N/A
Characteristic Velocity Efficiency	85	82	94	100
Instability Frequency (Hz)	110	109	85	89
Instability Amplitude (psi)	33.07	35.58	39.62	38.89

Tests 4-6, 4-7, 4-8, and 4-9 were conducted with the 0.375 inch throat diameter configuration, and all four displayed continued burning as a solid after GOX cutoff. The analysis techniques to calculate the parameters summarized in Table 5.4 and Table 5.5 used the solid burning rate coefficients calculated from the four solid test results to determine the web thickness at the time of GOX cutoff. This web thickness was calculated from a backwards step assuming a web thickness of 0.0 inches at 10% of the maximum pressure.

Table 5.5: Summary of hybrid test data, tests 4-8, 4-9, 4-10, and 4-11.

Test Number	4-8	4-9	4-10	4-11
Test Date	2/5/2015	2/5/2015	2/6/2015	2/6/2015
Nozzle Throat Diameter (in)	0.3750	0.3750	0.4375	0.4375
GOX Flow Rate (lbm/s)	0.101	0.101	0.302	0.302
GOX Flux (lbm/in^2s)	0.084	0.085	0.299	0.281
Burn Time (s)	1.309	1.350	0.854	1.169
Web Thickness Burned (in)	0.211	0.211	0.134	0.169
Average Regression Rate (in/s)	0.180	0.170	0.157	0.144
Maximum Regression Rate (in/s)	N/A	N/A	0.19	0.152
Mass of Fuel Burned (lbm)	0.674	0.678	0.302	0.423
Grain Density (lbm/in^3)	0.042	0.043	0.050	0.055
Average Chamber Pressure (psi)	469.3	471.6	556.1	581.4
Maximum Mean Pressure (psi)	602.7	585.2	662.1	707.5
Maximum Chamber Pressure (psi)	613.3	610.2	718.0	768.8
Maximum Thrust (lbf)	97.02	104.6	206.7	237.9
Average Specific Impulse (s)	145.1	149.7	241.0	253.1
Characteristic Velocity Efficiency	94	95	75	77
Instability Frequency (Hz)	83	87	102	104
Instability Amplitude (psi)	10.53	25.05	55.94	61.36

This process was recognized as a large source of uncertainty in the post-test analysis, and so a final test was planned to operate under the same nozzle and mass flow conditions with GOX flowing throughout the duration of the burn. This was not standard procedure during testing to avoid the possibility of damaging motor components so this condition was only run for the last test, 4-15.

As described in Chapter 4, two regression rates were measured for each test. An average regression rate was measured using the average web thickness and burn time, while a maximum regression rate used the maximum change in web thickness

Table 5.6: Summary of hybrid test data, tests 4-12, 4-13, and 4-15.

Test Number	4-12	4-13	4-15
Test Date	2/10/2015	2/10/2015	2/10/2015
Nozzle Throat Diameter (in)	0.6000	0.6000	0.3750
GOX Flow Rate (lbm/s)	0.601	0.594	0.098
GOX Flux (lbm/in^2s)	0.560	0.549	0.060
Burn Time (s)	1.081	1.072	2.876
Web Thickness Burned (in)	0.169	0.174	0.444
Average Regression Rate (in/s)	0.156	0.162	0.154
Mass of Fuel Burned (lbm)	0.377	0.384	1.003
Grain Density (lbm/in^3)	0.051	0.050	0.043
Average Chamber Pressure (psi)	451.2	453.8	507.8
Maximum Regression Rate (in/s)	0.181	0.187	0.167
Maximum Mean Pressure (psi)	493.8	494.7	655.7
Maximum Chamber Pressure (psi)	493.8	494.7	691.0
Maximum Thrust (lbf)	283.2	276.6	133.9
Average Specific Impulse (s)	234.9	236.2	226.3
Characteristic Velocity Efficiency	81	81	96
Instability Frequency (Hz)	N/A	N/A	65/90
Instability Amplitude (psi)	N/A	N/A	35.32

divided by the burn time. For tests 4-6, 4-7, 4-8, and 4-9, the maximum change in web thickness could not be reported for the hybrid portion of the test since the grain continued to burn when the GOX flow was stopped.

The average regression rates measured for tests 4-6, 4-7, 4-8, and 4-9 are among the highest regression rates observed during testing, although the average pressure and average oxidizer flux values are lower than that of tests 4-10 and 4-11. It is suspected that since these four tests displayed burning after GOX cutoff, the post-test analysis added additional uncertainty and therefore skewed the average regression

rate results. Test 4-15, conducted under the same GOX mass flow rate and nozzle throat diameter as 4-6 through 4-9, displayed a lower average regression rate than the original four tests at this condition. However, this average regression rate was still higher than test 4-11, which was conducted at a higher average pressure and average oxidizer flux.

Since an increase in either chamber pressure or oxidizer flux should result in an increase in regression rate, there are two likely reasons for this regression rate behavior. Measurement uncertainty most likely is one reason why the regression rates display unusual behavior, although another contributor could be the grain design itself. The Exquadrazine motor grains are progressive, creating a non-neutral pressure trace, which means that the pressure that corresponds to the average burning rate is not the average pressure [22], as discussed in Chapter 2.

5.2.2 Static Test Instability Measurements and Discussion

A low-frequency instability was observed in each hybrid test except for the high-flow tests, 4-12 and 4-13. To characterize this instability, each upper and lower peak of the instability amplitude was identified, and an average peak-to-peak amplitude was calculated from the recorded pressure data. To determine the instability frequency, a Fast Fourier Transform (FFT) was performed on the pressure data for the duration of the instability. Figure 5.13 shows the FFT result from hybrid test 4-15.

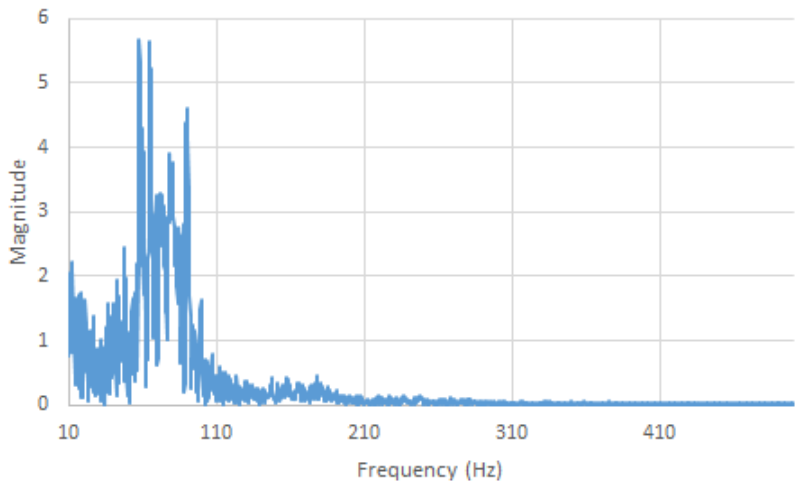

Figure 5.13: Fast Fourier transform of pressure data, test 4-15.

The initial spike at 0 Hz and the high values observed in very low frequencies ($< 10Hz$) are caused by a DC offset and have been removed from the plot. The two frequency peaks identified in this FFT analysis, as reported in Table 5.6, occur at 65 Hz and 90 Hz. Since the data was recorded at only one frequency (1000 Hz), there was the possibility that the frequencies observed during the hybrid testing were not physical frequencies, but instead aliased values of higher frequency oscillations above the 1000 Hz rate of data collection. To verify the observed frequencies, high speed video footage was taken at a rate of 1700 frames per second during test 4-15. Since an aliased signal would appear at a different frequency if measured with a different sample rate, altering the frame rate of the camera allowed for a verification of the instability frequency.

A program was developed to import the images collected from the high speed footage and perform a Fast Fourier Transform analysis on the images. Each image

was converted into an overall "light intensity" value by summing the grayscale bitmap values of each pixel in the entire frame. The higher the light intensity value for a frame, the lighter the overall image. Since the instability changed the size of the plume, the light intensity of each frame changed with the instability. Figure 5.14 shows a comparison of high speed images from test 4-15 to illustrate the change in light intensity due to the instability.

Figure 5.14: High speed footage comparison of successive frames for test 4-15.

The resulting FFT of the high speed footage for test 4-15 is presented in Figure 5.15. The mean has been removed from the light intensity values shown in the FFT plot. The frequencies observed in the light intensity FFT match those of the pressure data FFT for test 4-15, despite the difference in sampling rates. As a result, it can be concluded that the instability frequencies observed during testing were physical frequencies.

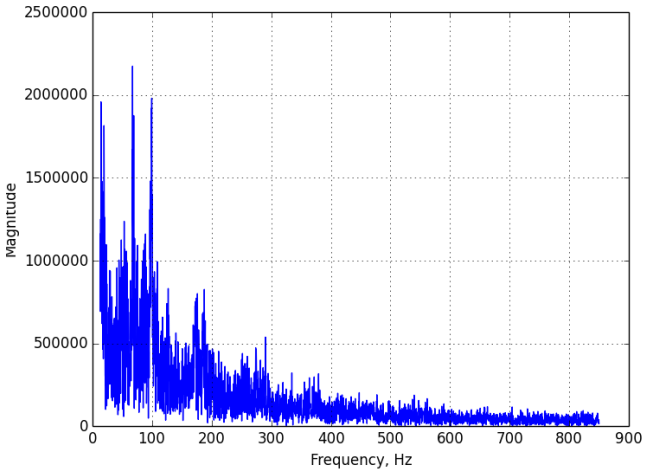

Figure 5.15: Fast Fourier transform of the high speed footage from test 4-15.

5.3 Regression Rate Model Results

The regression rate modeling was conducted in two parts by determining the solid and hybrid coefficients separately. The constants determining the pressure dependence aP^n were determined first by using the four solid tests. An initial optimization sequence, as described in Chapter 4, used a coarse grid search among the experimental constants a and n, and a trend in the results became apparent. The square errors were normalized from the results by dividing each error by the average square error of every equation considered for a given analysis. The average error varies based on the number of equations considered and the corresponding results for each equation, so this process gives a reference of the relative accuracy of one equation to any other considered within the same search, but not the overall accuracy.

For clarity, these values that have been divided by the average were referred to as 'normalized errors'.

The results of the initial coarse grid search for the solid constants are plotted in Figure 5.16. Figure 5.17 shows the results of the coarse grid search that resulted in normalized errors below 1.0, or 100%. There exists a range of values among a and n that produce low square errors in the prediction of chamber pressure. This relationship is shown in Figure 5.18, which shows each combination of a and n that produce a normalized error less than 5%.

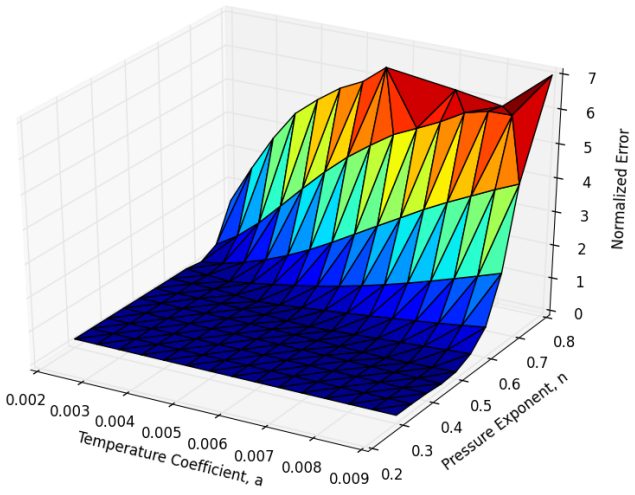

Figure 5.16: Initial optimization results for solid regression rate, coarse grid, all solid tests.

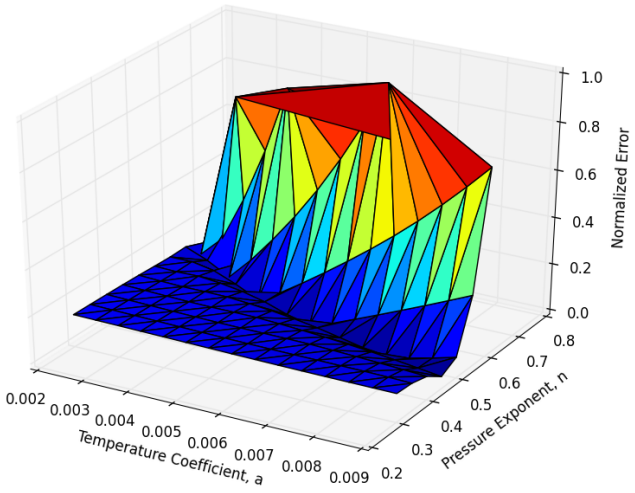

Figure 5.17: Solid regression rate coarse grid results below 100% normalized error, all solid tests.

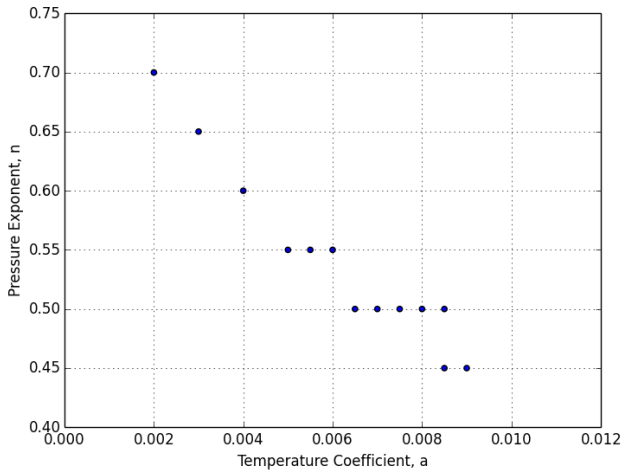

Figure 5.18: Plot of a and n pairs that produce below 5% error for solid regression rate, all solid tests.

Following the initial coarse grid search, refined searches were made using the optimization sequence with a fine grid to determine an absolute minimum average percent error for the solid regression rate. The results of this search are given in Figure 5.19. The regression rate equation for the solid tests is given in Equation (5.1).

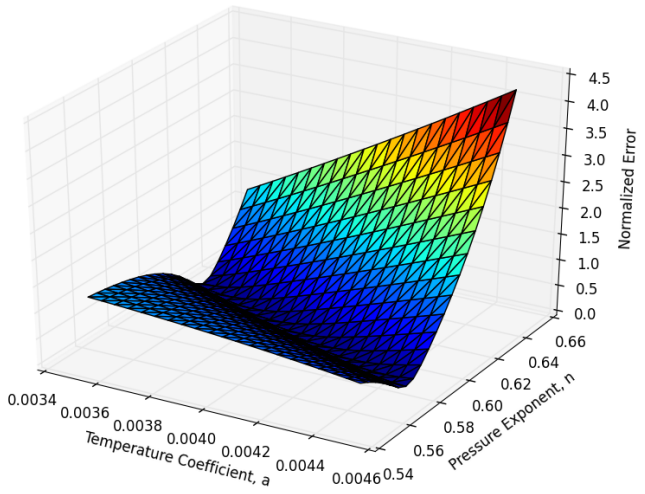

Figure 5.19: Refined optimization results for solid regression rate, fine grid, all solid tests.

$$\dot{r} = 0.0044P^{0.585} \tag{5.1}$$

Once the solid regression rate equation was determined, the values of a and n were fixed, and the optimization sequence was run to determine the remainder of the experimentally determined constants, b and q. The results of the coarse grid optimization search are given in Figure 5.20. For tests with an observed instability

during the hybrid testing, a moving average of 20 points (0.02 seconds) was used to smooth the measured pressure data for comparison. For these calculations, only the hybrid tests that extinguished at the cutoff of GOX flow were considered. Tests 4-6, 4-7, 4-8, and 4-9 were not considered as the grain continued burning without GOX flow, and therefore the analysis of these tests were dependent on the results of the solid analysis. For clarity, Figure 5.21 shows the coarse grid results for the hybrid tests with only the normalized errors below 100%.

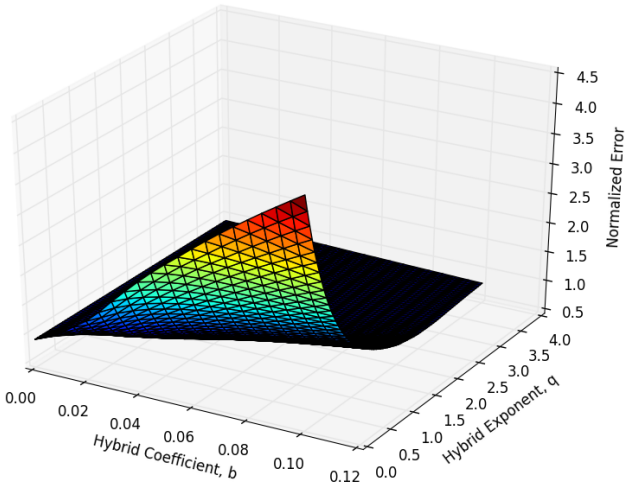

Figure 5.20: Initial optimization results for hybrid regression rate, coarse grid, all extinguishing hybrid tests.

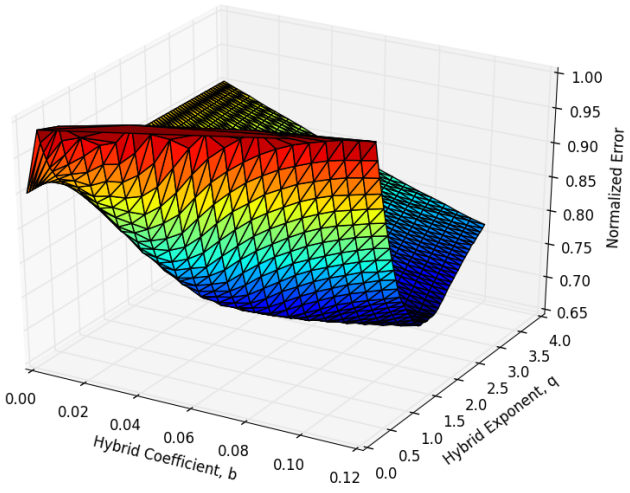

Figure 5.21: Results for hybrid regression rate with normalized error below 100%, coarse grid, all extinguishing hybrid tests.

A fine grid search was used to identify the hybrid constants b and q in the regression rate equation, as shown in Figure 5.22. The combination of hybrid constants that return a normalized error below 100% are given in Figure 5.23. The minimum error hybrid equation from the optimization searches conducted is given in Equation (5.2).

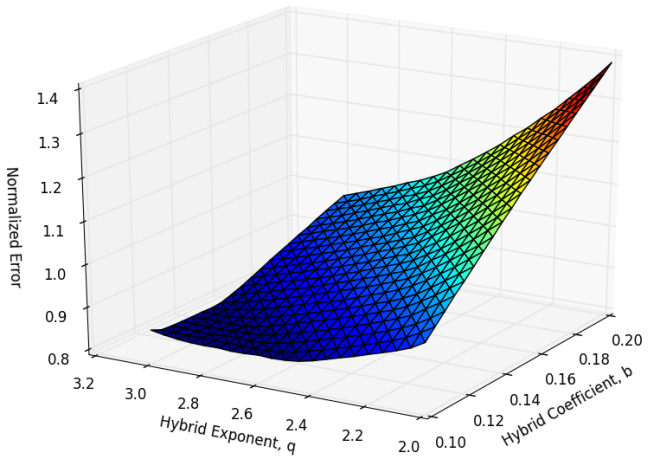

Figure 5.22: Refined results for hybrid regression rate, fine grid, all extinguishing hybrid tests.

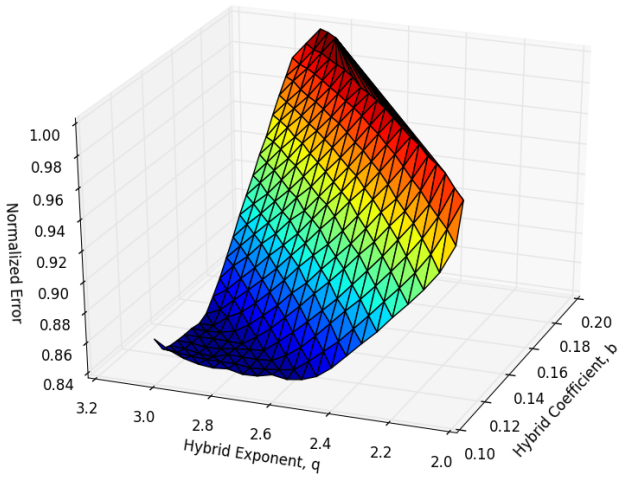

Figure 5.23: Results for hybrid regression rate with normalized error below 100%, fine grid, all extinguishing hybrid tests.

$$\dot{r} = 0.0044P^{0.585} + 0.11G_{ox}^{2.85} \tag{5.2}$$

5.3.1 Discussion of Regression Rate Model

As a validation of the solid regression rate equation calculated, the coarse search results for normalized error below 5% were used to generate regression rate vs. pressure curves and plotted along with the measured average regression rates from the solid testing, shown in Figure 5.24. In this figure, the dashed lines are the combinations of a and n that produced a normalized error below 5%, while the solid red line corresponds to the calculated equation given in Equation (5.1). The blue squares are the measured average regression rates for the solid tests.

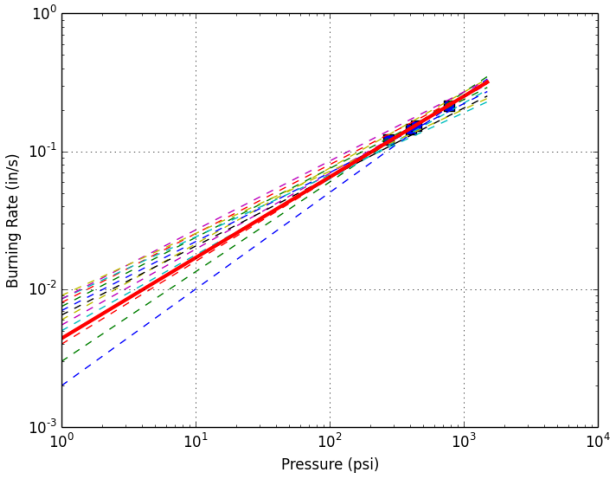

Figure 5.24: Burning rate vs. pressure for coarse results below 5% normalized error, all solid tests.

One of the trends observed in the solid regression rate optimization was the existence of a range of equations producing low normalized errors. One observation that can be made from Figure 5.24 is the close spread of average pressures from the test data. One possible way to discern a clear minimum error in the regression rate equation would be to increase the range of test conditions so that there is more variation in average pressure between tests.

To verify the results of the regression rate model against individual test data, plots were created showing the measured and predicted values of pressure for individual tests. The solid test that best fit the regression rate model was 4-2, shown in Figure 5.25. The least accurate fit for a solid test, test 4-14, is shown in Figure 5.26. This test was performed using a grain with an approximately straight, although the pressure test indicates that the grain had more of an offset or deformity to the bore than initially realized.

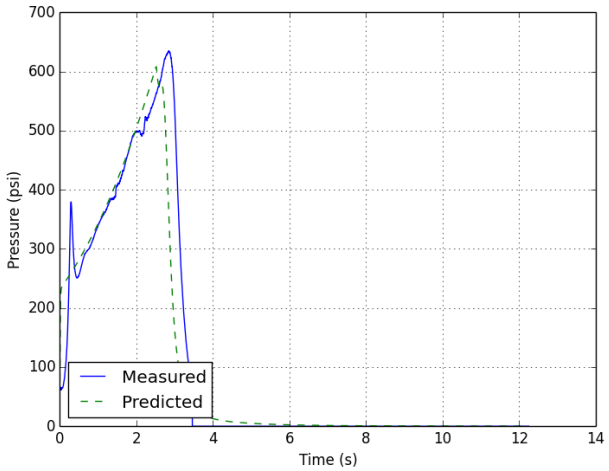

Figure 5.25: Predicted and measured pressure traces for test 4-2.

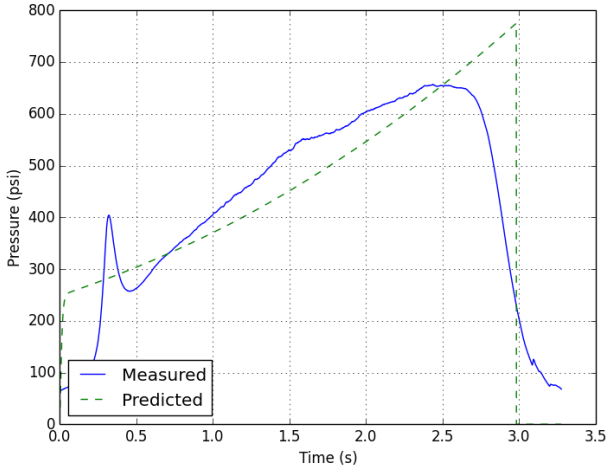

Figure 5.26: Predicted and measured pressure traces for test 4-14.

Of the hybrid tests, 4-10 fit the model with the smallest square error, shown in Figure 5.27. The largest square error for a hybrid test was test 4-5, given in Figure 5.28. The high flow tests, 4-12 and 4-13, showed a predicted curve that behaved in a different way than the measured pressures, as can be seen in Figure 5.29. The predicted pressure traces for the high flow tests showed a decrease through the middle of the burn, followed by an increase before burnout, while the measured pressures increased through the middle of the burn and decreased at burnout. It is possible that this inflection point in the predicted tests are a result of a change in the relative influence of the solid and hybrid terms of the regression rate equation.

For the measured data, which increased in pressure through the middle of the burn duration and then decreased near the end of the burn, it is possible this is a result of the characteristic velocity changing with the O/F ratio. As referenced in Chapter 4, the characteristic velocity shifts with O/F ratio, and a maximum char-

acteristic velocity is obtained at stoichiometric conditions. It is possible that as the grain burned, the O/F shifted through this maximum, and that the resulting increase and subsequent decrease of characteristic velocity caused the similar behavior observed in the pressure trace for the high flow condition.

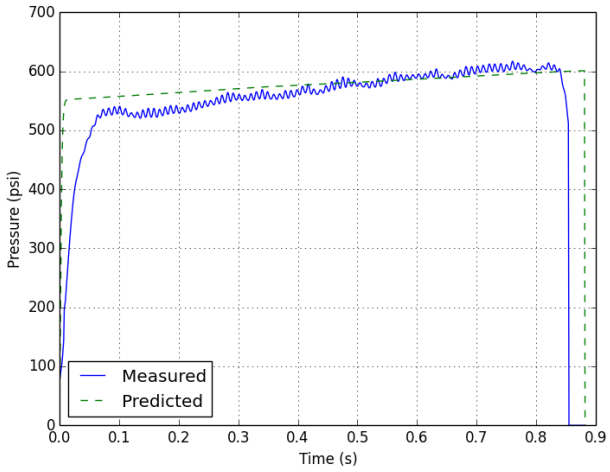

Figure 5.27: Predicted and measured pressure traces for test 4-10.

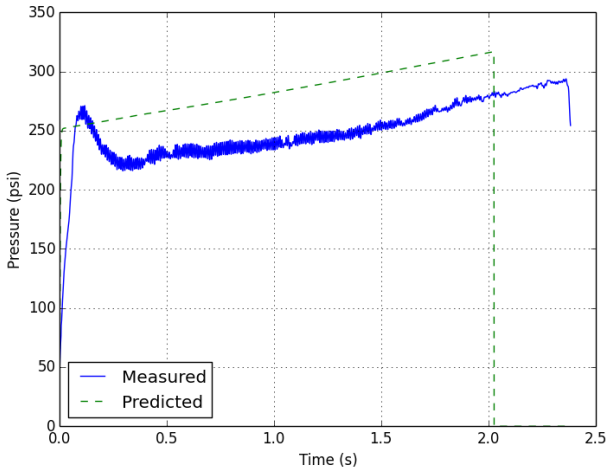

Figure 5.28: Predicted and measured pressure traces for test 4-5.

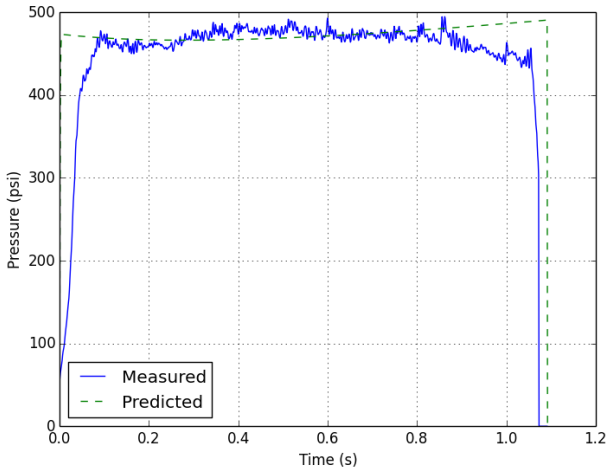

Figure 5.29: Predicted and measured pressure traces for test 4-13.

The predicted and measured pressure traces for each test are given in Appendix E. Several of the predicted pressure traces appear to be shifted in a manner that suggests that a different characteristic velocity efficiency could provide a very

Table 5.7: Measured characteristic velocity efficiency and efficiency within 4% that produces a minimum error for solid tests and hybrid extinguishing tests.

Test	Measured Efficiency	Minimum Error Efficiency	Change in Efficiency
4-1	65	69	4
4-2	68	65	3
4-3	73	73	0
4-4	85	81	4
4-5	82	78	4
4-10	75	78	3
4-11	77	73	4
4-12	81	79	2
4-13	81	83	2
4-14	68	69	1
4-15	96	92	4

accurate fit between the predicted and measured traces. The calculated efficiency and the minimum error efficiency within 4% of the measured efficiency are presented for in Table 5.7 for each test. This 4% variation in characteristic velocity efficiency was chosen as the uncertainty analysis showed a 95% confidence interval for values of efficiency within ±4% of the value calculated during the post-test analysis.

As a final test of the calculated regression rate model, the prediction code was modified to do a complete prediction of the hybrid configuration that displayed burning of the grain as a solid after GOX cutoff (tests 4-6, 4-7, 4-8, and 4-9). The ballistics code was modified in three ways:

- The GOX cutoff time was added.
- At GOX cutoff, the code changes the GOX flow rate to 0.0 lbm/s.

- At GOX cutoff, the code changes the combustion efficiency.

The combustion efficiency after GOX cutoff was calculated using the mass flow rate of fuel after GOX flow from the cutoff time until the end of the action time. The code was successful in predicting the burning as a solid after GOX cutoff, as can be seen in Figure 5.30. The pressure trails off at the end of the measured values, which most likely is indicative of a slightly offset bore at the end of the burn.

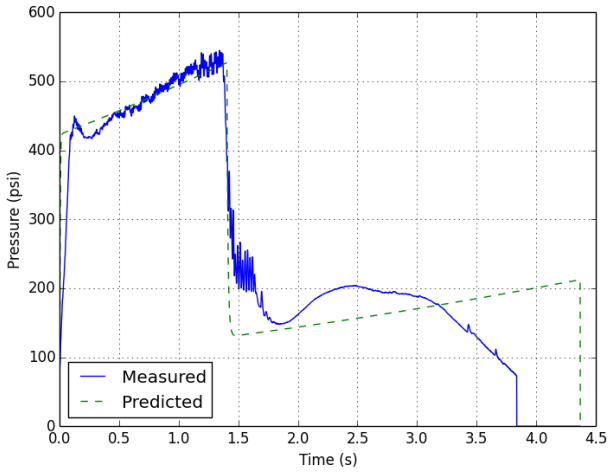

Figure 5.30: Predicted and measured pressure traces for test 4-6.

5.3.2 Input and Regression Rate Uncertainties

The uncertainty in the measurement variables is presented in Table 5.8. These values were then used to calculate the uncertainty in the calculated values from the post-test analysis that were used as inputs for the ballistics analysis. The uncertainty of the chamber pressure measurements was calculated using both the systematic uncertainty listed in the specifications of the pressure transducer, as well as the random

Table 5.8: Uncertainty values for variables used in post-test analysis.

Variable	Symbol	Units	Uncertainty
Initial mass	m_{pre}	lbm	0.0011
Final mass	m_{post}	lbm	0.0011
Web thickness	w_i	in	0.0005
Port radius	r_p	in	0.005
Grain length	l	in	0.0005
Nozzle throat diameter	d_t	in	0.0035
Venturi throat diameter	d_v	in	0.0025
Specific heat ratio	γ		0.050
Venturi gas temperature	T	K	1.800
Theoretical characteristic velocity	$C^{\star}_{R,P}$	ft/s	75.00
Venturi pressure	P_v	psi	3.460
Gas constant of combustion products	R	$\frac{ft*lbf}{lbm*R}$	15.60
Chamber pressure	P	psi	1.820

uncertainty in the measurements. This random uncertainty was taken as twice the standard deviation of the pressure measurements through the burn on test 4-4, divided by the square root of the number of measurements to give an uncertainty of the average chamber pressure. The uncertainty listed for chamber pressure in Table 5.8 was calculated using these two values according to Equation (5.3), where U_R is the random uncertainty and U_S is the systematic uncertainty [28].

$$U_P = \sqrt{U_R^2 + U_S^2} \tag{5.3}$$

The calculated uncertainties in the post-test analysis are given in Table 5.9. For the calculation of the uncertainty in the post-test analysis, the measurements from

Table 5.9: Expanded uncertainty values for post-test analysis calculations.

Calculated Value	Symbol	Units	Uncertainty	Percent Uncertainty
Web thickness	w_{pre}	in	0.0003	0.06
Average burning rate	$\bar{\dot{r}}_b$	in/s	0.0031	3.76
Grain density	ρ_p	lbm/in^3	0.0079	15.7
Oxidizer mass flow rate	$\dot{m}_{ox}$	lbm/s	0.0059	6.41
Oxidizer flux	G_{ox}	lbm/s*in^2	0.0179	6.59
Nozzle throat area	A_t	in^2	0.0024	1.60
Burn time	t_b	s	0.0707	3.75
Characteristic velocity	$c^\star$	ft/s	148.2	3.97
Gas to solid ratio	$\frac{G}{S}$		0.0355	7.44
Predicted characteristic velocity	$C^\star_{pred,R,P}$	ft/s	85.31	1.82
Characteristic velocity efficiency	$\eta_{c^\star}$		0.0366	4.54

hybrid test 4-4 were used. It was assumed that the corresponding percent uncertainty from the analysis on test 4-4 was representative of fifteen tests.

These calculated uncertainty values were used as inputs for the ballistic analysis in order to determine the uncertainty in average regression rate calculated by the proposed regression rate model. A Monte Carlo analysis was used to determine the uncertainty by randomly selecting the input values for these parameters from a Gaussian distribution with mean centered on the calculated value, and the standard deviation as half of the calculated uncertainty given in Table 5.9. The input values varied were:

- Propellant density, ρ_p
- Nozzle throat diameter, d_t

- Characteristic velocity efficiency, $\eta_{c^\star}$
- Oxidizer mass flow rate, $\dot{m}_{ox}$
- Pre-test web thickness, w_{pre}

The Monte Carlo analysis was performed on test 4-4 with 5000 iterations. The results of this uncertainty analysis, along with the calculated regression rates from each extinguishing hybrid test and the solid tests are given in Figure 5.31. The predicted regression rates for each test along with the expanded uncertainties are given in Table 5.10.

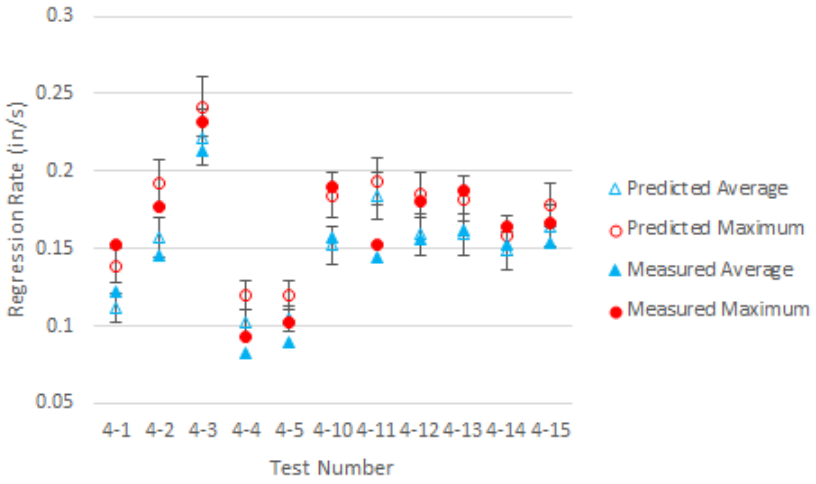

Figure 5.31: Predicted and measured average regression rates.

Table 5.10: Predicted and measured regression rates for solid tests and extinguishing hybrid tests.

Test	Average Predicted Regression Rate	Average Measured Regression Rate	Maximum Predicted Regression Rate	Maximum Measured Regression Rate
4-1	0.111 ± 0.009	0.122 ± 0.005	0.139 ± 0.011	0.153 ± 0.006
4-2	0.157 ± 0.013	0.145 ± 0.005	0.193 ± 0.015	0.177 ± 0.007
4-3	0.222 ± 0.018	0.213 ± 0.008	0.242 ± 0.019	0.232 ± 0.009
4-4	0.102 ± 0.008	0.083 ± 0.003	0.120 ± 0.009	0.093 ± 0.003
4-5	0.105 ± 0.009	0.089 ± 0.003	0.120 ± 0.009	0.102 ± 0.003
4-10	0.152 ± 0.013	0.157 ± 0.006	0.184 ± 0.015	0.190 ± 0.007
4-11	0.184 ± 0.015	0.144 ± 0.005	0.194 ± 0.015	0.152 ± 0.006
4-12	0.159 ± 0.013	0.156 ± 0.003	0.185 ± 0.015	0.181 ± 0.007
4-13	0.159 ± 0.013	0.162 ± 0.006	0.182 ± 0.014	0.187 ± 0.007
4-14	0.149 ± 0.012	0.153 ± 0.006	0.159 ± 0.013	0.164 ± 0.006
4-15	0.165 ± 0.014	0.154 ± 0.006	0.179 ± 0.014	0.167 ± 0.006

Each test with the exception of 4-4, 4-5, and 4-11 had good agreement between the predicted and measured regression rates for both the average and maximum rates. Tests 4-4, 4-5, and 4-11 consistently had predicted regression rates that were higher than those of the measured values. The regression rates for the solid tests, as well as the curve fit of the regression rate model are provided in Figure 5.32. As can be seen on this figure, the average regression rate results agree better with the model than the maximum regression rate results.

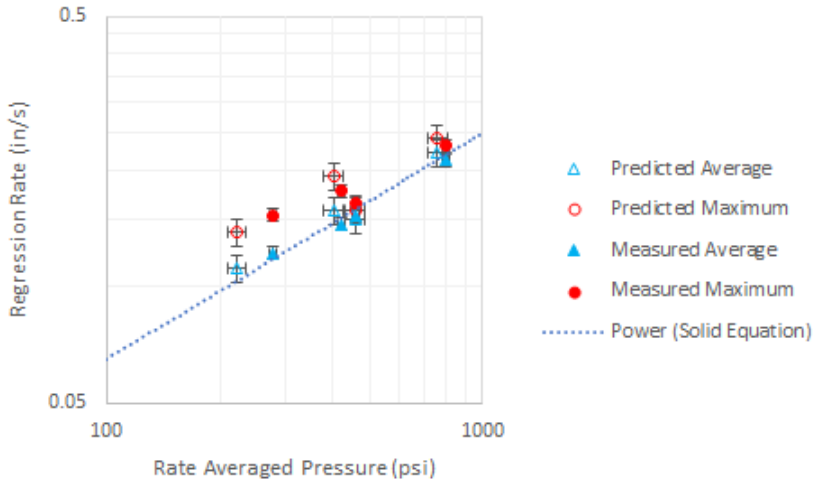

Figure 5.32: Predicted and measured regression rates for all solid tests.

CHAPTER 6

CONCLUSIONS

6.1 Conclusions

Fifteen tests of a center port, mixed oxidizer hybrid motor using Exquadrazine 6514 with and without gaseous oxygen were conducted to determine the regression rate model. The tests without gaseous oxygen showed reasonable agreement with concurrent testing using ultrasonic combustion bomb regression rate measurement techniques. The use of CAD modeling to recreate the burning surface area of the grain proved effective in recreating the pressure traces encountered during testing. The testing also showed that for hybrid tests conducted with a 0.375 inch throat diameter, the grain did not extinguish upon cutoff of the oxygen flow. This validated the proposed linear combination regression rate model which enables regression of the solid grain without oxidizer flux through the bore.

The optimization sequence identified a best-fit model of $\dot{r}_{bore} = 0.044P^{0.585} + 0.11G_{ox}^{2.85}$ for the regression of the bore, and $\dot{r}_{ends} = 0.044P^{0.585}$ for the regression of the ends. This model showed good agreement when comparing the average and maximum regression rates from the model with the rates measured during testing. A fit of the average pressure to average regression rate gives a solid regression rate

of $\dot{r}_{solid} = 0.006P^{0.531}$. The average regression rate results from the ballistic analysis agree very well with the calculated regression rate model. The exponent on the GOX term, 2.85, is higher than any value encountered in the review of the literature.

The proposed regression rate model was shown to be capable of calculating a predicted pressure trace for a non-extinguishing hybrid condition that displayed both burning with and without gaseous oxidizer flow. This analysis may be useful in applications which require both a 'boost' and 'cruise' phase of motor operation, where a gas generator mixed oxidizer hybrid may be used with and without oxidizer to provide changes in thrust. The proposed model can be used in a ballistics analysis to predict such an operating profile.

A possible reason for the high exponent is due to the nature of the optimization sequence and comparison of error between regression rate coefficients. The square error method proposed above will compare a specific pressure point against zero if there is not both a measured and a predicted pressure at that given time. As such, the error is significantly higher for a predicted burn time that is either shorter or longer than the measured time. The solid tests, which approach zero at burnout due to the crooked grain, should not bias this answer too much, but the hybrid tests extinguish at high pressures, so any variation in burn time between the predicted and measured should have significant effects on the error calculated. The ballistic analysis will iterate until the input web thickness is burned, so the optimization sequence most likely is driving towards a regression rate equation that most closely matches the burn time while still burning the given web thickness. It is possible that errors in the measured web thickness, or an inability to accurately capture the web

thickness throughout the bore, may have a significant effect on biasing the regression rate model selected due to this behavior.

The ignition transients observed during testing showed ignition delays, and in some cases ignition overspikes. These transients were not modeled in the ballistic analysis code, and may have biased the best fit regression rate model. The observed ignition delays have the effect of translating the measured pressure trace in time. The 'ideal' best fit model should show burnout earlier than that of the measured test by the same duration as the ignition delay, since the ignition delay is not modeled in the ballistics code. This 'ideal' model may have an increased error over other models however, as the ignition delay has the effect of de-syncing the measured and predicted pressures, causing an increase in square error at the beginning and end of the data. This increase in square error may mean that the calculated model may be biased towards slower regression rates to ensure burnout at the same time as the measured pressure.

A low-frequency instability was observed during the hybrid testing for all tests except for the high flow (0.6 lbm/s) configuration. The oscillation frequency measured through the chamber pressure was confirmed to be a physical frequency through analysis of high speed footage during testing. The frequencies encountered varied from approximately 85 Hz to 105 Hz, with the lower frequency occurring at the small nozzle throat configuration. Since the instability occurs only at low flow rates, it is possible that the instability is similar to those encountered in solid rockets, and relates to the characteristic length of the motor. This may explain the observed relationship between instability frequency and nozzle size.

6.2 Recommendations for Future Research

The optimization results for both the solid and hybrid tests displayed a range of values which produced low, but not the minimum, errors in predicting the pressure traces. Ideally, the minimum values would be more defined, and it is suspected that a lack of sufficient variation in test configurations could lead to the observed optimization results. Future testing should investigate larger ranges of pressures for both solid and hybrid tests, as well as larger variations in oxidizer flux.

Several of the grains tested used had deformities or offsets in the center bore leading to difficulties in recreating the chamber pressures. Modeling the burn surface areas in CAD software helped to correct this issue, but future testing should repeat these test conditions with satisfactory grain geometry to validate the results of this work. Future testing should also investigate the effect of grain bulk temperature on the regression rate. Solid rocket motors show significant variation in regression rate as a function of temperature, while classical hybrid rocket motors do not. The temperature sensitivity of this mixed oxidizer hybrid configuration has not been investigated yet.

Additional instrumentation could be placed on the oxidizer feed lines in front of the injector, as well as instrumentation on the aft end of the chamber to aid in the understanding of the instabilities observed during hybrid testing. If the instability is feed system related, a pressure transducer directly in front of the injector should observe the same instability in the feed line as measured in the chamber.

The optimization code and ballistic analysis code should be analyzed to determine the sensitivity to the various inputs. Since the ballistics code iterates through the maximum web thickness, the optimum regression rate model may be highly dependent on the measured web thicknesses. Improvements can be made to the uncertainty calculation as well by conducting the uncertainty analysis on each individual set of test data. The overall accuracy of the optimization code should be increased by modeling the ignition transients that were observed during testing.

APPENDICES

APPENDIX A

COMBUSTION INSTABILITY IN HYBRID ROCKETS

Hybrid rocket engines commonly suffer from two types of instabilities; a low frequency non-acoustic instability induced by the feed system, and an acoustic flame holding instability [1]. The flame holding instability typically arise due to poor flame stabilization in the boundary layer, and the frequency typically occurs at the first longitudinal mode of the motor [1]. Crygogenic or systems, such as LOX systems, tend to suffer from feed system instabilities due to compressibility of the oxidizer flow [30] [1]. Non-cryogenic oxidizers, such as hydrogen peroxide, do not suffer from two-phase flow or vapor cavities, which reduces the compressibility of the oxidizer and therefore helps eliminate the feed system instabilities [30].

Karabeyoglu et. al. observed varying instability frequencies in high-regression rate paraffin wax motors of 30, 100, and 350 hz. The 30 hz was identified as a fuel production instability triggered by vortex shedding off the injector. The 100 Hz instability was identified as the Helmholtz mode of the chamber, which is related to the volume inside the chamber. The 350 Hz frequency came from the longitudinal half wave within the motor [31].

A common method to provide sufficient flame stabilization in the boundary layer and therefore reduce the acoustic instability is to preheat the oxidizer before as it enters the combustion chamber [1]. In AMROC's 250,000 lbf thrust hybrid motor with HTPB and GOX, a forward chamber for precombustion, and an aft mixing chamber provided combustion stability. Fuel grain fins in the precombustion chamber increase amount of fuel surface area to provide a sufficient level of preheating to the oxidizer. The fins are designed to overlap with the main ports to provide flame stabilization. These modifications successfully provided stable combustion throughout the duration of the tests conducted [8].

Another common problem in hybrid rocket development is the lack of tools to model and predict combustion instability when designing or scaling a hybrid motor [1]. Altman and Karabeyoglu note that in AMROC's motor series motors with approximately the same O/F ratio displayed an inversely proportional relationship between instability frequency and L*. It was observed from the AMROC data that in a boundary-layer thermal lag coupled system commonly found in hybrid motors, an increase in chamber pressure or decrease in port mass flux decreases the instability frequency [32].

Karabeyoglu et. al. suggests that the low frequency oscillation in hybrids is due to coupling of thermal lag, combustion, and gasdynamic systems. A universal scaling law was suggested as Equation (A.1) but does not account for amplitude of oscillations [33]. This equation states that the instabillity frequency, f, is a function of the oxidizer to fuel ratio O/F, the oxidizer flux, G_{ox}, the gas constant R, the average

combustion temperature T_{av}, the chamber length L, and the chamber pressure P.

$$f = 0.2341(2 + \frac{1}{O/F})\frac{G_{ox}RT_{av}}{LP} \tag{A.1}$$

APPENDIX B

THERMOCHEMICAL ANALYSIS RESULTS

Table B.1: Chracteristic velocity as a function of chamber pressure and gas-to-solid ratio (GSR), 0-2.5 GSR.

	Chamber Pressure (psi)							
GSR	1	100	500	1000	1500	2000	2500	3000
0	3182	3251	3290	3305	3313	3318	3322	3324
0.1	3600	3615	3645	3661	3671	3678	3683	3687
0.2	3957	3956	3968	3978	3985	3991	3996	4000
0.3	4178	4264	4264	4268	4272	4275	4278	4281
0.4	4299	4528	4534	4533	4534	4535	4537	4538
0.5	4543	4718	4766	4772	4773	4773	4773	4774
0.6	4978	5007	5007	5006	5006	5006	5006	5006
0.7	5105	5247	5266	5271	5272	5274	5274	5275
0.8	5165	5388	5433	5446	5452	5456	5459	5461
0.9	5174	5452	5524	5549	5562	5570	5576	5581
1	5154	5463	5557	5593	5612	5625	5635	5642
1.1	5122	5445	5552	5595	5619	5635	5648	5658
1.2	5085	5415	5527	5574	5600	5619	5633	5644
1.3	5048	5379	5494	5542	5570	5589	5604	5616
1.4	5011	5341	5456	5505	5534	5554	5569	5581
1.5	4975	5302	5418	5467	5496	5515	5531	5543
1.6	4940	5265	5380	5429	5457	5477	5492	5505
1.7	4907	5229	5343	5391	5419	5439	5454	5466
1.8	4875	5194	5306	5354	5382	5401	5416	5428
1.9	4845	5160	5271	5318	5345	5365	5379	5391
2	4816	5128	5237	5283	5310	5329	5344	5355
2.1	4789	5096	5204	5250	5276	5295	5309	5320
2.2	4763	5066	5172	5217	5243	5261	5275	5287
2.3	4737	5037	5142	5186	5211	5229	5243	5254
2.4	4713	5009	5112	5155	5180	5198	5211	5222
2.5	4690	4983	5084	5126	5150	5167	5180	5191

Table B.2: Chracteristic velocity as a function of chamber pressure and gas-to-solid ratio (GSR), 2.6-5 GSR.

	Chamber Pressure (psi)							
GSR	1	100	500	1000	1500	2000	2500	3000
2.6	4668	4956	5056	5097	5121	5138	5150	5161
2.7	4646	4931	5029	5069	5093	5109	5121	5131
2.8	4626	4907	5002	5042	5065	5081	5093	5103
2.9	4606	4883	4977	5016	5038	5053	5065	5075
3	4587	4860	4952	4990	5012	5026	5038	5047
3.1	4568	4838	4928	4965	4986	5000	5011	5020
3.2	4550	4816	4904	4940	4960	4974	4985	4994
3.3	4533	4794	4881	4916	4936	4949	4960	4968
3.4	4516	4774	4858	4892	4911	4924	4934	4942
3.5	4499	4753	4835	4869	4887	4900	4910	4917
3.6	4483	4733	4813	4846	4863	4876	4885	4893
3.7	4467	4713	4792	4823	4840	4852	4861	4868
3.8	4452	4694	4770	4800	4817	4829	4837	4844
3.9	4437	4675	4749	4778	4794	4805	4814	4820
4	4423	4656	4728	4757	4772	4783	4790	4797
4.1	4408	4638	4708	4735	4750	4760	4767	4773
4.2	4394	4620	4688	4714	4728	4737	4745	4750
4.3	4381	4602	4667	4692	4706	4715	4722	4727
4.4	4367	4584	4647	4671	4684	4693	4699	4705
4.5	4354	4566	4628	4651	4663	4671	4677	4682
4.6	4341	4549	4608	4630	4642	4649	4655	4660
4.7	4328	4532	4588	4609	4620	4628	4633	4637
4.8	4316	4515	4569	4589	4599	4606	4611	4615
4.9	4303	4497	4550	4569	4578	4585	4590	4593
5	4291	4481	4531	4548	4558	4564	4568	4572

Table B.3: Molecular weight as a function of chamber pressure and gas-to-solid ratio (GSR), 0-2.5 GSR.

	Chamber Pressure (psi)							
GSR	1	100	500	1000	1500	2000	2500	3000
0.0	13.3951	13.6640	14.0642	14.3136	14.4806	14.6078	14.7112	14.7983
0.1	14.7365	14.8132	15.0395	15.2240	15.3613	15.4721	15.5658	15.6471
0.2	16.1079	16.1051	16.2106	16.3226	16.4178	16.5009	16.5750	16.6421
0.3	17.4325	17.4612	17.5012	17.5626	17.6215	17.6769	17.7290	17.7781
0.4	18.7232	18.8257	18.8587	18.8943	18.9303	18.9661	19.0012	19.0355
0.5	20.0151	20.1646	20.2259	20.2651	20.2970	20.3262	20.3538	20.3802
0.6	21.0181	21.3259	21.3765	21.3910	21.3982	21.4030	21.4067	21.4099
0.7	21.8358	22.4351	22.5737	22.6191	22.6417	22.6562	22.6665	22.6744
0.8	22.5373	23.3954	23.6468	23.7379	23.7859	23.8174	23.8404	23.8583
0.9	23.1443	24.2056	24.5715	24.7166	24.7964	24.8504	24.8907	24.9226
1.0	23.6794	24.8819	25.3420	25.5373	25.6490	25.7266	25.7858	25.8333
1.1	24.1609	25.4567	25.9829	26.2161	26.3531	26.4503	26.5254	26.5865
1.2	24.6007	25.9585	26.5287	26.7876	26.9421	27.0530	27.1395	27.2105
1.3	25.0065	26.4062	27.0053	27.2812	27.4474	27.5673	27.6615	27.7391
1.4	25.3833	26.8117	27.4300	27.7170	27.8908	28.0167	28.1158	28.1977
1.5	25.7349	27.1829	27.8137	28.1079	28.2865	28.4162	28.5185	28.6032
1.6	26.0641	27.5252	28.1639	28.4625	28.6441	28.7761	28.8803	28.9666
1.7	26.3734	27.8426	28.4858	28.7868	28.9700	29.1032	29.2084	29.2955
1.8	26.6646	28.1381	28.7832	29.0852	29.2689	29.4025	29.5080	29.5954
1.9	26.9393	28.4141	29.0591	29.3608	29.5443	29.6777	29.7830	29.8703
2.0	27.1989	28.6726	29.3158	29.6164	29.7990	29.9317	30.0365	30.1232
2.1	27.4447	28.9152	29.5554	29.8540	30.0353	30.1669	30.2707	30.3566
2.2	27.6776	29.1433	29.7792	30.0753	30.2548	30.3850	30.4876	30.5725
2.3	27.8987	29.3581	29.9889	30.2818	30.4592	30.5877	30.6889	30.7726
2.4	28.1088	29.5606	30.1854	30.4748	30.6498	30.7764	30.8760	30.9583
2.5	28.3086	29.7517	30.3698	30.6554	30.8276	30.9522	31.0500	31.1308

Table B.4: Molecular weight as a function of chamber pressure and gas-to-solid ratio (GSR), 2.6-5 GSR.

	Chamber Pressure (psi)							
GSR	1	100	500	1000	1500	2000	2500	3000
2.6	28.4989	29.9322	30.5431	30.8244	30.9938	31.1161	31.2120	31.2912
2.7	28.6802	30.1030	30.7060	30.9828	31.1491	31.2690	31.3630	31.4404
2.8	28.8531	30.2645	30.8593	31.1312	31.2943	31.4117	31.5036	31.5792
2.9	29.0183	30.4175	31.0035	31.2705	31.4302	31.5449	31.6347	31.7085
3.0	29.1760	30.5624	31.1393	31.4011	31.5573	31.6694	31.7569	31.8287
3.1	29.3268	30.6998	31.2672	31.5236	31.6762	31.7855	31.8708	31.9407
3.2	29.4710	30.8301	31.3877	31.6385	31.7875	31.8940	31.9769	32.0448
3.3	29.6091	30.9536	31.5012	31.7464	31.8916	31.9952	32.0757	32.1416
3.4	29.7413	31.0709	31.6081	31.8475	31.9889	32.0896	32.1677	32.2315
3.5	29.8680	31.1821	31.7088	31.9424	32.0799	32.1776	32.2533	32.3151
3.6	29.9895	31.2877	31.8037	32.0313	32.1649	32.2596	32.3329	32.3926
3.7	30.1060	31.3879	31.8930	32.1145	32.2442	32.3359	32.4067	32.4644
3.8	30.2178	31.4831	31.9770	32.1925	32.3182	32.4069	32.4753	32.5308
3.9	30.3251	31.5733	32.0561	32.2654	32.3871	32.4728	32.5388	32.5923
4.0	30.4282	31.6590	32.1304	32.3336	32.4513	32.5340	32.5975	32.6490
4.1	30.5272	31.7404	32.2002	32.3973	32.5110	32.5907	32.6518	32.7012
4.2	30.6224	31.8175	32.2658	32.4567	32.5664	32.6431	32.7019	32.7492
4.3	30.7138	31.8907	32.3273	32.5120	32.6178	32.6916	32.7479	32.7933
4.4	30.8017	31.9601	32.3850	32.5635	32.6653	32.7362	32.7902	32.8336
4.5	30.8863	32.0258	32.4389	32.6113	32.7093	32.7772	32.8289	32.8704
4.6	30.9676	32.0881	32.4894	32.6557	32.7498	32.8149	32.8643	32.9039
4.7	31.0459	32.1471	32.5366	32.6967	32.7870	32.8493	32.8965	32.9343
4.8	31.1212	32.2028	32.5806	32.7347	32.8212	32.8808	32.9258	32.9618
4.9	31.1936	32.2556	32.6215	32.7697	32.8525	32.9093	32.9522	32.9864
5.0	31.2634	32.3054	32.6596	32.8018	32.8811	32.9352	32.9760	33.0085

Table B.5: Combustion temperature as a function of chamber pressure and gas-to-solid ratio (GSR), 0-2.5 GSR.

	Chamber Pressure (psi)							
GSR	1	100	500	1000	1500	2000	2500	3000
0	2164.51	2301.15	2452.44	2533.82	2585.18	2623.09	2653.24	2678.32
0.1	2643.71	2686.81	2767.56	2827.97	2870.67	2904.06	2931.63	2955.16
0.2	2923.92	3106.00	3141.87	3174.05	3200.42	3222.96	3242.73	3260.37
0.3	3032.68	3453.28	3514.38	3537.09	3553.54	3567.62	3580.28	3591.89
0.4	3388.23	3658.52	3810.79	3856.15	3878.66	3893.93	3905.87	3915.94
0.5	3708.28	3810.23	4001.83	4084.60	4127.21	4154.70	4174.58	4188.60
0.6	4329.70	4663.75	4718.83	4734.20	4741.35	4745.75	4748.85	4751.22
0.7	4675.21	5259.33	5393.97	5437.53	5459.13	5472.81	5482.51	5489.87
0.8	4876.90	5664.78	5894.30	5977.05	6020.32	6048.65	6069.26	6085.22
0.9	4985.42	5914.63	6231.12	6355.91	6424.27	6470.38	6504.69	6531.72
1	5041.05	6053.46	6432.31	6591.64	6682.29	6745.06	6792.71	6830.88
1.1	5068.82	6126.03	6542.21	6724.04	6830.03	6904.75	6962.28	7008.94
1.2	5081.30	6161.34	6598.04	6792.77	6907.84	6989.78	7053.40	7105.37
1.3	5084.81	6175.16	6622.39	6824.02	6944.03	7029.94	7096.96	7151.92
1.4	5082.73	6175.95	6627.80	6832.72	6955.14	7043.05	7111.77	7168.25
1.5	5077.00	6168.47	6621.30	6827.27	6950.57	7039.23	7108.63	7165.73
1.6	5068.81	6155.50	6606.97	6812.59	6935.78	7024.42	7093.84	7150.98
1.7	5058.91	6138.79	6587.34	6791.65	6914.08	7002.19	7071.19	7128.00
1.8	5047.79	6119.45	6564.00	6766.37	6887.59	6974.80	7043.10	7099.31
1.9	5035.81	6098.23	6538.00	6737.97	6857.67	6943.74	7011.13	7066.57
2	5023.19	6075.64	6510.08	6707.30	6825.25	6910.01	6976.33	7030.87
2.1	5010.10	6052.05	6480.73	6674.96	6790.99	6874.31	6939.45	6993.00
2.2	4996.68	6027.71	6450.30	6641.36	6755.35	6837.12	6901.01	6953.49
2.3	4983.01	6002.80	6419.07	6606.81	6718.66	6798.81	6861.38	6912.74
2.4	4969.16	5977.47	6387.22	6571.53	6681.16	6759.63	6820.84	6871.04
2.5	4955.18	5951.82	6354.90	6535.68	6643.04	6719.79	6779.60	6828.61

Table B.6: Combustion temperature as a function of chamber pressure and gas-to-solid ratio (GSR), 2.6-5 GSR.

	Chamber Pressure (psi)							
GSR	1	100	500	1000	1500	2000	2500	3000
2.6	4941.10	5925.93	6322.20	6499.40	6604.43	6679.43	6737.81	6785.61
2.7	4926.97	5899.85	6289.22	6462.77	6565.44	6638.66	6695.59	6742.17
2.8	4912.79	5873.63	6256.01	6425.87	6526.16	6597.57	6653.04	6698.37
2.9	4898.59	5847.29	6222.62	6388.75	6486.63	6556.23	6610.22	6654.31
3	4884.38	5820.87	6189.08	6351.46	6446.92	6514.69	6567.20	6610.03
3.1	4870.17	5794.38	6155.43	6314.03	6407.05	6472.98	6524.01	6565.58
3.2	4855.96	5767.83	6121.67	6276.48	6367.06	6431.15	6480.69	6521.00
3.3	4841.76	5741.23	6087.84	6238.84	6326.97	6389.22	6437.26	6476.32
3.4	4827.57	5714.60	6053.93	6201.11	6286.80	6347.21	6393.76	6431.56
3.5	4813.39	5687.93	6019.96	6163.32	6246.55	6305.13	6350.20	6386.75
3.6	4799.23	5661.22	5985.93	6125.47	6206.26	6263.00	6306.59	6341.90
3.7	4785.07	5634.48	5951.85	6087.56	6165.91	6220.83	6262.95	6297.03
3.8	4770.93	5607.70	5917.72	6049.61	6125.53	6178.63	6219.30	6252.15
3.9	4756.81	5580.88	5883.54	6011.62	6085.11	6136.41	6175.63	6207.27
4	4742.69	5554.03	5849.31	5973.59	6044.68	6094.19	6131.98	6162.41
4.1	4728.57	5527.13	5815.04	5935.53	6004.22	6051.96	6088.33	6117.58
4.2	4714.46	5500.19	5780.72	5897.44	5963.76	6009.74	6044.71	6072.79
4.3	4700.35	5473.20	5746.36	5859.33	5923.29	5967.53	6001.12	6028.05
4.4	4686.24	5446.17	5711.96	5821.19	5882.83	5925.36	5957.58	5983.38
4.5	4672.13	5419.07	5677.52	5783.05	5842.38	5883.21	5914.09	5938.78
4.6	4658.01	5391.93	5643.03	5744.89	5801.94	5841.11	5870.68	5894.27
4.7	4643.88	5364.72	5608.51	5706.73	5761.54	5799.06	5827.34	5849.87
4.8	4629.73	5337.46	5573.95	5668.57	5721.16	5757.08	5784.09	5805.58
4.9	4615.57	5310.12	5539.37	5630.42	5680.84	5715.18	5740.95	5761.42
5	4601.38	5282.73	5504.75	5592.29	5640.56	5673.36	5697.92	5717.40

Table B.7: Ratio of specific heats as a function of chamber pressure and gas-to-solid ratio (GSR), 0-2.5 GSR.

	Chamber Pressure (psi)							
GSR	1	100	500	1000	1500	2000	2500	3000
0	1.34743	1.32532	1.29810	1.28316	1.27383	1.26702	1.26168	1.25729
0.1	1.32867	1.32377	1.31082	1.30101	1.29408	1.28868	1.28426	1.28050
0.2	1.31723	1.31468	1.30990	1.30504	1.30103	1.29761	1.29461	1.29195
0.3	1.31209	1.30671	1.30469	1.30248	1.30044	1.29855	1.29681	1.29518
0.4	1.30593	1.30219	1.29974	1.29837	1.29723	1.29616	1.29516	1.29420
0.5	1.30114	1.29962	1.29673	1.29520	1.29417	1.29334	1.29260	1.29193
0.6	1.29421	1.28747	1.28637	1.28605	1.28589	1.28579	1.28571	1.28564
0.7	1.28189	1.26994	1.26737	1.26654	1.26612	1.26586	1.26567	1.26553
0.8	1.27315	1.25732	1.25314	1.25167	1.25091	1.25041	1.25005	1.24976
0.9	1.26713	1.24850	1.24279	1.24063	1.23946	1.23868	1.23810	1.23764
1	1.26281	1.24247	1.23560	1.23282	1.23126	1.23020	1.22939	1.22875
1.1	1.25950	1.23823	1.23063	1.22743	1.22559	1.22431	1.22332	1.22253
1.2	1.25682	1.23509	1.22707	1.22362	1.22160	1.22018	1.21909	1.21820
1.3	1.25458	1.23264	1.22440	1.22081	1.21870	1.21720	1.21604	1.21509
1.4	1.25265	1.23067	1.22232	1.21866	1.21649	1.21495	1.21376	1.21277
1.5	1.25096	1.22903	1.22065	1.21696	1.21477	1.21321	1.21200	1.21100
1.6	1.24947	1.22764	1.21928	1.21558	1.21339	1.21183	1.21061	1.20961
1.7	1.24815	1.22646	1.21814	1.21445	1.21227	1.21072	1.20950	1.20850
1.8	1.24695	1.22543	1.21718	1.21352	1.21136	1.20981	1.20861	1.20762
1.9	1.24588	1.22454	1.21636	1.21274	1.21060	1.20907	1.20788	1.20690
2	1.24491	1.22376	1.21567	1.21210	1.20998	1.20847	1.20730	1.20633
2.1	1.24402	1.22308	1.21509	1.21156	1.20947	1.20799	1.20683	1.20588
2.2	1.24322	1.22248	1.21459	1.21111	1.20906	1.20760	1.20646	1.20553
2.3	1.24249	1.22196	1.21417	1.21075	1.20873	1.20729	1.20618	1.20526
2.4	1.24182	1.22151	1.21383	1.21046	1.20848	1.20707	1.20597	1.20508
2.5	1.24121	1.22111	1.21354	1.21023	1.20829	1.20690	1.20583	1.20495

Table B.8: Ratio of specific heats as a function of chamber pressure and gas-to-solid ratio (GSR), 2.6-5 GSR.

	Chamber Pressure (psi)							
GSR	1	100	500	1000	1500	2000	2500	3000
2.6	1.24065	1.22077	1.21332	1.21006	1.20816	1.20680	1.20575	1.20489
2.7	1.24014	1.22047	1.21314	1.20995	1.20808	1.20675	1.20572	1.20489
2.8	1.23967	1.22023	1.21301	1.20988	1.20804	1.20675	1.20574	1.20493
2.9	1.23925	1.22002	1.21292	1.20985	1.20806	1.20679	1.20581	1.20501
3	1.23886	1.21985	1.21287	1.20986	1.20811	1.20687	1.20592	1.20514
3.1	1.23850	1.21972	1.21286	1.20991	1.20820	1.20699	1.20606	1.20530
3.2	1.23818	1.21962	1.21288	1.20999	1.20832	1.20714	1.20624	1.20550
3.3	1.23789	1.21954	1.21293	1.21011	1.20848	1.20733	1.20645	1.20573
3.4	1.23762	1.21950	1.21301	1.21025	1.20866	1.20755	1.20669	1.20600
3.5	1.23739	1.21949	1.21312	1.21042	1.20888	1.20779	1.20696	1.20628
3.6	1.23717	1.21950	1.21325	1.21062	1.20911	1.20806	1.20725	1.20660
3.7	1.23698	1.21953	1.21341	1.21085	1.20938	1.20835	1.20757	1.20694
3.8	1.23681	1.21959	1.21359	1.21109	1.20967	1.20867	1.20791	1.20730
3.9	1.23666	1.21966	1.21380	1.21136	1.20998	1.20901	1.20828	1.20769
4	1.23653	1.21976	1.21402	1.21165	1.21031	1.20937	1.20866	1.20809
4.1	1.23641	1.21988	1.21427	1.21196	1.21066	1.20975	1.20907	1.20852
4.2	1.23632	1.22001	1.21453	1.21229	1.21103	1.21015	1.20949	1.20896
4.3	1.23624	1.22017	1.21481	1.21264	1.21141	1.21057	1.20993	1.20942
4.4	1.23617	1.22034	1.21511	1.21300	1.21182	1.21101	1.21039	1.20990
4.5	1.23612	1.22053	1.21543	1.21338	1.21224	1.21146	1.21086	1.21039
4.6	1.23609	1.22073	1.21576	1.21378	1.21267	1.21192	1.21135	1.21090
4.7	1.23607	1.22095	1.21611	1.21419	1.21313	1.21240	1.21185	1.21142
4.8	1.23606	1.22118	1.21647	1.21462	1.21359	1.21289	1.21237	1.21195
4.9	1.23606	1.22142	1.21685	1.21505	1.21407	1.21340	1.21290	1.21250
5	1.23607	1.22168	1.21724	1.21551	1.21456	1.21392	1.21344	1.21306

APPENDIX C

TESTING MEASUREMENTS AND PRESSURE TRACES

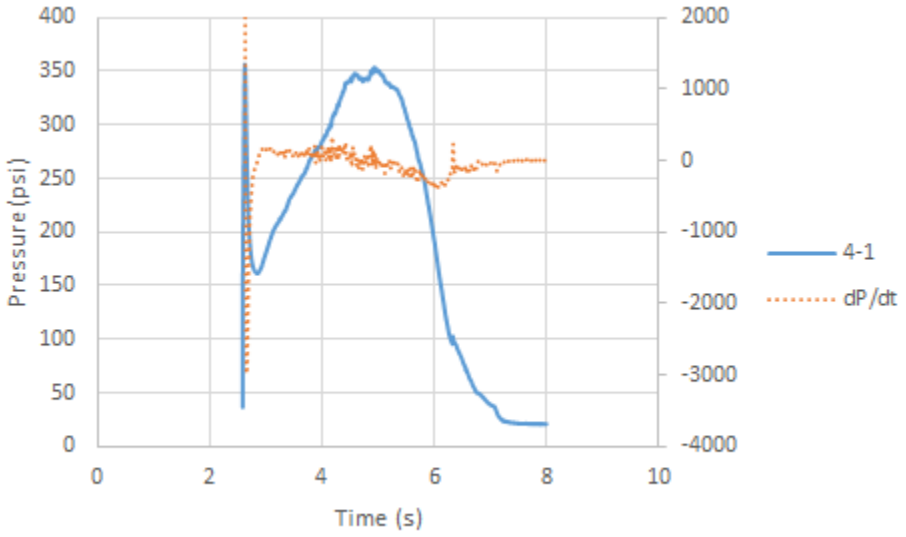

Figure C.1: Pressure trace and dP/dt for test 4-1, 0.2969" throat diameter, no GOX flow.

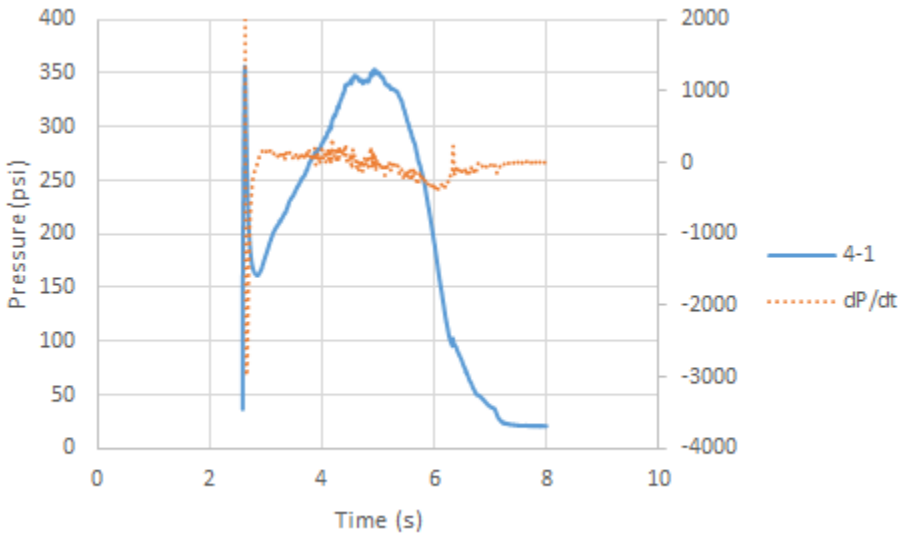

Figure C.2: Pressure trace and dP/dt for test 4-2, 0.2610" throat diameter, no GOX flow.

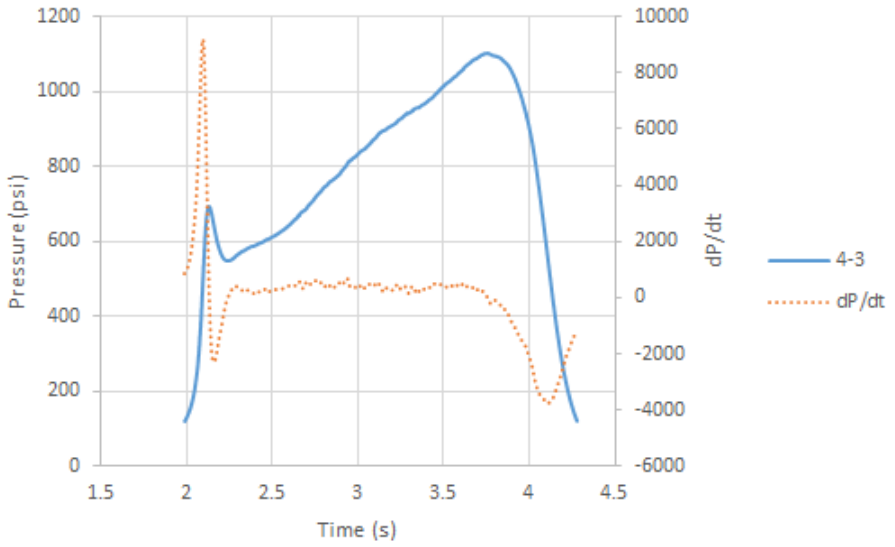

Figure C.3: Pressure trace and dP/dt for test 4-3, 0.2380" throat diameter, no GOX flow.

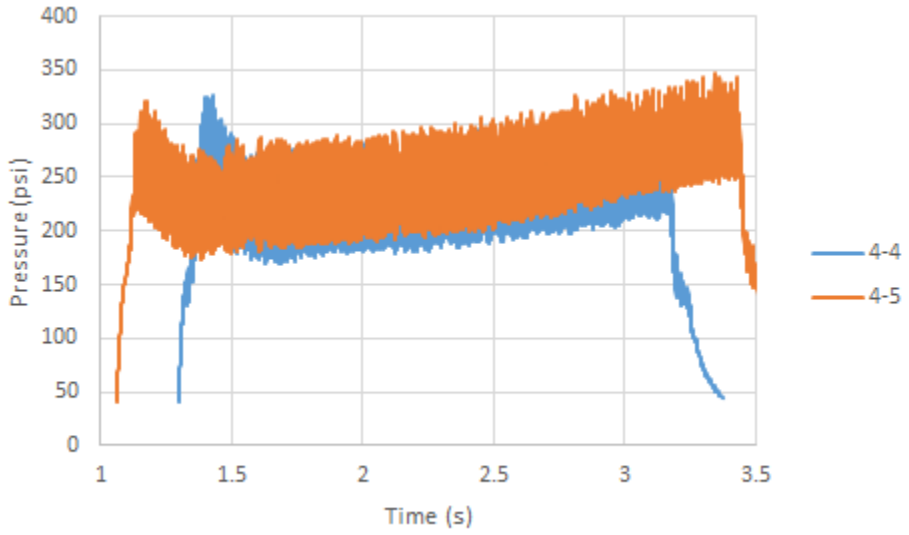

Figure C.4: Pressure trace for tests 4-4 and 4-5, 0.4375" throat diameter, 0.1 lbm/s GOX flow.

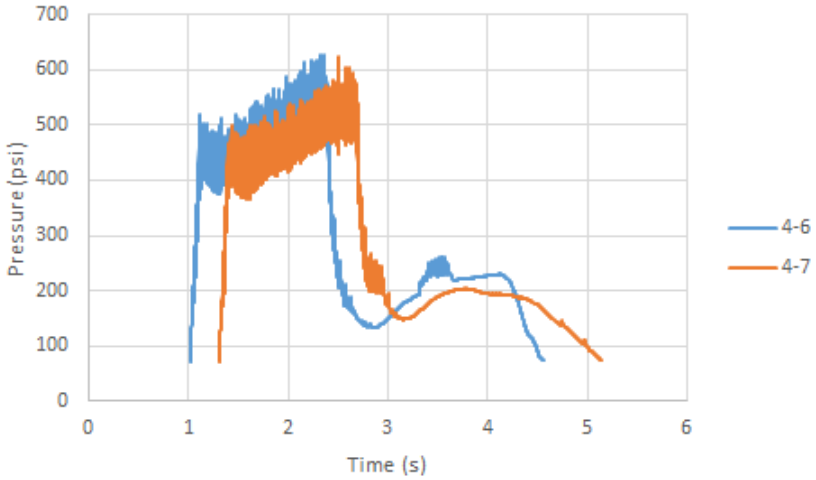

Figure C.5: Pressure trace for tests 4-6 and 4-7, 0.3750" throat diameter, 0.1 lbm/s GOX flow.

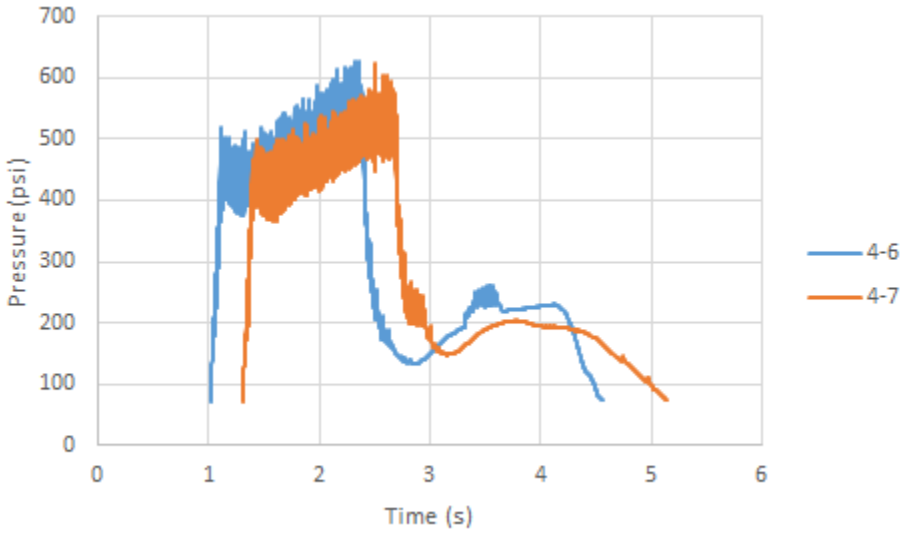

Figure C.6: Pressure trace for tests 4-8 and 4-9, 0.3750" throat diameter, 0.1 lbm/s GOX flow.

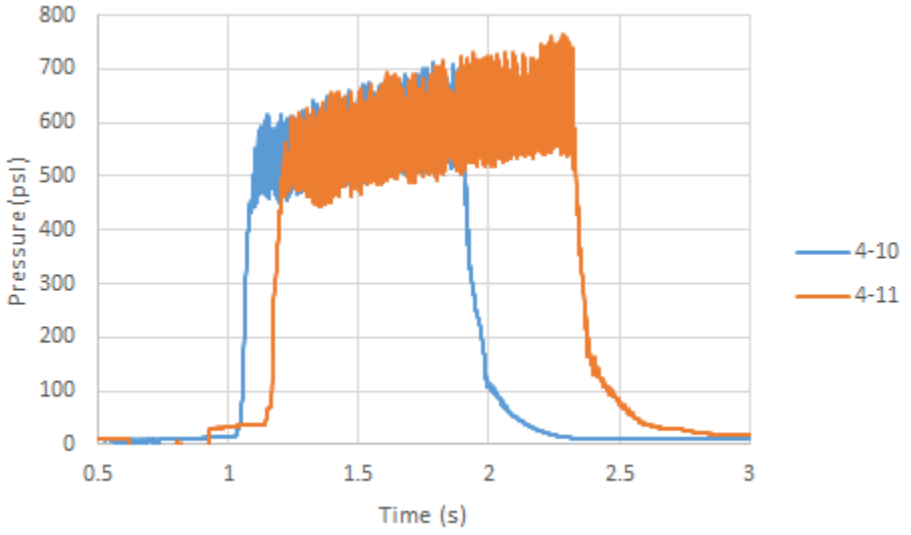

Figure C.7: Pressure trace for tests 4-10 and 4-11, 0.4375" throat diameter, 0.3 lbm/s GOX flow.

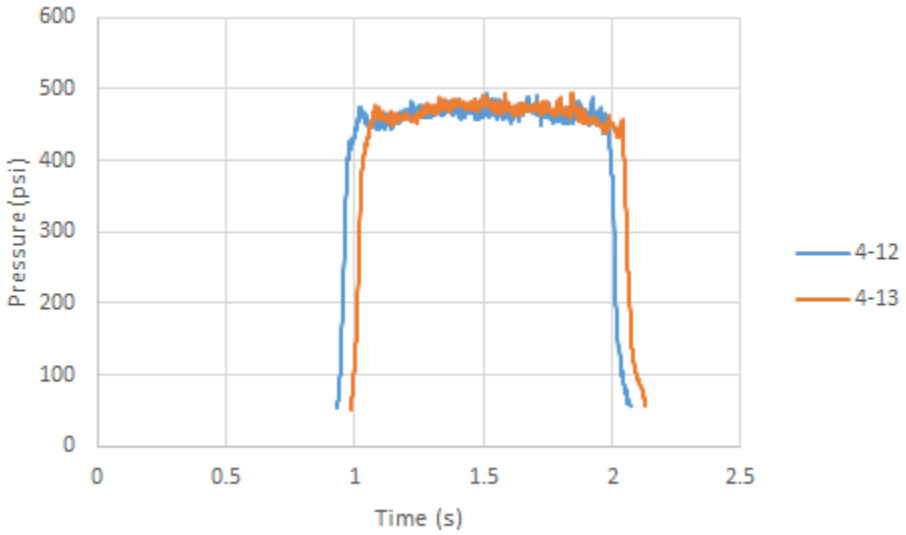

Figure C.8: Pressure trace for tests 4-12 and 4-13, 0.6000" throat diameter, 0.6 lbm/s GOX flow.

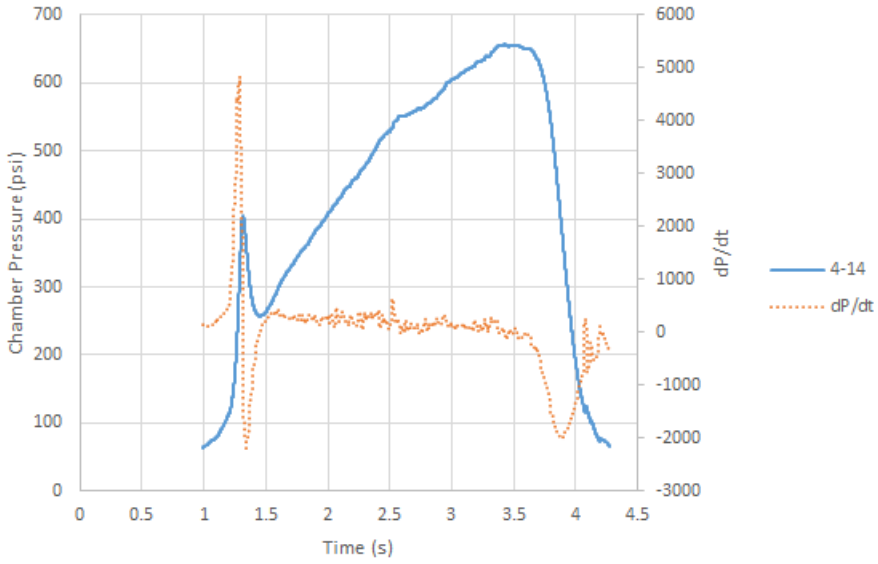

Figure C.9: Pressure trace and dP/dt for test 4-14, 0.2610" throat diameter, no GOX flow.

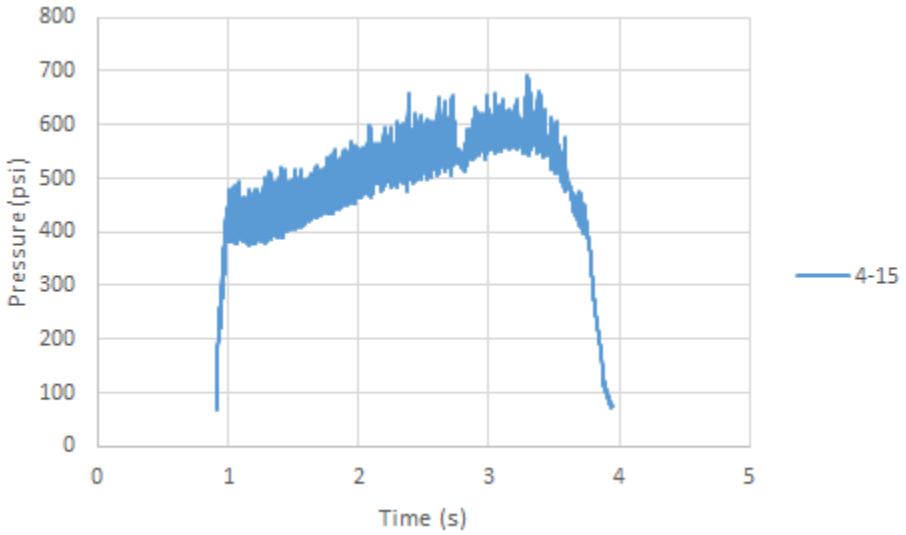

Figure C.10: Pressure trace for test 4-15, 0.3750" throat diameter, 0.1 lbm/s GOX flow.

Table C.1: Measured data for tests 4-1, 4-2, and 4-3.

Test number		**4-1**	**4-2**	**4-3**
Grain identification number		1	5	7
Pre-test web	1	0.524	0.426	0.49
thickness (head end)	2	0.4675	0.425	0.409
	3	0.2575	0.437	0.413
	4	0.391	0.435	0.4805
	Average	0.41	0.43075	0.448125
Pre-test web	1	0.425	0.374	0.4905
thickness (nozzle end)	2	0.4445	0.477	0.4345
	3	0.4285	0.543	0.444
	4	0.4285	0.436	0.4345
	Average	0.431625	0.4575	0.450875
Post-test web	1	0	0	0
thickness (head end)	2	0	0	0
	3	0	0	0
	4	0	0	0
	Average	0	0	0
Post-test web	1	0	0	0
thickness (nozzle end)	2	0	0	0
	3	0	0	0
	4	0	0	0
	Average	0	0	0
Pre-test grain length		11.5	11.5	11.5
Post-test grain length		0	0	0
Pre-test grain mass		562	565	566
Post-test grain mass		114	114	109
Throat diameter		0.2969	0.261	0.238
Venturi diameter		0	0	0

Table C.2: Measured data for tests 4-4, 4-5, and 4-6.

Test number		**4-4**	**4-5**	**4-6**
Grain identification number		2	3	4
Pre-test web	1	0.446	0.4745	0.465
thickness (head end)	2	0.4455	0.4315	0.4885
	3	0.454	0.4155	0.416
	4	0.44	0.46	0.3985
	Average	0.446375	0.445375	0.442
Pre-test web	1	0.4485	0.4385	0.4455
thickness (nozzle end)	2	0.43	0.442	0.439
	3	0.4345	0.4425	0.4415
	4	0.441	0.438	0.451
	Average	0.4385	0.44025	0.44425
Post-test web	1	0.271	0.265	0
thickness (head end)	2	0.285	0.227	0
	3	0.304	0.177	0
	4	0.276	0.218	0
	Average	0.284	0.22175	0
Post-test web	1	0.2905	0.251	0
thickness (nozzle end)	2	0.2855	0.253	0
	3	0.294	0.2375	0
	4	0.2805	0.22	0
	Average	0.287625	0.240375	0
Pre-test grain length		11.5	11.5	11.5
Post-test grain length		11.03	10.94	0
Pre-test grain mass		569	563	562
Post-test grain mass		404	328	119
Throat diameter		0.4375	0.4375	0.375
Venturi diameter		0.08	0.08	0.08

Table C.3: Measured data for tests 4-7, 4-8, and 4-9.

Test number		**4-7**	**4-8**	**4-9**
Grain identification number		6	10	12
Pre-test web	1	0.4605	0.4505	0.4475
thickness (head end)	2	0.4125	0.439	0.453
	3	0.4215	0.443	0.459
	4	0.469	0.4405	0.429
	Average	0.440875	0.44325	0.447125
Pre-test web	1	0.4315	0.433	0.435
thickness (nozzle end)	2	0.428	0.4365	0.437
	3	0.4365	0.4745	0.4295
	4	0.437	0.4575	0.433
	Average	0.43325	0.450375	0.433625
Post-test web	1	0	0	0
thickness (head end)	2	0	0	0
	3	0	0	0
	4	0	0	0
	Average	0	0	0
Post-test web	1	0	0	0
thickness (nozzle end)	2	0	0	0
	3	0	0	0
	4	0	0	0
	Average	0	0	0
Pre-test grain length		11.5	11.5	11.5
Post-test grain length		0	0	0
Pre-test grain mass		558	565	564
Post-test grain mass		115	120	119
Throat diameter		0.375	0.375	0.375
Venturi diameter		0.08	0.08	0.08

Table C.4: Measured data for tests 4-10, 4-11, and 4-12.

Test number		**4-10**	**4-11**	**4-12**
Grain identification number		13	14	18
Pre-test web	1	0.428	0.4905	0.456
thickness (head end)	2	0.457	0.437	0.494
	3	0.4525	0.397	0.44
	4	0.428	0.446	0.3945
	Average	0.441375	0.442625	0.446125
Pre-test web	1	0.436	0.451	0.441
thickness (nozzle end)	2	0.4355	0.4495	0.444
	3	0.4345	0.432	0.436
	4	0.4365	0.432	0.442
	Average	0.435625	0.441125	0.44075
Post-test web	1	0.287	0.329	0.316
thickness (head end)	2	0.2945	0.284	0.3335
	3	0.315	0.2245	0.2735
	4	0.306	0.276	0.271
	Average	0.300625	0.278375	0.2985
Post-test web	1	0.3035	0.2755	0.256
thickness (nozzle end)	2	0.3005	0.272	0.25
	3	0.3115	0.257	0.251
	4	0.318	0.266	0.246
	Average	0.308375	0.267625	0.25075
Pre-test grain length		11.5	11.5	11.42
Post-test grain length		11.15	11.06	11.14
Pre-test grain mass		562	563	564
Post-test grain mass		425	371	393
Throat diameter		0.4375	0.4375	0.6
Venturi diameter		0.12	0.12	0.186

Table C.5: Measured data for tests 4-13, 4-14, and 4-15.

Test number		**4-13**	**4-14**	**4-15**
Grain identification number		25	26	23
Pre-test web	1	0.441	0.415	0.4085
thickness (head end)	2	0.4385	0.4725	0.4315
	3	0.4395	0.475	0.4815
	4	0.451	0.418	0.4525
	Average	0.4425	0.445125	0.4435
Pre-test web	1	0.441	0.434	0.4365
thickness (nozzle end)	2	0.4495	0.4455	0.4465
	3	0.4465	0.445	0.4475
	4	0.44	0.443	0.445
	Average	0.44425	0.441875	0.443875
Post-test web	1	0.287	0	0
thickness (head end)	2	0.2855	0	0
	3	0.299	0	0
	4	0.2945	0	0
	Average	0.2915	0	0
Post-test web	1	0.249	0	0
thickness (nozzle end)	2	0.2555	0	0
	3	0.2465	0	0
	4	0.2415	0	0
	Average	0.248125	0	0
Pre-test grain length		11.5	11.49	11.5
Post-test grain length		11.22	0	0
Pre-test grain mass		558	559	562
Post-test grain mass		384	107	107
Throat diameter		0.6	0.261	0.375
Venturi diameter		0.186	0	0.08

APPENDIX D

HARDWARE AND GRAIN SCHEMATICS

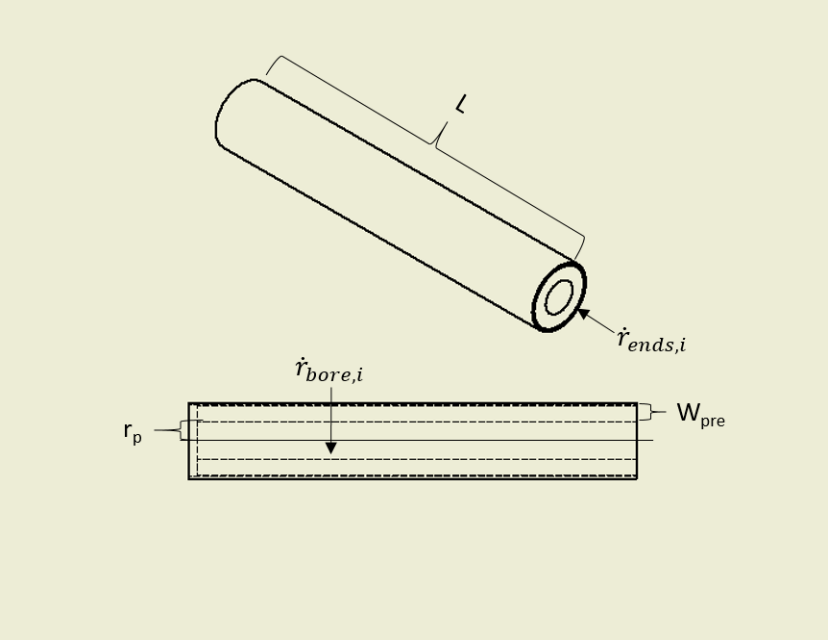

Figure D.1: Schematic of motor grain.

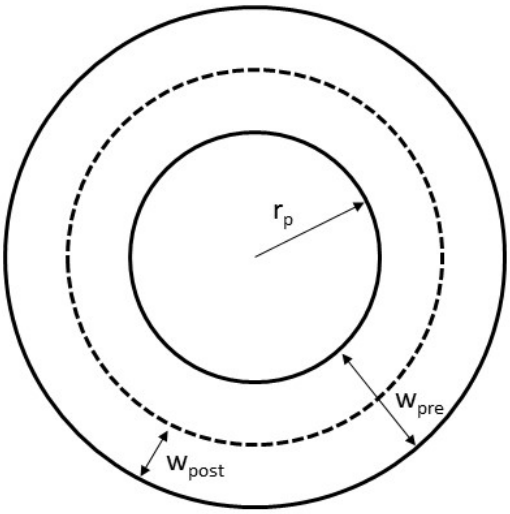

Figure D.2: End view schematic of motor grain.

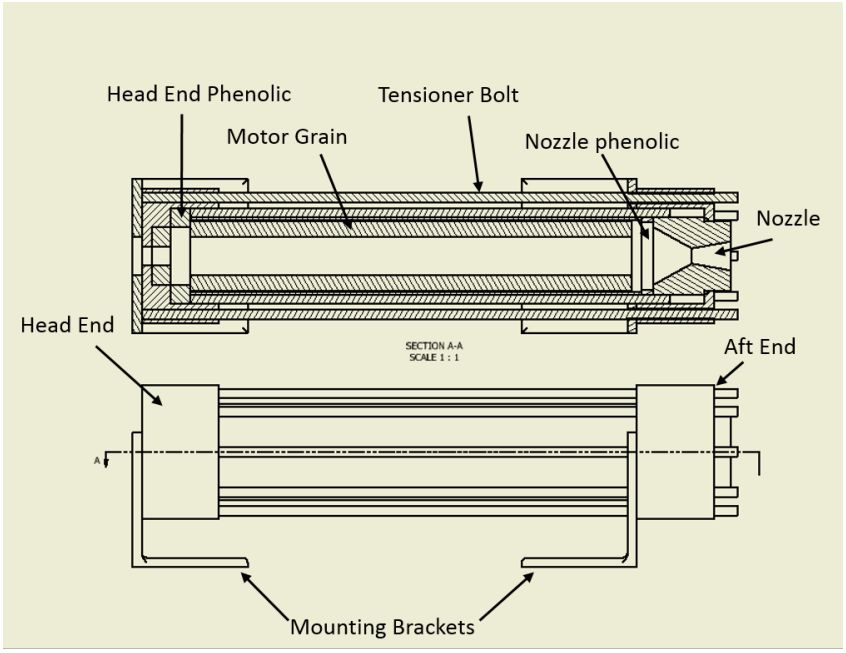

Figure D.3: Schematic of motor hardware.

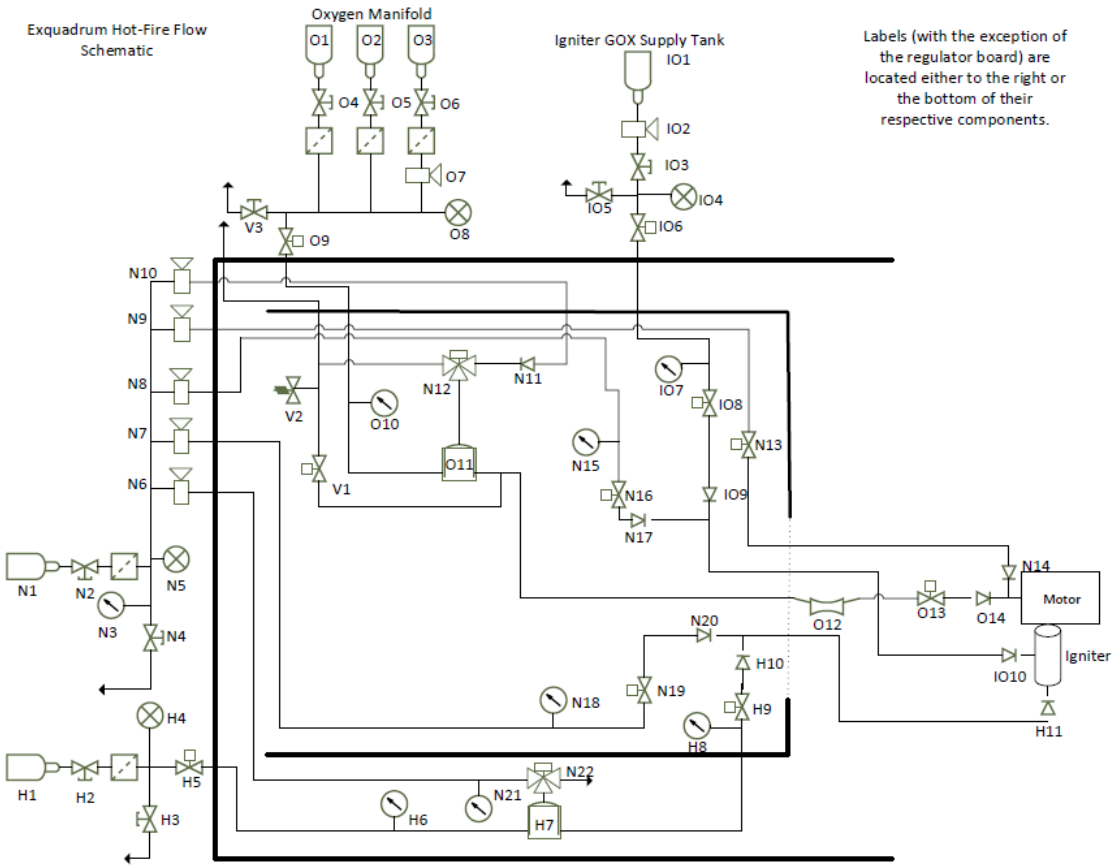

Figure D.4: Rocket test cell feed system schematic.

APPENDIX E

PREDICTED AND MEASURED PRESSURE TRACES

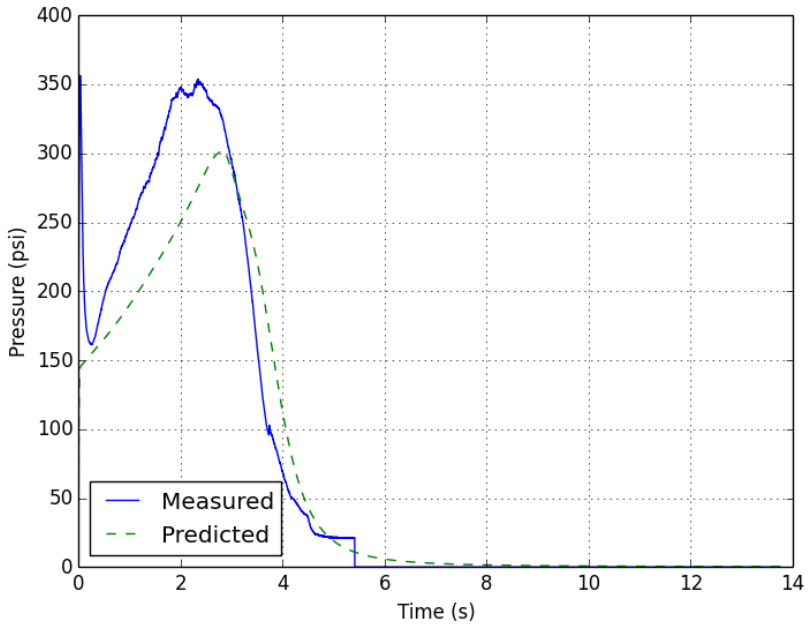

Figure E.1: Predicted and measured pressure traces for test 4-1.

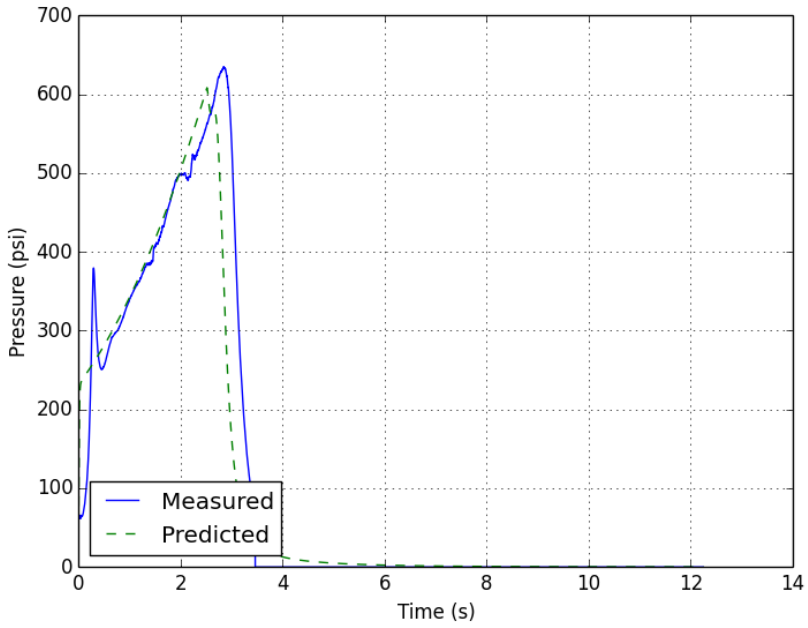

Figure E.2: Predicted and measured pressure traces for test 4-2.

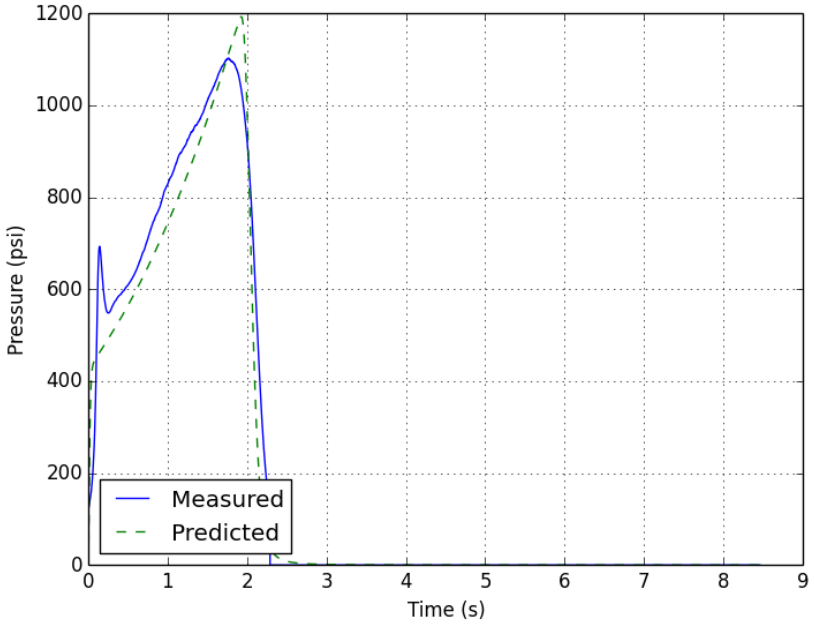

Figure E.3: Predicted and measured pressure traces for test 4-3.

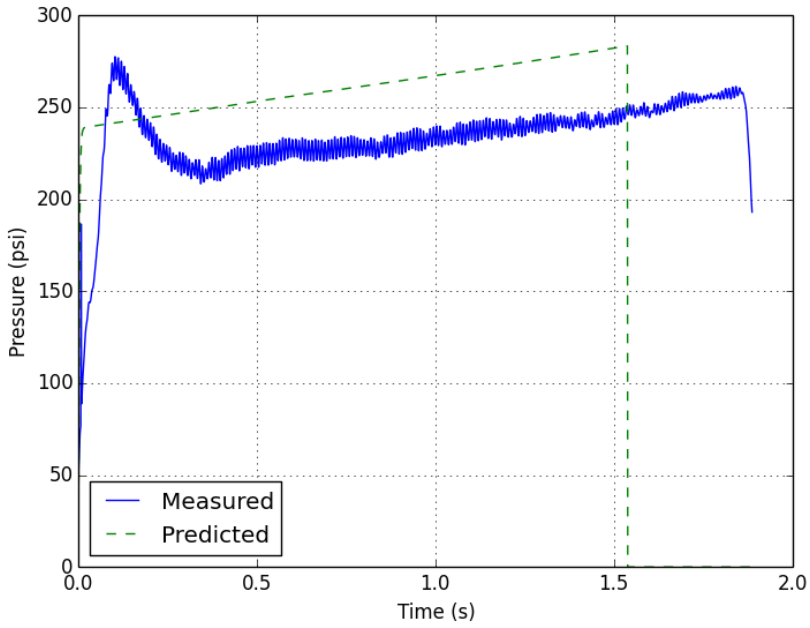

Figure E.4: Predicted and measured pressure traces for test 4-4.

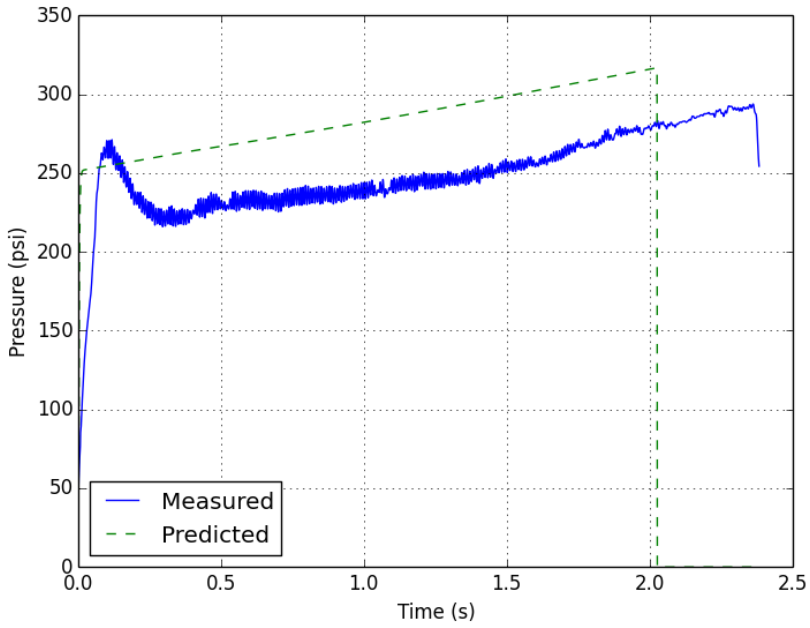

Figure E.5: Predicted and measured pressure traces for test 4-5.

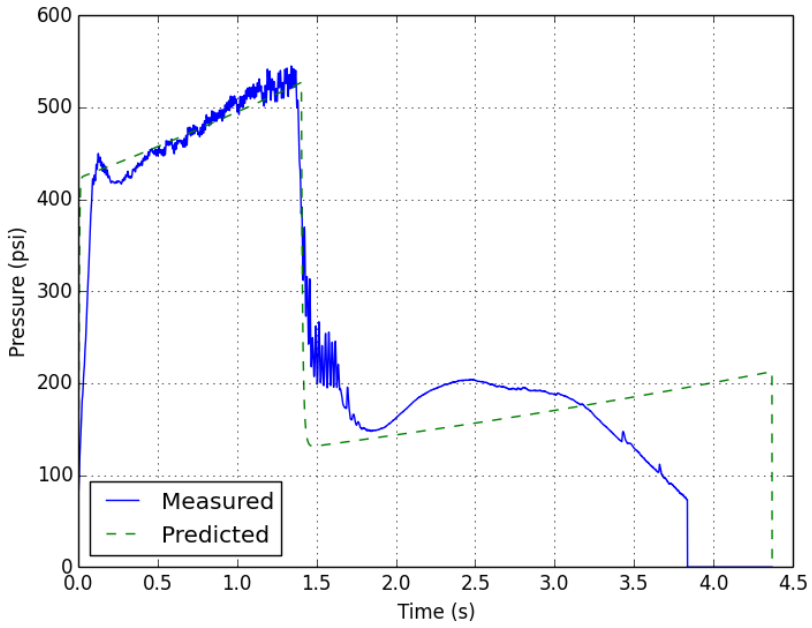

Figure E.6: Predicted and measured pressure traces for test 4-6.

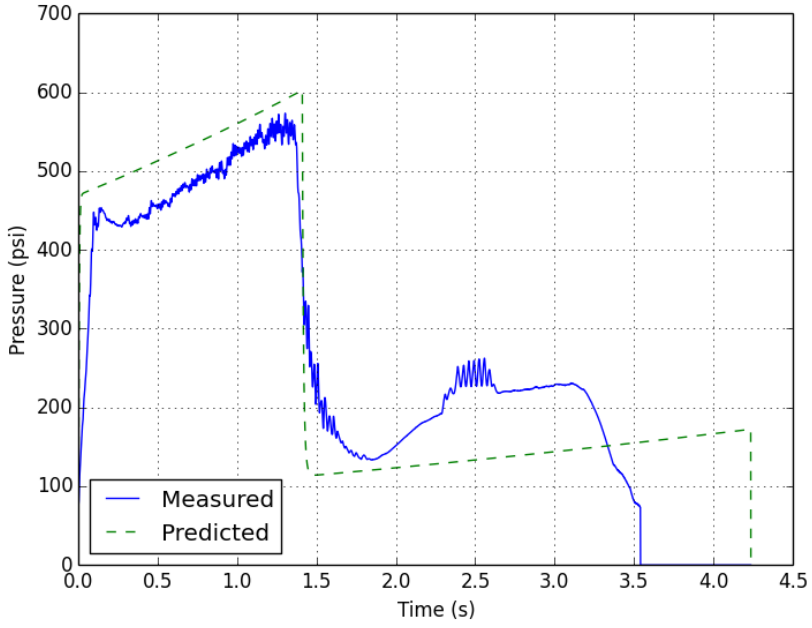

Figure E.7: Predicted and measured pressure traces for test 4-7.

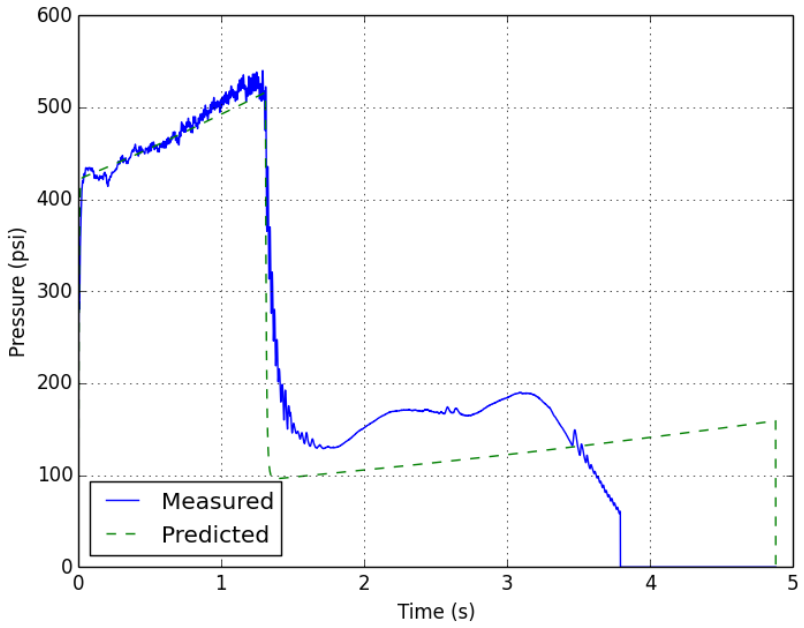

Figure E.8: Predicted and measured pressure traces for test 4-8.

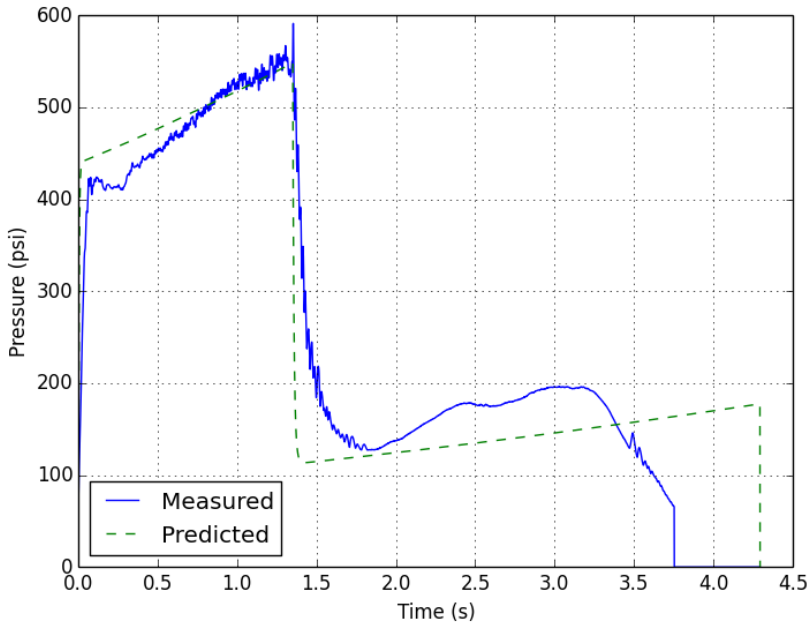

Figure E.9: Predicted and measured pressure traces for test 4-9.

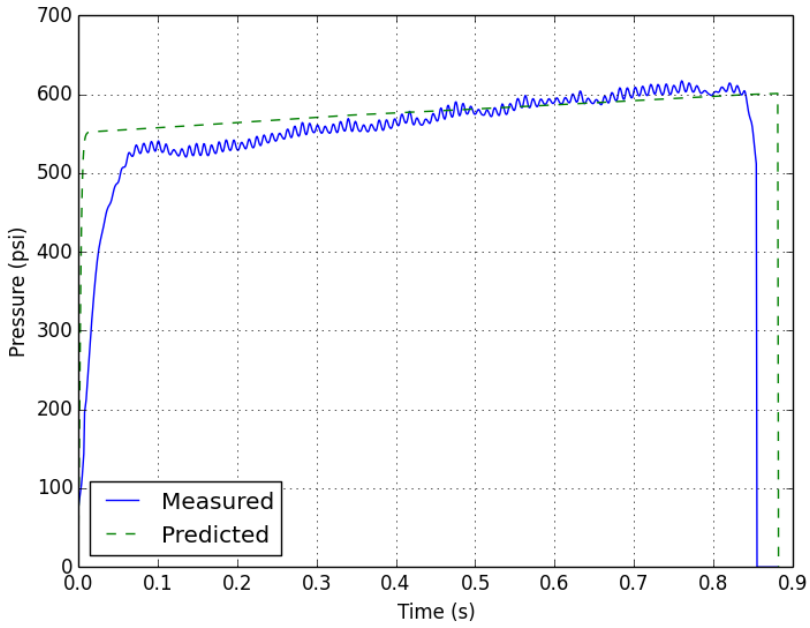

Figure E.10: Predicted and measured pressure traces for test 4-10.

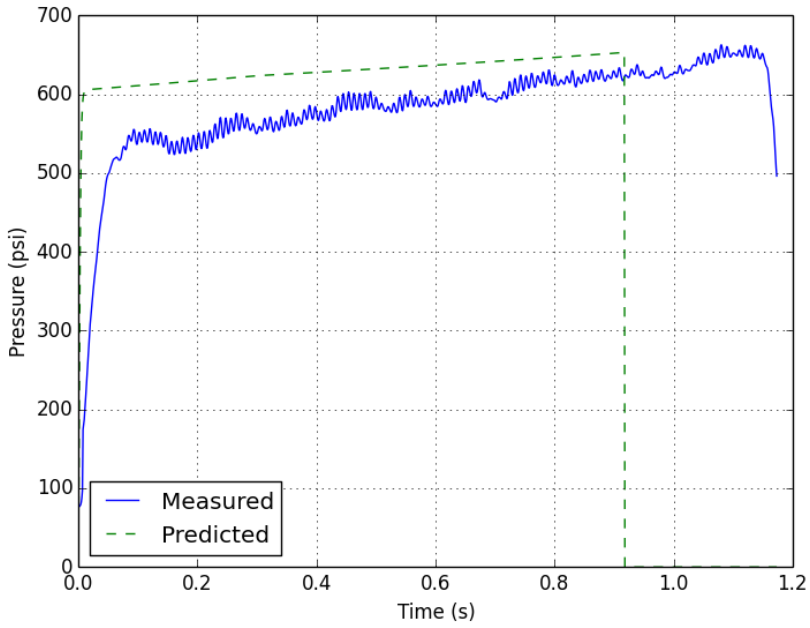

Figure E.11: Predicted and measured pressure traces for test 4-11.

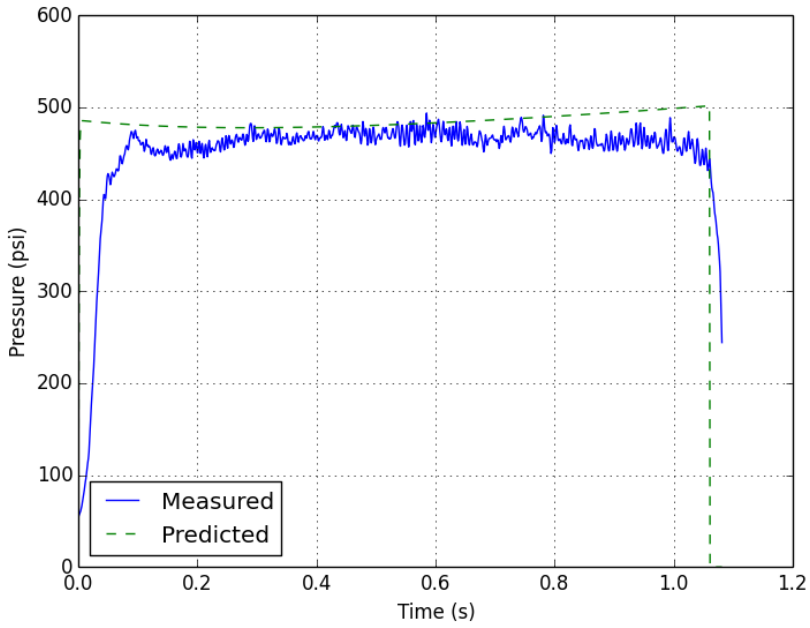

Figure E.12: Predicted and measured pressure traces for test 4-12.

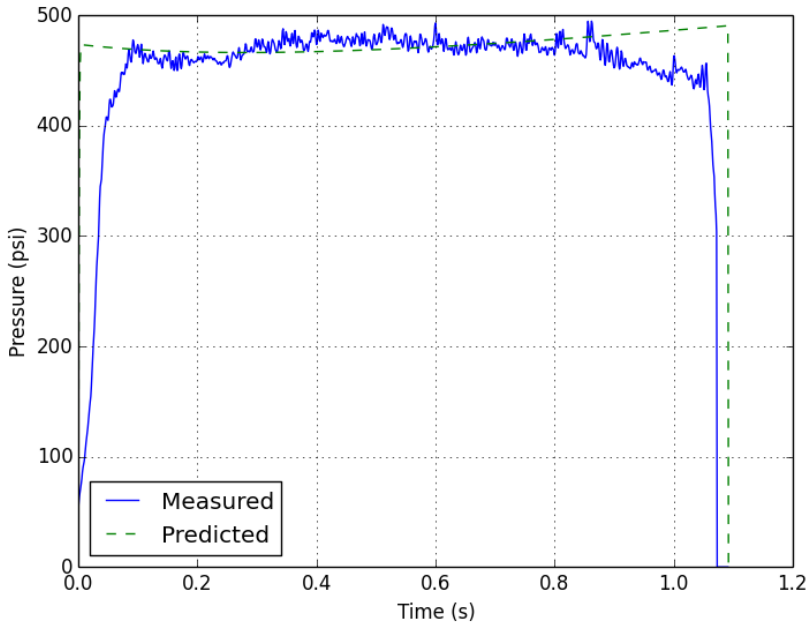

Figure E.13: Predicted and measured pressure traces for test 4-13.

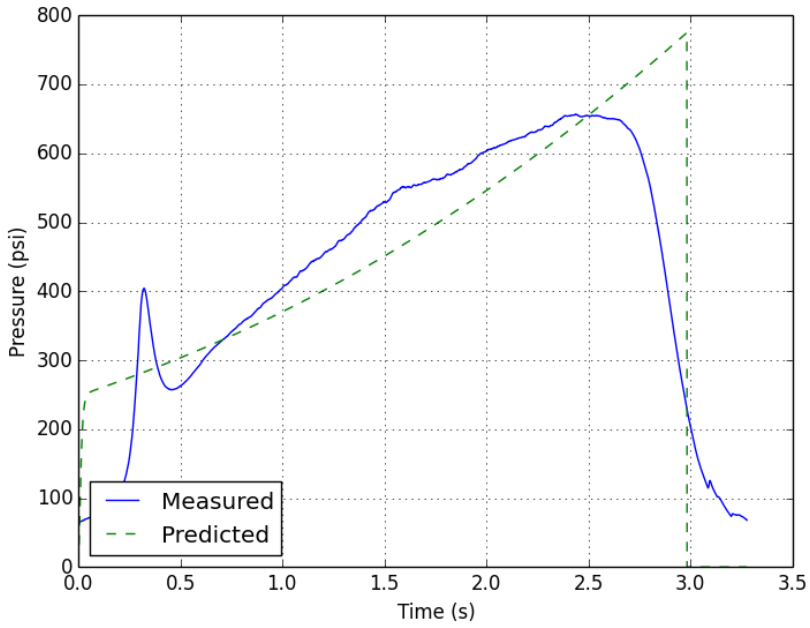

Figure E.14: Predicted and measured pressure traces for test 4-14.

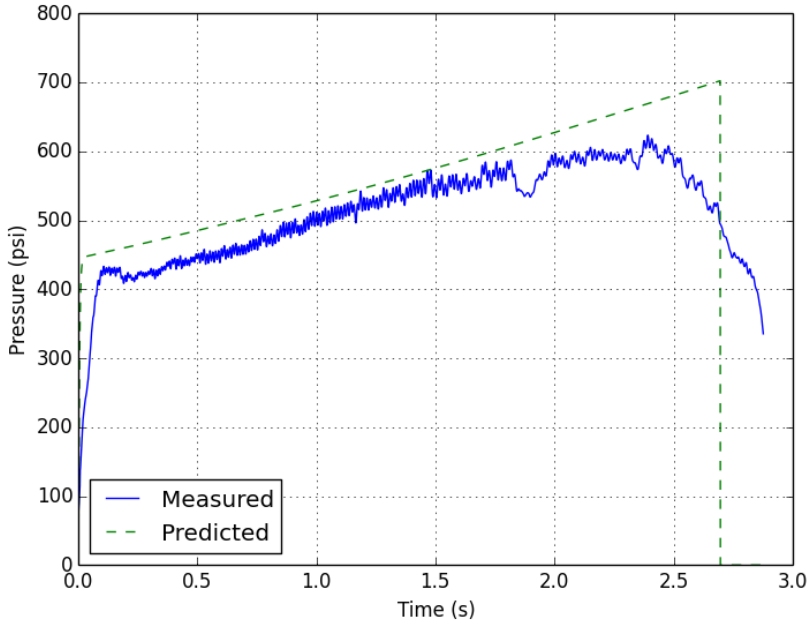

Figure E.15: Predicted and measured pressure traces for test 4-15.

APPENDIX F

CROOKED BORE BURN SURFACE AREA TABLES

Table F.1: Burn surface area data for test 4-1.

Web	Overall Length	A_p	A_{head}	A_{nozzle}	A_b	A_{ends}
0	11.5	37.385	1.846	1.946	41.177	3.792
0.02	11.46	38.691	1.778	1.882	42.351	3.66
0.04	11.42	39.987	1.708	1.815	43.51	3.523
0.06	11.38	41.274	1.635	1.746	44.655	3.381
0.08	11.34	42.55	1.559	1.674	45.783	3.233
0.1	11.3	43.816	1.482	1.599	46.897	3.081
0.12	11.26	45.072	1.401	1.523	47.996	2.924
0.14	11.22	46.318	1.319	1.443	49.08	2.762
0.16	11.18	47.554	1.233	1.361	50.148	2.594
0.18	11.14	48.78	1.146	1.277	51.203	2.423
0.2	11.1	49.996	1.055	1.19	52.241	2.245
0.22	11.06	51.202	0.963	1.1	53.265	2.063
0.24	11.02	52.398	0.868	1.008	54.274	1.876
0.26	10.98	53.584	0.77	0.914	55.268	1.684
0.28	10.94	54.14	0.679	0.817	55.636	1.496
0.3	10.9	53.787	0.598	0.717	55.102	1.315
0.32	10.86	52.737	0.523	0.615	53.875	1.138
0.34	10.82	51.005	0.453	0.511	51.969	0.964
0.36	10.78	48.485	0.387	0.404	49.276	0.791
0.38	10.74	45.028	0.325	0.294	45.647	0.619
0.4	10.7	40.307	0.267	0.182	40.756	0.449
0.42	10.66	33.472	0.212	0.068	33.752	0.28
0.44	10.62	21.442	0.163	0	21.605	0.163
0.46	10.58	13.797	0.117	0	13.914	0.117
0.48	10.54	8.445	0.077	0	8.522	0.077
0.5	10.5	4.469	0.043	0	4.512	0.043
0.52	10.46	1.632	0.017	0	1.649	0.017
0.54	10.42	0.05	0.001	0	0.051	0.001

Table F.2: Burn surface area data for test 4-2.

Web	Overall Length	A_p	A_{head}	A_{nozzle}	A_b	A_{ends}
0	11.5	35.504	1.944	2.014	39.462	3.958
0.02	11.46	36.824	1.879	1.952	40.655	3.831
0.04	11.42	38.133	1.812	1.888	41.833	3.7
0.06	11.38	39.433	1.743	1.821	42.997	3.564
0.08	11.34	40.722	1.671	1.752	44.145	3.423
0.1	11.3	42.001	1.596	1.68	45.277	3.276
0.12	11.26	43.27	1.519	1.605	46.394	3.124
0.14	11.22	44.529	1.44	1.528	47.497	2.968
0.16	11.18	45.778	1.358	1.449	48.585	2.807
0.18	11.14	47.017	1.273	1.366	49.656	2.639
0.2	11.1	48.246	1.186	1.282	50.714	2.468
0.22	11.06	49.465	1.096	1.195	51.756	2.291
0.24	11.02	50.673	1.004	1.105	52.782	2.109
0.26	10.98	51.872	0.91	1.013	53.795	1.923
0.28	10.94	53.061	0.813	0.918	54.792	1.731
0.3	10.9	54.239	0.713	0.821	55.773	1.534
0.32	10.86	55.408	0.611	0.721	56.74	1.332
0.34	10.82	56.566	0.506	0.619	57.691	1.125
0.36	10.78	57.714	0.399	0.514	58.627	0.913
0.38	10.74	57.036	0.289	0.417	57.742	0.706
0.4	10.7	52.675	0.177	0.335	53.187	0.512
0.42	10.66	44.155	0.063	0.262	44.48	0.325
0.44	10.62	27.001	0	0.197	27.198	0.197
0.46	10.58	16.85	0	0.139	16.989	0.139
0.48	10.54	9.967	0	0.089	10.056	0.089
0.5	10.5	4.993	0	0.047	5.04	0.047
0.52	10.46	1.574	0	0.016	1.59	0.016

Table F.3: Burn surface area data for test 4-3.

Web	Overall Length	A_p	A_{head}	A_{nozzle}	A_b	A_{ends}
0	11.5	35.579	1.976	1.976	39.531	3.952
0.02	11.46	36.896	1.913	1.913	40.722	3.826
0.04	11.42	38.202	1.847	1.847	41.896	3.694
0.06	11.38	39.498	1.779	1.779	43.056	3.558
0.08	11.34	40.785	1.708	1.708	44.201	3.416
0.1	11.3	42.061	1.635	1.635	45.331	3.27
0.12	11.26	43.327	1.559	1.56	46.446	3.119
0.14	11.22	44.583	1.481	1.481	47.545	2.962
0.16	11.18	45.829	1.4	1.401	48.63	2.801
0.18	11.14	47.065	1.317	1.317	49.699	2.634
0.2	11.1	48.291	1.231	1.232	50.754	2.463
0.22	11.06	49.506	1.143	1.143	51.792	2.286
0.24	11.02	50.712	1.052	1.053	52.817	2.105
0.26	10.98	51.908	0.959	0.959	53.826	1.918
0.28	10.94	53.094	0.863	0.863	54.82	1.726
0.3	10.9	54.269	0.765	0.765	55.799	1.53
0.32	10.86	55.435	0.664	0.664	56.763	1.328
0.34	10.82	56.59	0.561	0.561	57.712	1.122
0.36	10.78	57.736	0.455	0.455	58.646	0.91
0.38	10.74	58.871	0.347	0.347	59.565	0.694
0.4	10.7	59.758	0.237	0.236	60.231	0.473
0.42	10.66	53.039	0.151	0.122	53.312	0.273
0.44	10.62	33.592	0.084	0.007	33.683	0.091
0.46	10.58	9.521	0.034	0	9.555	0.034
0.48	10.54	0.659	0.003	0	0.662	0.003

APPENDIX G

FILE DESCRIPTION AND LOCATION

The raw data files recorded during testing as well as the Python scripts used in the ballistic analysis, optimization scheme, and uncertainty analysis are provided in a file database online. Table G.1 gives the files, a filename, and a description of each item in the database. The database can be accessed at `https://drive.google.com/folderview?id=0B_p39P6bhsy9X3JaSWx0bWVESmM&usp=sharing`.

Table G.1: Files used, description, and filename.

File	Description	Filename
4-1 Data	Test 4-1 raw data.	`4_1_Data.lvm`
4-2 Data	Test 4-2 raw data.	`4_2_Data.lvm`
4-3 Data	Test 4-3 raw data.	`4_3_Data.lvm`
4-4 Data	Test 4-4 raw data.	`4_4_Data.lvm`
4-5 Data	Test 4-5 raw data.	`4_5_Data.lvm`
4-6 Data	Test 4-6 raw data.	`4_6_Data.lvm`
4-7 Data	Test 4-7 raw data.	`4_7_Data.lvm`
4-8 Data	Test 4-8 raw data.	`4_8_Data.lvm`
4-9 Data	Test 4-9 raw data.	`4_9_Data.lvm`
4-10 Data	Test 4-10 raw data.	`4_10_Data.lvm`
4-11 Data	Test 4-11 raw data.	`4_11_Data.lvm`
4-12 Data	Test 4-12 raw data.	`4_12_Data.lvm`
4-13 Data	Test 4-13 raw data.	`4_13_Data.lvm`
4-14 Data	Test 4-14 raw data.	`4_14_Data.lvm`
4-15 Data	Test 4-15 raw data.	`4_15_Data.lvm`
Uncertainty Code	Monte Carlo routine for regression rate uncertainty.	`monte_carlo.py`
Optimization Routine	Optimization routine for both solids and hybrids.	`optimization_hybrid.py`
C Star Optimization	Searches within a range of $C^\star$ values to find a minimum error.	`optimization_c_star.py`
Plot Generator	Plots results from the optimization search.	`optimization_plotter.py`
Ballistic Analysis	Ballistic analysis code used by optimization code.	`prediction.py`
Uncertainty Analysis	Uncertainty analysis on test 4-4	`Uncertainty.nb`

REFERENCES

[1] Sutton, G. P. and Biblarz, O., *Rocket Propulsion Elements*, John Wiley & Sons, Inc., Hoboken, 8th ed., 2010.

[2] Knuth, W. H., Chiaverini, M. J., Sauer, A., and Gramer, D. J., "Solid-Fuel Regression Rate Behavior of Vortex Hybrid Rocket Engines," *AIAA Journal of Propulsion and Power*, Vol. 18, No. 3, May-June 2002.

[3] Frederick, R. A. J., Whitehead, J. J., Knox, L. R., and Moser, M. D., "Regression Rates Study of Mixed Hybrid Propellants," *AIAA Journal of Propulsion and Power*, Vol. 23, No. 1, January-Febuary 2007.

[4] Karabeyoglu, M. A., Cantwell, B. J., and Zilliac, G., "Development of Scalable Space-Time Averaged Regression Rate Expressions for Hybrid Rockets," *AIAA Journal of Propulsion and Power*, Vol. 23, No. 4, July-August 2007.

[5] Kearney, D. A., Joiner, K. F., Gnau, M. P., and Casemore, M. A., "Improvements to the Marketability of Hybrid Propulsion Technologies," *AIAA/ASME/SAE/ASEE 43rd Joint Propulsion Conference & Exhibit*, No. AIAA 2007-6144, American Institute of Aeronautics and Astronautics, Cincinnati, OH, July 2007.

[6] Kearney, D. A. and Geiman, W. W., "Accounting for Planned Fuel Expulsion by Hybrid Rockets," *41st AIAA/ASME/SAE/ASEE Joint Propulsion Conference & Exhibit*, No. AIAA 2005-3546, American Institue of Aeronautics and Astronautics, Tuscon, AZ, July 2005.

[7] McFarlane, J. S., Kniffen, R. J., and Lichatowich, J., "Design and Testing of AMROC's 250,000 lbf Thrust Hybrid Motor," *AIAA/SAE/ASME 29th Joint Propulsion Conference*, No. AIAA 93-2551, American Institute of Aeronautics and Astronautics, Monterey, CA, June 1993.

[8] Boardman, T. A., Abel, T. M., Claflin, S. E., and Shaeffer, C. W., "Design and Test Planning for a 250-KLBF-Thrust Hybrid Rocket Motor Under the Hybrid Propulsion Demonstration Program," Tech. Rep. AIAA 1997-2804, American Institute of Aeronautics and Astronautics, 1997.

[9] Culver, D. W. and Mueggenburg, H. H., "Aft Mounted Gas/Liquid Injector Technology for Gas Generator Cycle Hybrid Rockets," *AIAA/SAE/ASME 27th Joint Propulsion Conference*, No. AIAA 91-2518, American Institute of Aeronautics and Astronautics, Sacramento, CA, June 1991.

[10] Whitehead, J. J., *Experimental Evaluation of a Mixed Oxidizer Hybrid Concept with GOX*, Master's thesis, University of Alabama in Huntsville, 2004.

[11] Prince, A. S., Carpenter, R. L., Boardman, T. A. Abel, T. M., and Claflin, S. E., "Design and Testing of an Upper Stage Hybrid Propulsion System Using Hydrogen Peroxide Oxidizer," *AIAA/ASME/SAE/ASEE 36th Joint Propulsion Conference and Exhibit*, No. AIAA 2000-3542, American Institute of Aeronautics and Astronautics, Huntsville, AL, July 2000.

[12] Knox, L. R., *Experimental Determination of Regression Rates of Mixed Hybrid Propellants*, Master's thesis, University of Alabama in Huntsville, 2004.

[13] Aeronautics, N. and Administration, S., "Hybrid Propulsion for Upper-Stage Boosters," NASA SBIR/STTR Award, 2011, Awarded to Exquadrum, Inc.

[14] Zilliac, G., Waxman, B. S., Evans, B., Karabeyoglu, M. A., and Cantwell, B., "Peregrine Hybrid Rocket Motor Development," *50th AIAA/ASME/SAE/ASEE Joint Propulsion Conference*, No. AIAA 2014-3870, American Institute of Aeronautics and Astronautics, Cleveland, OH, July 2014.

[15] Karabeyoglu, M. A., Cantwell, B. J., and Altman, D., "Development and Testing of Paraffin-Based Hybrid Rocket Fuels," *AIAA/ASME/SAE/ASEE 37th Joint Propulsion Conference and Exhibit*, No. AIAA 2001-4503, American Institute of Aeronautics and Astronautics, Salt Lake City, UT, July 2001.

[16] Miyata, K. and Frederick, R. A. J., "Ammonium Nitrate-Based Solid Fuel Gas Generator for Gas Hybrid Rockets," *AIAA/SAE/ASME/ASEE 32nd Joint Propulsion Conference*, No. AIAA 96-3254, American Institute of Aeronautics and Astronautics, Buena Vista, FL, July 1996.

[17] Abel, T., Markopoulos, P., Lund, G., Prince, A., Claflin, S., and Caravella, J., "Design and Development of a Peroxide Hybrid Upper Stage Propulsion System," *3rd International Hydrogen Peroxide Propulsion Conference*, Gulf Port, MS, November 2000.

[18] Cohen, N. S. and Strand, L. D., "Hybrid Propulsion Based on Fluid-Controlled Solid Gas Generators," *AIAA/SAE/ASME/ASEE 29th Joint Propulsion Conference and Exhibit*, No. AIAA 93-2550, American Institute of Aeronautics and Astronautics, Monterey, CA, June 1993.

[19] Markopoulos, P. and Abel, T., "Design and Testing of a Hydrogen Peroxide Hybrid Upper Stage Propulsion System," *AIAA/ASME/SAE/ASEE 37th Joint Propulsion Conference and Exhibit*, No. AIAA 2001-3243, American Institute of Aeronautics and Astronautics, Salt Lake City, UT, July 2001.

[20] Estey, P., Altman, D., and McFarlane, J., "An Evaluation of Scaling Effects for Hybrid Rocket Motors," *AIAA/ASME/SAE/ASEE 27th Joint Propulsion Conference*, No. AIAA 1991-2517, American Institute of Aeronautics and Astronautics, Sacramento, CA, June 1991.

[21] Fry, R. S., Deluca, L., Frederick, R., Gadiot, G., Strecker, R., Whitehouse, A., Traineau, J.-C., Ribereau, D., and Reynaud, J.-P., "Evaluation of Methods for Solid Propellant Burning Rate Measurement," Tech. rep., Air Force Research Laboratory, 2002.

[22] Watson, T. J., Jordan, F. W., and Stockham, L. W., "Accurate Burn Rate Determination for Sub-Scale Test Motors," *AIAA/SAE/ASME/ASEE 29th Joint Propulsion Conference and Exhibit*, No. AIAA 93-2060, American Institute of Aeronautics and Astronautics, Monterey, CA, June 1993.

[23] Lilley, J. S., "Burning Rate Characterization from One Motor Firing: An Analytical Approach," *AIAA/SAE/ASME 19th Joint Propulsion Conference*, No. AIAA 83-1315, American Institute of Aeronautics and Astronautics, Seattle, WA, June 1983.

[24] Chiaverini, M. J., Serin, N., Johnson, D. K., Lu, Y., Kuo, K., and Risha, G. A., "Regression Rate Behavior of Hybrid Rocket Solid Fuels," *AIAA Journal of Propulsion and Power*, Vol. 16, No. 1, January-February 2000.

[25] Lund, G. K., Starrett, W. D., and Jensen, K. C., "Development and Lab-Scale Testing of a Gas Generator Hybrid Fuel in Support of the Hydrogen Peroxide Hybrid Upper Stage Program," *AIAA/ASME/SAE/ASEE 37th Joint Propulsion Conference and Exhibit*, No. AIAA 2001-3244, American Institute of Aeronautics and Astronautics, Salt Lake City, UT, July 2001.

[26] Frederick, R. A. J. and Greiner, B. E., "Laboratory-Scale Hybrid Rocket Motor Uncertainty Analysis," *AIAA Journal of Propulsion and Power*, Vol. 12, No. 3, May-June 1996.

[27] Hollman, S. L. and Frederick, R. A. J., "Labscale Testing Techniques for Hybrid Rockets," *AIAA/SAE/ASME 29th Joint Propulsion Conference*, No. AIAA 93-2409, American Institute of Aeronautics and Astronautics, Monterey, CA, June 1993.

[28] Coleman, H. W. and Steele, W. G., *Experimentaion, Validation, and Uncertainty Analysis for Engineers, 3rd Edition*, John Wiley & Sons, Inc., Hoboken, NJ, 2009.

[29] Jones, D. A., *Advanced Digital Methods for Solid Propellant Burning Rate Determination*, Master's thesis, University of Alabama in Huntsville, 2015.

[30] Wernimont, E. J. and Heister, S. D., "Performance Characterization of Hybrid Rockets Using Hydrogen Peroxide Oxidizer," *AIAA/ASME/SAE/ASEE 31st Joint Propulsion Conference and Exhibit*, No. AIAA 95-3084, American Institute of Aeronautics and Astronautics, San Diego, CA, July 1995.

[31] DeZilwa, S., Karabeyoglu, A., Zilliac, G., King, L., and Reinath, M., "Combustion Oscillations in High-Regression-Rate Hybrid Rockets," *AIAA/ASME/SAE/ASEE 39th Joint Propulsion Conference and Exhibit*, No. AIAA 2003-4465, American Institute of Aeronautics and Astronautics, Huntsville, AL, July 2003.

[32] Karabeyoglu, M. A. and Altman, D., "Dynamic Modeling of Hybrid Rocket Combustion," *AIAA Journal of Propulsion and Power*, Vol. 15, No. 4, July-August 1999.

[33] DeZilwa, S., Zilliac, G., and Reinath, M., "Time-Resolved Fuel-Grain Port Diameter Measurement in Hybrid Rocket," *AIAA Journal of Propulsion and Power*, Vol. 20, No. 4, July-August 2004.